ISBN 978-82-326-1870-5 (printed ver.)
ISBN 978-82-326-1871-2 (electronic ver.)
ISSN 1503-8181

Eva Anne Mørtsell

Doctoral thesis

Doctoral theses at NTNU, 2016:266

Eva Anne Mørtsell

Precipitation in multicomponent, lean, Al-Mg-Si alloys

A transmission electron microscopy study

NTNU
Norwegian University of
Science and Technology

Doctoral theses at NTNU, 2016:266

NTNU
Norwegian University of
Science and Technology
Thesis for the Degree of
Philosophiae Doctor
Faculty of Natural Sciences and Technology
Department of Physics

NTNU

NTNU
Norwegian University of
Science and Technology

Eva Anne Mørtsell

Precipitation in multicomponent, lean, Al-Mg-Si alloys

A transmission electron microscopy study

Thesis for the Degree of Philosophiae Doctor

Trondheim, September 2016

Norwegian University of Science and Technology
Faculty of Natural Sciences and Technology
Department of Physics

NTNU
Norwegian University of
Science and Technology

NTNU
Norwegian University of Science and Technology

Thesis for the Degree of Philosophiae Doctor

Faculty of Natural Sciences and Technology
Department of Physics

ISBN 978-82-326-1870-5 (printed ver.)
ISBN 978-82-326-1871-2 (electronic ver.)
ISSN 1503-8181

Doctoral theses at NTNU, 2016:266

Printed by NTNU Grafisk senter

Abstract

Aluminium alloys have a number of versatile applications, and there are numerous alloys in production today, where a variety of solute additions and heat treatments are applied. This work focusses on lean, age-hardenable Al-Mg-Si alloys, which are light weight, have excellent corrosion resistance and a moderate strength potential. In Al-Mg-Si alloys it is the growth of nanosized needles, consisting of Mg, Si and Al itself, which leads to an increase in strength during heat treatment of the alloys. The nanosized needles are metastable and grow along the three <001> Al crystal directions. During heat treatment, several needle phases may form, dependent on parameters such as the extent of the heat treatment, its temperature and the alloy composition.

A major challenge in industry, and the first motivation behind this work, is to make extrusion of lean Al-Mg-Si alloys easier and faster, while simultaneously not making any sacrifices in strength. The second major motivational point of this thesis is to connect the macroscopic material properties like strength and extrudability to the atomic scale characteristics. Only in this way tailor-made alloys can be made for specific applications. Transmission electron microscopy (TEM) serves as an excellent tool for microstructure characterization of Al. The high spatial resolution and possibility of detecting a number of different electron-sample interactions are obvious advantages.

High angle annular dark field scanning TEM (HAADF-STEM) with aberration corrected lenses provides exceptionally high spatial resolution, down to the atomic scale. Aberration corrected HAADF-STEM is particularly well suited for detecting elements with different atomic numbers (Z) because of its Z contrast. However, in some cases the elements might be too close in atomic number to separate intensity differences, which is where electron energy loss spectroscopy (EELS) comes to aid. With EELS one obtains a ‘fingerprint’ of each element based on the energy losses of the electrons, which are dependent on the elements they have interacted with while passing through the sample.

For surface-specific dynamics in the material, information can be attained by photoelectron spectroscopy (PES). PES enables us to do in-situ investigations of core levels during heat treatment of the material. By making use of this method, the complications of detecting elements with overlapping EEL edges, like e.g. Li and Mg, can be solved.

Two main approaches have been chosen to solve the extrudability vs strength issue here. The first approach was based on lowering the amount of added Si and Mg, while adding back a smaller or equal amount of Li, Cu, Ge or Ag. In the second approach, ‘disturbed ageing’ was applied at various times during heat treatment. This was accomplished by elastic straining or introducing small plastic deformations to the material.

It has been demonstrated how strength loss in an Al-Mg-Si alloy, caused by reduction in solute, can be compensated by adding back smaller quantities of Li, Cu, Ag or Ge. These

solute additions were added to Al-Mg-Si alloys alone or in different combinations. Ge was discovered to be the most effective solute addition, significantly refining the precipitation and strengthening the material in spite of lower total solute.

Cu, Ag and Ge additions have strong influence on the main hardening precipitate, *β''*. Ge in particular changes its structure and promotes disorder, which seems to be favourable for increased material strength. Cu and Ag both participate in the precipitation of needles and change the precipitation sequence. HAADF-STEM investigations indicated that Li causes modest structural changes to the main hardening precipitate *β''*.

DFT has been used to support the experimental results and better explain the observed features in each alloy. Bonding energies, volume misfits, and formation enthalpies have been calculated for solute additions, vacancies and structural variants of the *β''* phase. DFT and HAADF-STEM support intensity variations suggesting Li to occupy Mg sites, and in particular the Mg3 sites in *β''*.

The potential of atomic resolution EELS has been demonstrated by detailed investigation of the elemental distribution in a precipitate cross section in a multicomponent Al alloy. Furthermore, a correlative analysis of the EELS data was performed and connected to the results. The EELS technique alone was able to resolve both the face centred cubic (fcc) Al lattice along the <001> Al zone axes and the hexagonal Si-network in a precipitate cross section. Some atomic columns were revealed to contain a mix of elements after combining EELS and HAADF-STEM.

It has been demonstrated how a commercial Al-Mg-Si alloy can get enhanced strength at peak hardness conditions when elastic strain is applied at the beginning of natural ageing. The strengthening effect is explained by enhanced formation of clusters, causing a higher number density of precipitates at peak hardness. Applying 1 % plastic deformation increased the material strength as compared to an un-deformed reference alloy; the strengthening effect is in this case attributed to the introduction of dislocations to the material during deformation.

X-ray photoelectron spectroscopy (XPS) and X-ray photoemission electron microscopy (XPEEM) were used to study Li, Mg and Si in the surface of an Al-Mg-Si-Li alloy. The surface oxide layer was sputtered to a negligible thickness, and the relative abundance of alloying agents (Li, Mg and Si) was recorded for different time-stamps during annealing. All three elements were recorded to appear with a significant increase in surface concentration. The concentration decreased again with further increase in annealing temperature and duration of annealing. Si and Li both occur everywhere on the alloy surface, while Mg migration is mostly restricted to grain boundaries. Li occurs at much higher temperature than the two respective alloying agents.

Preface

This thesis is submitted to the Norwegian University of Science and Technology, Trondheim (NTNU) for partial fulfilments of the requirements for the degree Philosophiae Doctor (Ph.D.). The work has been conducted at the Department of Physics at NTNU, from September 2012 to July 2016. One fourth of the work has been teaching duties at the Department of Physics at NTNU. The Ph.D. project has been a part of the KMB RolEx project (*Smart alloy development for rolling and extrusion*), funded by Hydro Aluminium and Forskningsrådet. The work has been a collaboration between NTNU, SINTEF and Hydro Aluminium.

The work has been done at the TEM Gemini Centre in Trondheim, a collaboration between the Department of Physics (NTNU), Materials Science and Engineering (NTNU) and SINTEF Materials and Chemistry, Trondheim. The work has been carried out under supervision by Professor Randi Holmestad and co-supervision of Dr. Calin Marioara and Dr. Jostein Røyset.

The thesis consists of a collection of papers, in addition to an introduction part and the necessary background theory on materials and experimental techniques.

Papers Included in the Thesis

1. *Effects of Germanium, Copper and Silver Substitutions on Hardness and Microstructure in Lean Al-Mg-Si Alloys*

E. A. Mørtsell, C. D. Marioara, S. J. Andersen, J. Røyset, O. Reiso and R. Holmestad. *Metallurgical and Materials Transactions A, Volume 46, Issue 9, pp 4369 – 4379 (2015)*

2. *TEM and HAADF-STEM investigations on the effect of Cu and Ge additions on precipitation in 6xxx Al alloys*

E. A. Mørtsell, C. D. Marioara, S. J. Andersen, J. Røyset, O. Reiso and R. Holmestad. *Microscopy and Analysis, January Issue (2016)*

3. *Elemental electron energy loss mapping of a precipitate in a multi-component aluminium alloy*

E. A. Mørtsell, S. Wenner, P. Longo, S. J. Andersen, C. D. Marioara and R. Holmestad. *Micron, Volume 86, pp 22 – 29 (2016)*

4. *Atomistic details of precipitates in lean Al-Mg-Si alloys with trace additions of Ag and Ge studied by HAADF-STEM and DFT*

E. A. Mørtsell, S. J. Andersen, J. Friis, C. D. Marioara and R. Holmestad

Submitted

5. *The effects and behaviour of Li and Cu alloying agents in lean Al-Mg-Si alloys*

E. A. Mørtsell, C. D. Marioara, S. J. Andersen, I. G. Ringdalen, J. Røyset, O. Reiso and R. Holmestad

Submitted

6. *The Effect of 1 % Plastic Deformation and Elastic Strain on a 6060 Aluminium Alloy during Natural and Artificial Ageing*

   E. A. Mørtsell, I. Westermann, C. D. Marioara, K. O. Pedersen, S. J. Andersen, J. Røyset and R. Holmestad

   In progress

7. *Thermal migration of alloying agents in aluminium*

   S. Cooil, E. A. Mørtsell, F. Mazzola, M. Jorge, S. Wenner, M. Edmonds, L. Thomsen; H. G. Klemm, G. Peschel, R. Holmestad and J. Wells

   In progress

Statement of Author Contributions

Paper 1

Eva Mørtsell was in charge of manuscript writing. TEM sample preparation, bright field TEM, HAADF-STEM and statistics were done by Eva Mørtsell. Calin Marioara helped with HAADF-STEM training, imaging and data analysis. S. J. Andersen contributed significantly to interpret the results and to revise the manuscript. All co-authors contributed to interpretation of the results and commenting on the manuscript. Birgitte Karlsen did the heat treatments and HV measurements.

Paper 2

Eva Mørtsell was in charge of manuscript writing. The experimental work and interpretation of results was done by Eva Mørtsell. Calin Marioara supervised the HAADF-STEM work. All co-authors helped interpreting the results and commented on the manuscript.

Paper 3

Eva Mørtsell and Sigurd Wenner did the sample preparation. Eva Mørtsell was in charge of manuscript writing and interpretation of experimental results. Paolo Longo did the experimental EELS work, aided by Eva Mørtsell and Sigurd Wenner. Sigmund Andersen, Calin Marioara and Randi Holmestad supervised the work, helped interpreting the results and commented on the manuscript.

Paper 4

Eva Mørtsell was in charge of manuscript writing. Sample preparation and some HAADF-STEM work was done by Eva Mørtsell, in addition to interpreting the results. Sigmund Andersen contributed significantly to interpreting results and suggesting precipitate-phase models. Calin Marioara did most of the HAADF-STEM work, and Jesper Friis did the DFT simulations. Randi Holmestad supervised the work, and like all co-authors helped interpreting results and commented on the manuscript.

Paper 5

Eva Mørtsell was in charge of the experimental work, interpretation of results and writing of the manuscript. Inga Ringdalen and Jesper Friis did the DFT simulations. Calin Marioara and Sigmund Andersen contributed a great deal in interpretation of results and revising the manuscript. Jostein Røyset, Oddvin Reiso and Randi Holmestad helped supervise the work, discuss and interpret results and comment on the manuscript. Birgitte Karlsen did the heat treatments and HV measurements.

Paper 6

The experimental work was done by Eva Mørtsell, except hardness measurements and preparation of tensile samples which were done by Ida Westermann. Eva Mørtsell also interpreted the results and wrote the manuscript. The initial idea behind this work came from Ida Westermann, Ketill Pedersen and Jostein Røyset. Calin Marioara and Sigmund Andersen helped interpret results and revise the manuscript. Ida Westermann, Ketill Pedersen, Jostein Røyset and Randi Holmestad also commented on the manuscript. Jostein Røyset and Randi Holmestad supervised the work and contributed to discussions about the results.

Paper 7

Eva Mørtsell did the sample preparation and helped interpreting results and writing the manuscript. Simon Cooil and Federico Mazzola did the measurements and data analysis. All co-authors helped interpret the results and commented on the manuscript. The work was supervised by Justin Wells and Randi Holmestad.

Other Scientific Contributions

Publications

1. *The Effect of Cu and Ge Additions on Strength and Precipitation in a lean 6xxx Aluminium Alloy*

   E. A. Mørtsell, C. D. Marioara, S. J. Andersen, J. Røyset, O. Reiso and R. Holmestad. EMAG, *Journal of Physics, Conference Series 644 012028 (2015)*

2. *The effect of Elastic Straining on a 6060 Aluminium Alloy during Natural or Artificial Ageing*

   E. A. Mørtsell, I. Westermann, C. D. Marioara, K. O. Pedersen, S. J. Andersen, J. Røyset and R. Holmestad. *Materials Science Forum, Volumes 794 – 796, pp 1205 – 1210 (2014)*

3. *Cu atoms suppress misfit dislocations at the β"/Al interface in Al-Mg-Si alloys*

   T. Saito, F. J. H. Ehlers, W. Lefebvre, D. Hernandez-Maldonado, R. Bjørge, C. D. Marioara, S. J. Andersen, E. A. Mørtsell, R. Holmestad. *Scripta Materialia, Volume 110, pp 6 – 9 (2016)*

Oral Presentations (presenter underlined)

- *The Effect of Elastic and Plastic Ageing of a 6060 Aluminium Alloy*
  E. A. Mørtsell, I. Westermann, C. D. Marioara, K. O. Pedersen, S. J. Andersen, J. Røyset and R. Holmestad
  ICAA, 14th International Conference on Aluminium Alloys
  15th – 19th June 2014, Trondheim, Norway.

- *The Effect of Cu, Ag and Ge Additions on Strength and Precipitation in a Lean 6xxx Aluminium Alloy*
  E. A. Mørtsell, C. D. Marioara, J. Røyset and R. Holmestad
  IMC, 18th International Microscopy Congress
  7th – 12th September 2014, Prague, Czech Republic.

- *HAADF-STEM Analysis of Precipitates in Al-Mg-Si Alloys*
  E. A. Mørtsell, S. J. Andersen, C. D. Marioara and R. Holmestad
  SCANDEM, the 67th annual conference of the Nordic Microscopy Society
  7th – 10th June 2016, Trondheim, Norway.

- *The effect of Li addition on strength and precipitation in a lean Al 6xxx alloy –* ***Young Scientist Award***
  E. A. Mørtsell, C. D. Marioara, S. J. Andersen, O. Reiso, J. Røyset and R. Holmestad
  ICAA, 15th International Conference on Aluminium Alloys
  12th – 16th June 2016, Chongqing, China.

- *Characterization of multicomponent Al alloys by TEM, HAADF-STEM, EELS and DFT*
  E. A. Mørtsell, S. J. Andersen, C. D. Marioara, J. Røyset, J. Friis and R. Holmestad
  EMC, 16th European Microscopy Congress
  28th August – 2nd September 2016, Lyon, France.

Posters

- *Elastic Ageing of an Aluminium 6060 Alloy*
  E. A. Mørtsell, I. Westermann, C. D. Marioara, K. O. Pedersen, J. Røyset and R. Holmestad
  SCANDEM, the 64th annual conference of the Nordic Microscopy Society
  10th – 14th June 2013, Copenhagen, Denmark.

- *Hardness evolution during aging of lean 6xxx alloys for extrusion, connected to precipitation: a TEM/STEM study*
  T. Omi, C. D. Marioara, E. A Mørtsell, R. Holmestad and J. Røyset
  ICAA, 14th International Conference on Aluminium Alloys
  15th – 19th June 2014, Trondheim, Norway

- *TEM and HAADF STEM Investigations of Ge addition to an Al 6060 Alloy*
  E. A. Mørtsell, C. D. Marioara, S. J. Andersen, J. Røyset and R. Holmestad
  SuperSTEM Summerschool, Advanced Topics in Abberation-Corrected STEM
  4th – 7th July 2014, Daresbury, UK

- *The Effect of Cu and Ge Additions on Strength and Precipitation in a lean 6xxx Aluminium Alloy –* ***1st poster prize***
  E. A. Mørtsell, C. D. Marioara, S. J. Andersen, J. Friis, O. Reiso, J. Røyset and R. Holmestad
  MMC, Microscience Microscopy Congress. Incorporating EMAG, Electron Microscopy and Analysis Group Conference.
  29th June – 2nd July 2015, Manchester, UK.

Trondheim, July 2016

Eva Anne Mørtsell

Acknowledgements

Professor Randi Holmestad has been my main supervisor these past four years. I would like to thank her for all support she has given, accompanied with her positive and solution oriented mind set. I am happy I could always count on her making decisions in my best interest and answering my emails at all times. When adding these years to those spent on my master's degree, she has been my supervisor for 6 years in total, so thank you Randi for all these years and time spent together.

The research council of Norway and Hydro aluminium are greatly acknowledged for funding the RolEx project. This work could also not have been completed without the excellent NORTEM facilities and the TEM Gemini centre in Trondheim.

Dr Calin Marioara and Dr Sigmund Andersen have both been indispensable sources of knowledge during these past four years. They have both spent a lot of time and effort to help explain experimental results, come up with ideas and giving good advice. Thank you for being excellent supervisors!

I would also like to thank Dr Jostein Røyset and Dr Oddvin Reiso from Hydro aluminium for their friendly advice and encouragement, and for providing insightful discussions regarding my work. Many thanks also to Ida Westermann and Ketill Pedersen for our collaboration during my first year of the Ph.D. Thanks to Ruben Bjørge, Jesper Friis and Inga Ringdalen, from SINTEF, and Paolo Longo from Gatan for nice and interesting collaborations during these past years.

There are many bright minds in the TEM group whom I would also like to thank: Sigurd Wenner for always answering my questions and helping me out. Bjørn Soleim for being incredibly helpful at odd (and even) hours and always fixing things that the rest of us are not treating well. Thanks also to Ragnhild Sæterli and Per-Erik Vullum for giving training on the microscopes and helping out when I needed it. I am very happy to have gotten to know everyone in the TEM group and our section! You are so many, so please imagine all your names in this sentence! And many thanks to my great office-mate Julie Nilsen, and my former (also great) office mate Vidar Fauske who fortunately proof-read this thesis.

I have also been lucky enough to join the group of Justin Wells for beamtimes both at Maxlab in Lund and at BESSY in Berlin. Thanks for fun and fascinating trips and also for giving me an opportunity to work with all of you.

It is difficult to describe how happy I have been to have good friends around during my Ph.d, but I will give it a try (both in English and “på norsk”). Inga, André og lille Elida, tusen takk for at dere heier på meg, dere er fantastiske! Trude og Ida: jeg er så glad for at dere flyttet til Trondheim og at vi holder kontakten! Jeg håper vi møtes, for kaffe og prat, i mange mange år til! Dog forhåpentligvis litt mindre prat om ph.d nå framover.

Sylvie, Federico, Astrid Marie, Lars-Martin, Eva-Therese, Erisa, Lars, Hanna and Karin (yes you are many but very important!): I hope you all realise how much I appreciate your friendship and spending time with you. Thanks for always asking how I am doing and showing interest in my work! Tusen takk Martin for at du har hørt på alt jeg har å fortelle om avhandling og jobb det siste året, det har hjulpet mye mer enn du tror. Jeg gleder meg til å se mer til deg framover!

Sist men ikke minst, ‘folkan fra Sommerhus og Harstad’. Mamma, Ester Karen, Hedda og Geir (og udyran): nå skal jeg endelig prøve å komme heim* på ferie uten bøker som må leses og artikler som må skrives! Takk for at dere har holdt ut med en til dels uforutsigbar fysikk-student i alle disse årene og at dere alltid er en telefonsamtale unna dersom hjemlengselen tar overhånd! Jeg hadde ikke vært her uten dere.

**heim*

List of Acronyms

AA Artificial ageing

ADF Annular dark field

bcc body centred cubic

BF Bright field

CTF Contrast transfer function

DF Dark field

DFT Density functional theory

EELS Electron energy loss spectroscopy

Eq. Equation

fcc Face centred cubic

FEG Field emission gun

Fig. Figure

GP Guinier-Preston

HAADF High angle annular dark field

HR High resolution

HV Vickers hardness

ISO International organization for standardisation

LEED Low energy electron diffraction

LEEM Low energy electron microscopy

MEM Mirror electron microscopy

NA Natural ageing

NTNU Norwegian University of Science and Technology

NORTEM Norwegian centre for transmission electron microscopy

PES Photoelectron spectroscopy

(P)EELS Parallel electron energy loss spectroscopy

PEEM Photoemission electron microscopy

Ph.D Philosophiae doctor

PSF Point spread function

RolEx Smart 6xxx Alloy Development for Rolling and Extrusion

RT Room temperature

RX RolEx – for alloy designations

SA Selected area

sc Simple cubic

SHT Solution heat treatment

SSSS Supersaturated solid solution

SPELEEM Spectroscopic photoemission and low energy electron microscope

STEM Scanning transmission electron microscopy

TEM Transmission electron microscopy

UV Ultra violet

UHV Ultra high vacuum

VASP Vienna ab-initio simulation package

XPEEM X-ray photoemission electron microscopy (PEEM using synchrotron radiation)

XPS X-ray photoelectron spectroscopy

Contents

Part I
Introduction

Chapter 1

Motivation

Aluminium is currently competing with fish to be the second most exported product in Norway after oil. The worldwide needs for light metals are growing, and aluminium is a very good candidate to satisfy these demands. The only metal which is more frequently used in the world today is steel. Steel is heavy, which is one of the reasons why medium and high strength aluminium alloys are becoming increasingly popular. Light metals do for example lead to much lower energy consumption in automotive vehicles, which is why they are frequently referred to as environmental friendly. Additionally, aluminium is easy to recycle. Only 5 percent of the energy which is needed to produce new aluminium is required for recycling it. Intriguingly, approximately 75 % of all aluminium ever made is still in use [1].

Age-hardened, medium-strength aluminium alloys are mostly used for architectural and automotive purposes. Mg and Si are added to the alloy because these elements enable the formation of nanosized needles during heat treatment, and these needles are the secret to aluminium's excellent strength potential. Al-Mg-Si alloys, often referred to as 6xxx alloys, are shaped in soft condition, usually by extrusion or rolling, and are then age hardened to their final strength.

It seems like optimizing alloy properties is a never ending quest. This thesis aims to improve and understand the extrudability of lean alloys, while not compromising in-service strength and other sought-for material properties. It also focusses on atomistic understanding of the processes, which in turn should make way for improving simulations. Improved extrudability in this viewpoint refers to low energy expenditure and higher extrusion speed. This is a challenge since solute additions are needed to grow hardening precipitate phases, while at the same time they decrease ductility and increase strain hardening and flow stress [2]. It is advantageous for optimal extrusion rates to limit the total amount of solute, and the content of some solutes in particular. An increase in extrusion speed achieved by solute reduction inevitably causes a loss in material strength. Different approaches to circumvent this effect have been explored and are presented in this thesis. The first approach has been to add new, "exotic" elements or combinations of such. Li, Cu, Ge and Ag were chosen because of their positive effect on precipitation, hardening response and in-service strength. The second approach was to subject lean Al-Mg-Si alloys to disturbances during the heat treatment. We will here be dealing with elastic strain or small plastic deformations of the material during different stages of the heat treatment. It is already well-known that higher levels of plastic

deformation lead to an increased hardness of the material because of the introduction of dislocations. The initial theory is that disturbances during ageing should lower the energy needed to nucleate and grow precipitate needles, consequently increasing the number density of hardening precipitates and resulting in an increased hardening response.

One of the most important characterization techniques for hardening phases in aluminium alloys is transmission electron microscopy (TEM). Using this powerful tool allows us to quantify the precipitate needle microstructure and morphology. It is possible to determine which precipitate phases are present, and with electron lens aberration correction, even the location and type of atoms can be identified. As TEM uses the 2D projection of our sample, other related techniques have been applied in order to come closer to the complete depiction of the material microstructure. High angle annular dark field scanning-TEM (HAADF-STEM) gives us the possibility to decide the atomic number of the elements present due to its atomic number contrast, where the intensity increases with increasing atomic number. HAADF-STEM and TEM might not be sufficient. In such cases, electron energy loss spectroscopy (EELS) or photoelectron spectroscopy (PES) techniques can give us the information we seek. EELS allows us to determine if just one element is present in a projected column or if we are actually dealing with a mix of elements. In particular, atomically resolved EELS would give unambiguous results, as it can reveal which elements are present in each atomic column from the 2D projection. In some cases, the Li and Mg EEL edges overlap, this is however not an issue with PES. PES also allows for in-situ measurements during annealing of the material. It is exceedingly important to understand the connection between theory and experiments, for this reason density functional theory (DFT) has been used to corroborate and interpret the experimental work.

The objective of this thesis has in short been to connect the microscopic features of lean alloys with properties like strength and extrudability at the macro-scale. The experimental work evolves around TEM, HAADF-STEM, EELS and PES. The features of the material have been investigated at several length scales, ranging from micrometres to the atomic scale. Finally, the microscopic properties should be explained and connected to the reduction of solutes in extruded and rolled Al products.

Chapter 2

Aluminium

Aluminium is not found naturally in its pure state on Earth, however, oxidized states occur frequently, like in for example naturally occurring bauxite rocks. Both the Earth and the Moon has a high abundancy of aluminium in their crusts. In the Earth's crust, aluminium is the third most abundant element and the most abundant metal [3]. Norway is a significant player in the global Al market, where Al oxide is extracted from bauxite, and subsequently reduced by electrolysis to obtain pure, metallic aluminium. Metallic aluminium is silvery-white in appearance, soft and non-magnetic.

Figure 2.1 Crystal structure of a unit cell in fcc aluminium next to a beverage can made out of aluminium. The light blue atoms are situated at the corners of the unit cell, while the dark blue atoms are situated at the faces.

The density of metallic, solid aluminium is 2.7 g/cm^3, less than a third of the density of steel [4]. This makes aluminium a particularly light metal, similar to titanium and magnesium. Pure aluminium in its solid state is crystalline, with a face centred cubic (fcc) unit cell, see insert in Fig. 2.1. Because of high strength-to-weight ratio, aluminium alloys are used in a vast number of applications and an increasingly important factor in aluminium production is the material's potential to be recycled.

In this chapter there will be given an introduction to aluminium alloys, focussing on the 6xxx series. Strengthening mechanisms will be explained with emphasis on precipitation hardening, which is the main hardening mechanism for Al-Mg-Si alloys. Finally, the solute elements that have been used in this thesis will be introduced, focussing on their effects on precipitation and strength.

2.1 Aluminium Alloys

By adding solute elements to aluminium, the material can be tailored into having specialized properties. Properties of particular interest are in-service strength, electrical conductivity, corrosion resistance, formability and the ability to be recycled.

There are two main categories of aluminium alloys, *cast alloys* and *wrought alloys,* which are directly cast or worked into their final shapes respectively. Wrought alloys are usually cast into billets and subsequently formed to their ultimate shapes. It is common to further separate wrought alloys in two subcategories: alloys which are heat treatable and those which are not. If an aluminium alloy is heat treatable, its mechanical strength increases considerably during heat treatment at elevated temperatures. The different alloy series and their heat-treatability are presented in Table 2.1. This work will focus on wrought, heat-treatable aluminium alloys in the 6xxx series.

Table 2.1 Al alloy classification of wrought alloys based on their main alloying elements, applications and heat treatability [4].

Alloy series	**Alloying elements**	**Applications**	**Heat-treatability**
1xxx	None	Electrical conductors, chemical plants and architectural panels	Non-heat treatable
2xxx	Cu, Mg	Aircraft structures	Heat treatable
3xxx	Mn	Heat exchangers, packaging, architectural applications	Non-heat treatable
4xxx	Si	Architectural applications	Mainly non-heat treatable
5xxx	Mg	Car and marine applications	Non-heat treatable
6xxx	Mg, Si	Extruded and rolled products, vast number of applications	Heat treatable
7xxx	Mg, Zn	Aircraft structures and hydraulic equipment	Heat treatable

2.2 The Heat Treatment

An example of a generic heat treatment for age-hardenable aluminium alloys in the 6xxx series is shown in Fig. 2.2. The alloys are cast at temperatures above the melting point of aluminium and cooled to room temperature (RT). Dispersoids form during a homogenisation step which is performed below the eutectic temperature. The purpose of the solution heat treatment (SHT) is to dissolve any structures containing solute additions which may be present. The solute atoms will then be dispersed in solid solution, and are available for precipitation of nanosized needles during artificial ageing (AA). Usually a relatively high number of quenched-in vacancies will be present after SHT. In Al alloys, vacancy diffusion is a key mechanism in the precipitation process.

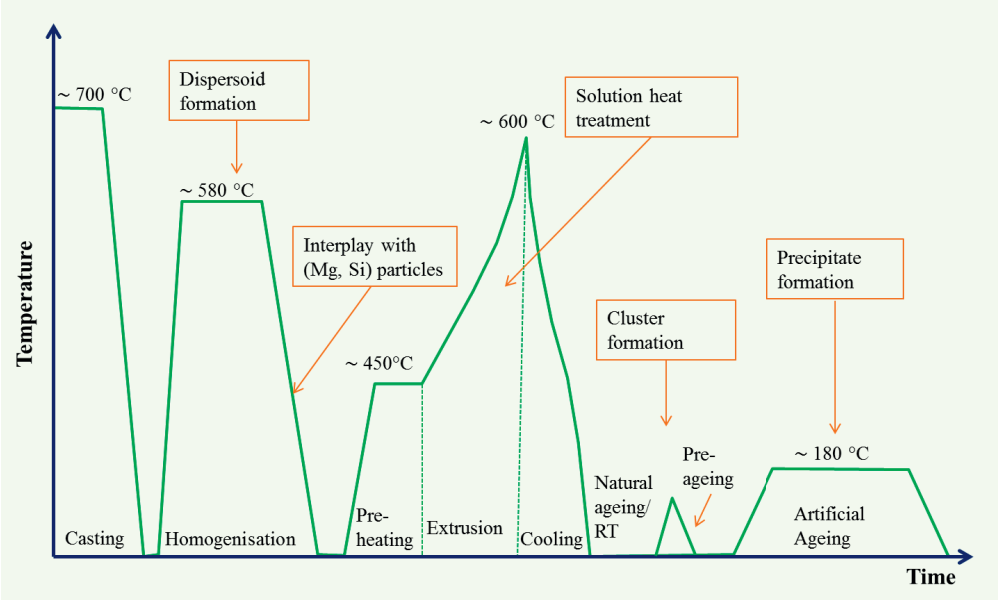

Figure 2.2 Example heat treatment for age-hardenable aluminium 6xxx alloys. The alloy is first subjected to solution heat treatment (SHT) to disperse solute atoms in the solid solution. The alloy is then quenched to room temperature (RT) and kept at this temperature for natural ageing (NA). Finally it is brought to its artificial ageing (AA) temperature, which is usually around 180 °C [2].

A pre-ageing stage (not to be confused with pre-heating in Fig. 2.2) is sometimes included after SHT and prior to AA, in order to optimize the precipitate distribution. Pre-ageing is typically conducted at temperatures ranging from 70 °C – 100 °C. During natural ageing (NA) clustering of solute additions starts in the supersaturated solid solution (SSSS). This stage, which in industry is simply the storage time between SHT and AA, can be beneficial for creating a high number of nucleation sites for precipitate growth. AA is the final step where the alloy is brought to its final strength, which is often peak strength of the material.

This is the stage where, in heat-treatable alloys, the precipitates are allowed to grow until an optimal precipitate distribution with regard to strength or other properties has been reached.

2.3 Strengthening Mechanisms

There are several mechanisms involved in the strengthening processes of aluminium alloys. The four major mechanisms contributing to strength are: work, microstructure, solid solution and precipitation hardening. These four mechanisms will be described briefly in this section.

Work or strain hardening occurs when solid material is exposed to plastic deformation. When the material is subjected to plastic deformation, it can no longer return to its original state as the atoms are permanently displaced from their equilibrium positions. Deforming material usually introduces more dislocations, and dislocation-dislocation interactions lead to a strengthening effect [5]. In aluminium, <111> Al plane dislocations are most common, while their most energetically favourable directions of movement are along <110> Al. It is the propagation of dislocations over time which causes the material to fracture. This can happen along the 12 slip systems in aluminium, along <111> lattice planes, which are also referred to as the slip planes in Al [6].

Microstructure hardening refers to dislocation impediments like grain boundaries or constituent particles. Because of this, it is desirable to design alloys with grain sizes resulting in the best material properties. A distribution of smaller grains can lead to increased hardness, but in turn this may lower the hardening effect from precipitation. It is therefore crucial to find an optimal grain-size distribution.

Solute additions may also lead to a strengthening effect of the material, see A in Fig. 2.3. When foreign atoms are dissolved in a lattice, they can act as additional obstacles to dislocation movement. Solute atoms substitute the atoms in the lattice or place themselves interstitially. The strength contribution (yield strength contribution), σ_{ss}, from elements in solid solution can be expressed as follows [7].

$$\sigma_{ss} = \sum_j k_j C_j^{\frac{2}{3}} \tag{2.1}$$

Here, C_j is the concentration of a solute element in solid solution and k_j is its corresponding scaling factor.

Precipitation hardening occurs when precipitates form during heat treatment of age-hardenable alloys. The precipitates typically grow along specific *hkl* lattice planes (or habit planes), and act as dislocation impediments when the material is strained or deformed. Hardening effects from precipitation will be further discussed in section 2.4.

It is common to simplify the total (yield) strength, σ_{tot}, of the material as a linear summation of the different contributions.

$$\sigma_{tot} = \sigma_i + \sigma_{dis} + \sigma_{ss} + \sigma_p \tag{2.2}$$

Where σ_i is the intrinsic strength of pure aluminium, $\sigma_{dis}$is the contribution from dislocations (work hardening), σ_{ss} is the solid solution hardening and σ_p is the hardening contribution from precipitation.

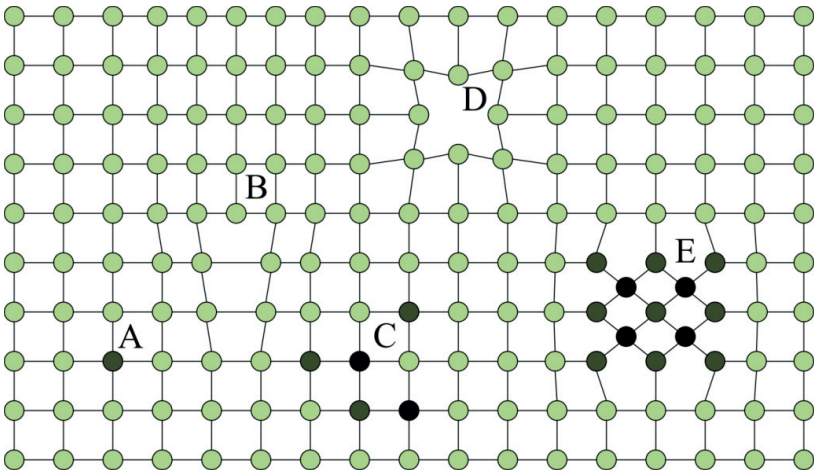

Figure 2.3 Crystallographic defects in a generic lattice. A: substitutional solute atom, B: end dislocation, C: solute atom cluster, D: vacancy and E: precipitate phase. Adapted from Wenner [8].

2.4 Precipitation Hardening

Precipitates are the main strength contributors in Al 6xxx alloys, and tend to grow into cubes, plates, needles or other characteristic shapes, see Fig. 2.4. Usually, the first phases to form are coherent with the Al matrix and lose coherency as they grow. Before the equilibrium phases form, there is a sequence of other metastable phases forming during AA. The theory in this section is based on [6], which gives a complete explanation of the different mechanisms at hand.

When precipitates interact with dislocations, they make slip more difficult and consequently the strength of the material increases. The basic mechanisms of precipitate-dislocation interactions are Orowan bowing (looping) and particle cutting. The Orowan bowing

mechanism describes dislocations looping particles in solid solution. The two mechanisms are illustrated in Fig. 2.5.

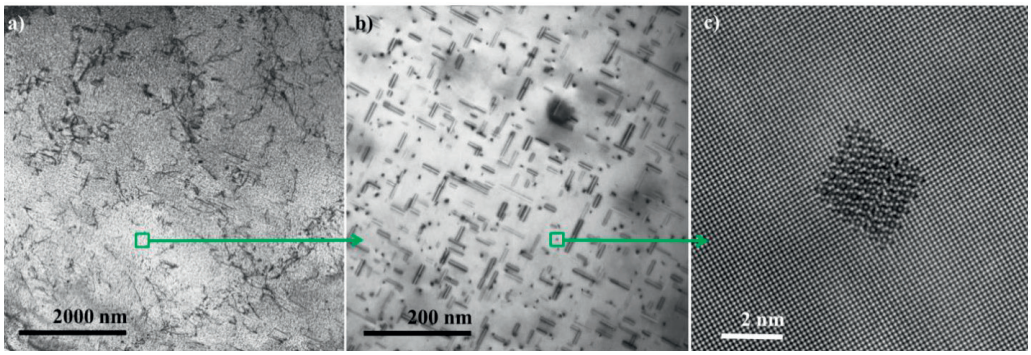

Figure 2.4 TEM images from the centre of a grain in a common Al 6xxx alloy at different magnifications. **(a)** overview bright field TEM image. The green square indicates the size of image (b). **(b)** TEM bright field image clearly showing precipitate needles. The green square indicates the magnification of image (c). **(c)** HAADF-STEM image of a precipitate cross section growing into the plane. The cross section is *β"* type. 'Smart Align' [9] has been applied in (c).

Dislocations bypassing precipitates bow out when they encounter each other. When a dislocation bows out as it moves through the Al lattice, it may encounter itself at the opposite side of the particle. When the dislocation "encounters itself" at the other side of the particle it is of opposite nature and annihilates, causing the looping dislocation to separate from the "parent-dislocation", see Fig. 2.5. As an effect of this mechanism, reducing the spacing between precipitates causes an increase in material strength. Simultaneously, small spacing between precipitates is often associated with the precipitates becoming smaller, which in turn lowers the energy required for particle looping.

When the precipitates are not able to impede dislocation movement by looping, the dislocation can instead glide through them, essentially "cutting" its way through. The simple explanation would be that small particles are sheared while larger particles are looped. The strain field of the dislocation interacts with that of the precipitate particle and results in a repulsive force between the two strain fields. The dislocation requires additional energy for cutting through the precipitate particle, after overcoming the two repulsive strain fields, which is why the strength contribution from this mechanism is dependent on the precipitate size distribution.

The looping and cutting contributions from precipitates to strength can be described assuming the precipitates are spherical and of identical sizes. This approximation is surprisingly similar to the contribution from needle shaped precipitates, which is why a spherical precipitate approximation can be used [7]. Based on the previously mentioned simplifications, the contribution to strength from precipitation can be expressed as

$$\sigma_p = \frac{M\bar{F}}{bl} \tag{2.3}$$

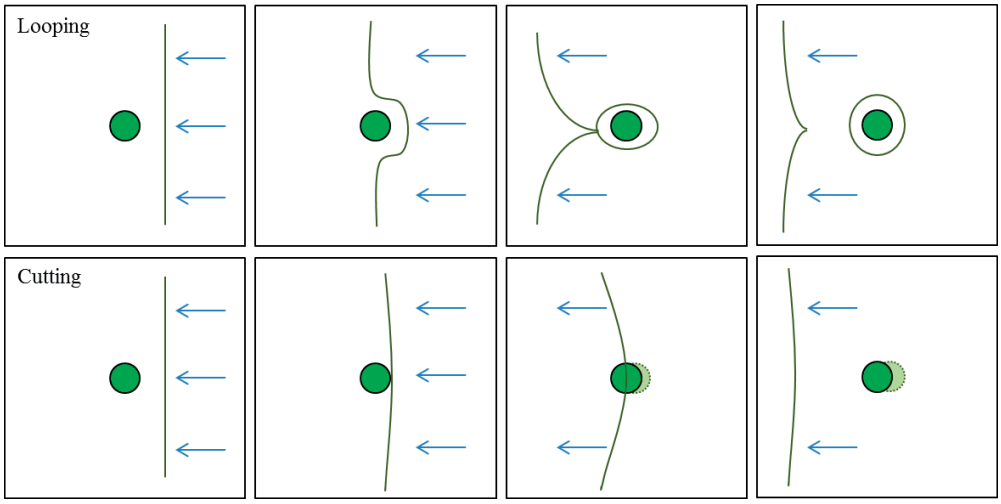

Figure 2.5 Illustration of the two most important interaction mechanisms between dislocations and precipitates in aluminium alloys: particle looping and particle cutting. The dislocation moves from right to left in both cases and encounters a particle illustrated in green.

M is the Taylor factor, $\bar{F}$ is the mean interaction force between dislocations and precipitates, l is the mean effective particle spacing and b is the Burgers vector. If l is further expressed by the mean particle size, $\bar{r}$, and the volume fraction of precipitates, f, we get Eq. 2.4 [7].

$$\sigma_p = \frac{M}{b\bar{r}}(2\beta G b^2)^{-\frac{1}{2}}\left(\frac{3f}{2\pi}\right)^{\frac{1}{2}}\bar{F}^{\frac{3}{2}} \tag{2.4}$$

β is a constant close to 0.5 and G is the shear modulus of the aluminium matrix. Normally we are dealing with a mixture of shearing and bypassing of precipitates for aluminium alloys, which is why the mean interaction force $\bar{F}$ is referred to as a sum of the different contributions, see Eq. 2.5.

$$\bar{F} = \frac{\sum_i N_i F_i}{\sum_i N_i} \tag{2.5}$$

Here, N_i is the number of particles per unit volume within the size class r_i and F_i is the mean interaction force between dislocations and precipitates within size class r_i. In the case of shearing, when r_i is smaller than the critical radius, r_c, of the precipitates where shearing can occur, the mean obstacle strength is given as in Eq. 2.6.

$$\bar{F} = 2\beta G b^2 \left(\frac{r_i}{r_c}\right) \tag{2.6}$$

For dislocations bypassing the particles, the mean obstacle strength can be assumed to be constant and independent of the particle size.

$$\bar{F} = 2\beta G b^2 \tag{2.7}$$

2.5 Precipitate Phases

There are several aspects contributing to the formation of precipitates in aluminium alloys, e.g. ageing temperature and its duration, alloy composition, deformation, impurities and vacancy concentration. Overall, the processes of alloy design is quite complex and not all aspects can be discussed here.

The solid-to-solid phase transformation mainly enables a new phase, different from the parent phase, to form. For aluminium precipitates, the composition and volume of the new phases differ from the parental phase. Precipitates often nucleate heterogeneously, which means they nucleate at discontinuities in the parent matrix because of a lower energy barrier. New precipitate phases can also form uniformly throughout the matrix, i.e. by homogeneous nucleation. The volume of the newly formed precipitate usually deviates from that of the original phase. Consequently, contraction or expansion of the matrix will require additional energy for the phase to form.

At the beginning of the heat treatment solute atoms are distributed in a SSSS. Atomic clustering then starts, typically during RT storage or NA. When AA is performed, fully coherent Guinier Preston (GP)-zones start to develop. When the material reaches peak hardness, the microstructure is usually found to consist of a high number density of metastable, finely dispersed GP-zones and *β''* type precipitates. If the ageing is allowed to continue, *β'*, *U1*, *U2* and *B'* replace *β''*. These precipitates have the potential to grow to larger sizes, but provide a lower strength than *β''*. The precipitation sequence changes when other elements are added or when strain is introduced to the material [10] [11]. Finally, the

stable equilibrium phases β and Si will be the only phases left if AA has sufficient duration. The precipitation sequence in ternary, unstrained Al-Mg-Si alloys is generally given as [12].

SSSS → atomic clusters → Guinier-Preston zones (pre-β'') [13] [14] [15] → β'' [16] [17] → β' [18], *U1* [19], *U2* [20], *B'* [21] → β, Si (stable)

The remainder of this section will focus on vacancies, dislocations and relevant solute additions and their effects on precipitate types, microstructure and the resulting macroscopic properties of the alloys.

The crystal structure of the most common precipitate phases in Al-Mg-Si alloys are listed in Table 2.2 with corresponding compositions, space groups and lattice parameters.

Table 2.2 Overview of precipitate phases in the Al-Mg-Si system.

Phase	Composition	Space group	Lattice parameters [Å]
GP-zones	$Mg_{2+x}Al_{7-x-y}Si_{2+y}$	C2/m	$a = 14.8$, $b = 4.05$, $c = 6.48$, $\beta = 105.3°$
β''	$Mg_8Si_8Al_6$	C2/m	$a = 15.16$, $b = 4.05$, $c = 6.74$, $\beta = 105.3°$
β'	$Mg_{1.8}Si$	$P6_3$	$a = b = 7.15$, $c = 4.05$, $\beta = 120°$
U1	$MgAl_2Si_2$	$P\bar{3}m1$	$a = b = 4.05$, $c = 6.74$, $\beta = 120°$
U2	MgAlSi	Pnma	$a = 6.75$, $b = 4.05$, $c = 7.94$
B'	Probably $Mg_9Al_3Si_7$	Hexagonal	$a = b = 10.4$, $c = 4.05$, $\beta = 120°$
β	Mg_2Si	$Fm\bar{3}m$	$a = 6.35$

2.5.1 Vacancies

Vacancy clusters and dislocations have significant influence on the nucleation of precipitate needles. Vacancies attract solute atoms, are needed for substitutional diffusion and may be their own source for clustering. Solute atoms and vacancies can attract each other and act as a diffusion-pair. This is often referred to as the 'vacancy pump mechanism' where vacancies bring solute atoms to regions of higher solute concentration, before disconnecting and performing the same routine again and again [22]. Recently, calculations based on DFT have showed how the vacancy binding energy for alloying elements in aluminium increases with atomic sizes [23], with some exceptions. Solute-vacancy binding energy relates to the probability of a vacancy surrounding the solute atom for a period of time. Higher binding

energy means there is a higher probability of the vacancy to stay in the vicinity of the solute atom. Several simulations have been done for interaction energies in this work [24], some of which are shown in Fig. 2.6.

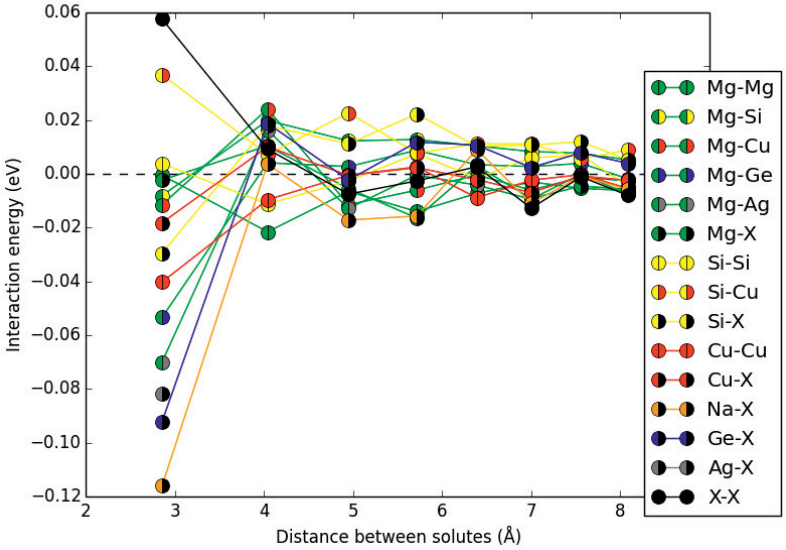

Figure 2.6 Interaction energies between the alloying elements and/or vacancies (X) in fcc aluminium as a function of separation distance, from 1st to 8th nearest neighbours. Extended from results presented in [24]. The simulations have been completed by Jesper Friis.

When there is an excess of quenched-in vacancies available in an alloy, they are found to form clusters and voids. In particular, 'prismatic clusters' consisting of vacancies are found to appear (Frank loops) [25] [26]. This observation is additionally supported by calculations which show that a few vacancies can form a prismatic dislocation loop when clustering on a {111} Al plane [27] [28]. However, dislocations may also aid the process of vacancy annihilation. Adding elements with high vacancy bonding energies should reduce the ability of the material to form loops and consequently the dislocation density drops [29]. Dislocations usually cause the precipitation to be more inhomogeneous, because it is energetically favourable for solute atoms to cluster and for precipitates to continue growing on dislocation lines.

2.5.2 Effect of Solute Additions on Precipitation in 6xxx Alloys

Solute additions can have many different effects on the precipitation kinetics and accordingly the material properties. There are several things to consider before mixing random elements into aluminum and hoping for the best. How will the solute atom interact with other solutes and vacancies? Will the atoms contract or expand the aluminium lattice? How will the charge

distributions between atoms look like? These are the atomistic issues which help explain the reasons behind precipitate formation.

Silicon and Magnesium

Si-rich alloys with an approximate Si to Mg ratio of 6/5 stabilises the well-known *β"* phase [30]. Mg-rich alloys on the other hand, seems to create a coarser precipitate distribution consisting of a mixture between *β"* and precipitate phases associated with over-ageing of the material, even at peak-aged conditions. The total Si and Mg additions affect the types of clusters which are able to form during NA of the material. There are two types of clusters forming, popularly featured as "good" or "bad" clusters. The "good" clusters seem to have an approximate Si/Mg ratio of 1. It has been reported that if Si + Mg < 1 wt %, RT storage enhances precipitation kinetics as opposed to artificially ageing the alloy directly [31]. If Si + Mg > 1 wt %, RT storage causes a lower strength than if the alloys had been subjected to AA directly after quenching. This lowered strength is a consequence of "bad" clusters retarding the precipitation sequence during AA [31].

At first glance it might seem like there are few connections between the different phases in Al-Mg-Si alloys. However, all metastable precipitates in this system are connected through a projected hexagonal network of Si atomic columns [32], the only exception being the main hardening phase, *β"* itself. By using this network of Si columns as a basis, the building-block approach by Ehlers et al. [33] explains all observed precipitate phases. Since the network is an integral part of all precipitates it is reasonable to think these elements are already in the clusters in the early stages of precipitation. The prevalence of the network means it must be initiated early, which means Si has an important role from the very start. *β"* has a distorted network of Si columns, where the columns arrange themselves so that a triangular Si-network exists across parts of the phase. It has been speculated that the reason Mg and Si combine in clusters, is to cancel the differences in the vacancy binding energy [34].

Lithium

The solid solubility of Li in aluminium is high, and because of its low density, adding it to Al will lower the density of the aluminium alloy [2]. It has been discovered that Li willingly diffuses to the surface of the alloy and a Li depletion can occur deep into the material surface when heat treating in air [35]. Li atoms are thought to diffuse to the surface faster than Al atoms can replace them in the crystal lattice. Because of this rapid Li diffusion from bulk to surface, an increased amount of vacancies which often agglomerate is expected close to the alloy surfaces [35].

It has been shown in previous studies that small additions of Li to Al-Mg-Si alloys increase the age-hardening response [36]. Li enters the precipitate needle structure, but it does not change the precipitation sequence. Consequently the *β"* phase is still the main hardening precipitate at peak hardness conditions for these alloys. Adding Li to these alloys systems seem to cause a denser precipitate distribution consisting of smaller needles. An example atomic overlay of a precipitate in a Al-Mg-Si-Li alloy (RXL0) is given in Fig. 2.7. The symbolic representation of elements and heights are given in Table 2.3.

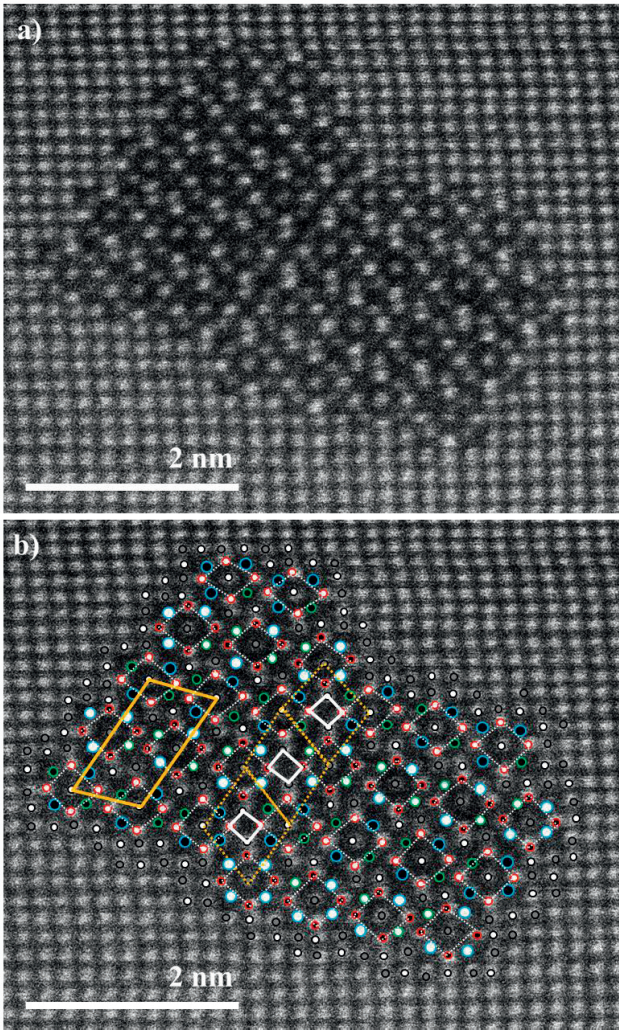

Figure 2.7 HAADF-STEM raw images of a precipitate cross section in an Al-Mg-Si-Li alloy (RXL0). (b) Atomic overlay of the precipitate cross section from (a). A *β"* unit cell is indicated with solid yellow lines. Examples of the β_2*"* stacking variations (see Table 2.5) are indicated with dashed yellow lines. The white solid lines indicate the location of "vacated atomic columns". Symbolic representation of elements is given in Table 2.3.

Table 2.3 Symbolic representation of elements used for the atomic overlay presented in Fig. 2.7.

Elements / Height	Al	Si	Mg	Li
z = 0.000 nm	○	○	○	○
z = 0.203 nm	●	●	●	●

Copper

It is common to find traces of Cu from recycling in Al-Mg-Si alloys, but it is also commonly added on purpose by industry because it improves the material strength. Although the strength increases, Cu additions down to 0.1 wt % can cause inter-granular corrosion [37] [38] [39]. Consequently, the Cu addition has been kept at 0.05 wt % in this study. When it comes to precipitate phases, Cu has been found to substitute Al and Si sites within the precipitate but it also occupies sites at the precipitate interfaces. By adding Cu to Al 6xxx systems, the formation of the *β''* phase is suppressed and other phases start to form, an overview is given in Table 2.4. The precipitation sequence in Cu-added 6xxx alloys is generally given as [40] [41] [42] [43] [44]:

SSSS → atomic clusters → Guinier-Preston-zones (pre-*β''*) [13] [14] → *β''* [18], L, S, C, QP, QC → *β'*, Q' → Q

Table 2.4 Overview of precipitate phases in quaternary Al-Mg-Si-Cu alloys.

Phase	Composition	Space group	Lattice parameters [Å]
QP	Unknown	Hexagonal	$a = b = 3.93$, $c = 4.05$
QC	Unknown	Hexagonal	$a = b = 6.70$, $c = 4.05$
C	$\approx Mg_4AlSi_{3.3}Cu_{0.7}$	$P2_1/m$	$a = 10.32$, $b = 8.1$, $c = 4.05$, $\beta = 101°$
L	Variable	Disordered	Variable
Q'	Probably $Al_3Cu_2Mg_9Si_7$	Probably $P\bar{6}$	$a = b = 10.32$, $c = 4.05$, $\beta = 120°$
Q	Probably $Al_3Cu_2Mg_9Si_7$	$P\bar{6}$	$a = b = 10.39$, $c = 4.02$, $\beta = 120°$

The problem with intergranular corrosion in Al-Mg-Si-Cu alloys is related to precipitate phases that are disposed to corrosion, especially the Q-phase [44], which nucleates on grain boundaries [38]. It has also recently been found that Cu forms film-like enrichments along the grain boundaries, also promoting inter-granular corrosion [38].

Cu can substitute both Al and Si in the precipitate structures and at the precipitate/matrix interfaces [45] [33]. For example, *Q'* and *Q* are isostructural with *B'* [44], where Cu has substituted some partly occupied Al-positions [21]. Unlike the binary Al-Si system (or Al-Ge), where only pure Si (Ge) precipitates form, in 2xxx alloys Cu combines with Al in the Al-Cu system. For example, the Al-Cu system is prone to form the hardening precipitates *θ'* - Al_2Cu [46]. For this reason alone Cu might be expected to have a strong effect on nucleation when added to other Al-based systems. In 6xxx alloys Cu suppresses the formation of pure

β'' by promoting disorder in the precipitate structures as well as inducing other precipitate types [40] [41] [42]. This is not necessarily a disadvantage as the new precipitates promotes hardening, and precipitate number densities and volume fractions do not decrease relative to total solute amount [40] [47].

Silver

A reason for adding Ag to 6xxx aluminium alloys is that small additions in several age-hardenable Al based alloys containing Mg have been found to stimulate GP-zone formation and precipitation. In general, Ag tends to accelerate the kinetics of the age-hardening response and increases the material's peak hardness [29] [2]. For example, binary Al-Mg alloys with Mg below ~10 wt % are practically non-heat-treatable. By adding 0.5 wt % of Ag a significant hardening response has been observed [29].

In pure form Ag, Al and Cu all form fcc structures. They have significant differences in bonding, which is quite obvious just by considering the composition of their normal oxides: Ag_2O, Al_2O_3 and CuO. Since Al and Ag are similar in size, precipitation may be compared in binary Al-Cu and Al-Ag alloys. Although the first precipitates to form in both systems are plates, in Al-Cu they form on (100) Al planes [32], while in Al-Ag they grow on (111) Al planes [48]. This shows that, even if Ag is more similar to Al than Cu regarding size and oxidation properties, Ag should not be considered a sole replacement for Al. In fact, TEM has shown that in precipitates of the 6xxx system Ag occupies Al positions by enriching the matrix outside precipitates, as well as replacing Si-positions within the precipitate structures [49]. Moreover, in Al-Cu-Ag, Cu and Ag are not found to mix well [50]. Here, Ag only goes to precipitate interfaces or segregates in the matrix. According to Kim et al. Ag or Ag and Cu additions to dense Al-Mg-Si alloys (with a total of about 0.10 at %) clearly affect the age-hardening behaviour and increases peak hardness when the material is aged at 443 K (170 °C) [51]. During over-ageing, Ag causes β'_{Ag} to form, which has structure and composition differing from the normal β' phase in Al-Mg-Si alloys [49]. If similar size and identical (fcc) structure to Al are the only criteria, more Ag in solid solution in a 6xxx alloy is unlikely to require extra energy during extrusion. Recently, it has been found that elongation improves with Ag additions [52], a result which could indicate improved extrudability.

Germanium

Ge is chemically similar to Si, but is a larger and heavier atom. The replacement of Si with Ge in Al-Mg-Si alloys has been investigated in former studies [53] [54]. One of the effects is a general refinement of the precipitation, with a following increase in hardness. When observed in the precipitate structures Ge has been found to occupy the same positions as Si. Just as Si, Ge forms a projected hexagonal network of columns along <100> Al, which is well integrated in the matrix and common for the Ge-Mg-(Al) containing precipitates. It seems Si and Ge substitute each other in the network columns. Increasing the Ge amount creates more disordered precipitates on an otherwise ordered network. Full replacement of Si by Ge prevents the formation of the β'' phase altogether. Instead, the material gains strength

by precipitates isostructural to those of the ternary Al-Mg-Si system which are not normally associated with hardening; *U1*-like and *β'*-like precipitates are found alongside a high fraction of disordered precipitates [54].

By replacing only a fraction of Si with Ge, the eye-like features in *β"* seems to be the main building blocks, with segments of a hexagonal Si/Ge network incorporated in the structure. The stacking of *β"* eyes seem to be interchangeable, and several stacking variations have been reported [24]. Three of the most commonly occurring stacking variations are presented in Table 2.5 with corresponding compositions, space groups and lattice parameters.

Table 2.5 Overview of *β"* precipitation variants in the Al-Mg-Si-Ge system. D denotes a mix of Ge and Si. Vacated columns are here denoted X and should not be confused with a single vacancy.

Phase	Composition	Space group	Lattice parameters [Å]
β"	$Mg_8D_8Al_6$	C2/m	$a = 15.16$, $b = 4.05$, $c = 6.74$, $\beta = 105.3°$
β$_2$"	$Mg_8D_8Al_6X_2$	C2/m	$a = 12.15$, $b = 4.05$, $c = 8.1$, $\beta = 90°$
β$_3$"	$Mg_8D_8Al_{10}$	C2/m	$a = 15.16$, $b = 4.05$, $c = 10.33$, $\beta = 135°$

The L phase discovered in Al-Mg-Si-Cu alloys [47] also seems to dominate at peak hardness in Al-Mg-Si-Cu-Ge alloys [55]. As a direct cause of this phase, in a high-strength Al-Mg-Si-Cu alloy, when adding Ge in low concentrations (0.13 wt %), both thermal stability and peak hardness improved [47]. Additionally, if only 10 % of the Si amount is replaced by Ge, precipitate number density increases quite significantly, and precipitates become finer.

Chapter 3

Experimental Techniques

A large part of the results presented in this thesis is based on experimental work. As the main features to be investigated are nanometre sized precipitate needles, advanced electron microscopy and spectroscopy methods have been applied. In particular, TEM, HAADF-STEM and EELS will be presented here as they have been the most important tools used for characterization. PES will also be presented, focussing on x-ray photoelectron spectroscopy (XPS) and x-ray photoemission electron microscopy (XPEEM), which were the techniques applied in paper 7.

3.1 Transmission Electron Microscopy (TEM)

TEM is in many ways comparable to optical, light microscopy. The most obvious differences are the use of electrons instead of light and electromagnetic lenses instead of glass-lenses. The electromagnetic lenses are stationary in TEM, and we rely on the possibility of adjusting their strength instead of moving them up and down like in optical microscopes. Not surprisingly, the spatial resolution of electron microscopes is much better than that of light microscopes because of the short wavelengths of high energy electrons. Mostly solid state samples are studied by TEM, but new advances allow also biological samples, gases and liquids to benefit from TEM techniques. The requirement of ultra-thin samples for TEM is an obvious limitation of this tool. In this context, ultra-thin may be understood as ‘electron transparent’, which is typically 100 nm or less for aluminium alloys.

3.1.1 Conventional TEM

The ray-diagram in Fig. 3.1 illustrates how a basic TEM works. The electrons are emitted from a source, which can be a thermionic or a field-emission source. A thermionic source is usually made from Tungsten or a LaB_6 crystal, which produces electrons upon heating. Field-emission sources (FEGs) emit electrons when an electrical potential is applied between itself and an anode, and gives more monochromatic electrons than thermionic sources. The electrons are accelerated to energies typically in the range from 60-300 keV by an electric field [56]. The entire microscope column is under vacuum and electromagnetic lenses control the electron trajectories.

The condenser aperture allows us to select the most coherent electrons, which are usually the ones closest to the optical axis in the microscope. More lenses then focus the beam in order to create a diffraction pattern or an image of the sample-plane. Finally, the magnified image can be observed on a viewing screen or CCD camera, or the transmitted electrons may be detected by e.g. bright field, dark field or spectroscopy detectors.

The resolution of a conventional TEM is often described by the Rayleigh criterion, which expresses the smallest spatial distance which can be resolved, δ [56].

$$\delta = \frac{0.61\lambda}{\mu \sin\beta} \tag{3.1}$$

Where λ is the wavelength of the electrons, μ is the refractive index and β is the collection angle of the magnifying lens.

In a TEM the interaction between electrons and sample is typically strong; for thick specimens one has to assume the electrons experience more than one scattering event. There are many possible interactions which can occur when an electron travels through the sample. The most important ones are illustrated in Fig. 3.2 and can be divided into elastic and inelastic interactions. It is common to refer to electrons in an electron microscope as ionizing radiation because of their ionizing nature when interacting with the sample. Most of the electron-sample interactions can be detected and used for characterizing the sample.

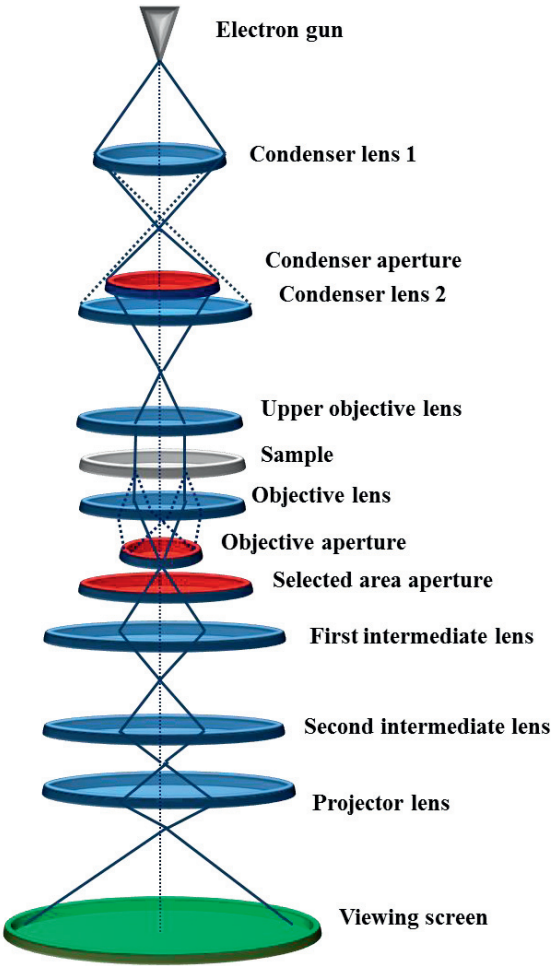

Figure 3.1 Schematic of a conventional TEM setup. In this illustration the electrons travel from top to bottom. Adapted from [56].

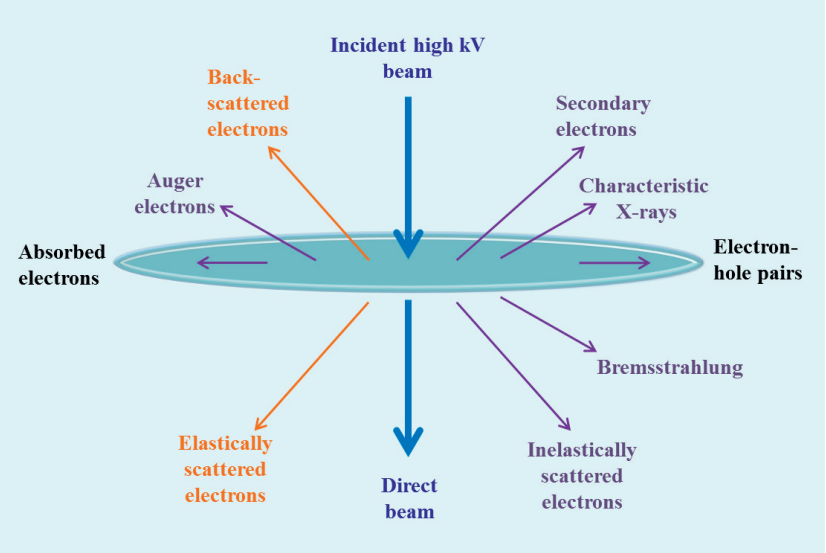

Figure 3.2 Electron-specimen interactions where the specimen is very thin. The figure has been adapted from [56].

3.1.2 Diffraction

When investigating materials incorporating multiple phases and small particles, a TEM is often the preferred tool. Since TEMs can switch between real and reciprocal space, it is a suitable tool for phase determination and orientation relationships. In this work diffraction has mainly been used to determine the [100] Al zone axis, exemplified in Fig. 3.3, as this is the most convenient crystal orientation for viewing precipitates in 6xxx alloys.

By starting to consider a single elastic scattering event by a single atom, the energy state of the atom will not change. In TEM the electrons emitted from the source have high kinetic energy and will be scattered by the atomic potential when interacting with the sample. The resulting scattering intensity $I(\theta)$ is then given by Eq. 3.2.

$$I(\theta) = |f(\theta)|^2 \tag{3.2}$$

Where $f(\theta)$ is atomic scattering amplitude as a function of distance from the scattering atom. $I(\theta)$ is a quantifiable and a very important quantity in TEM.

In a perfect periodic crystal, scattered waves from several atoms interfere, resulting in diffraction maxima and minima. In TEM this means that electrons scattered from parallel crystal planes will be focused to points in the back-focal plane of a lens below the sample. Diffraction maxima can be expressed by Bragg's law, see Eq. (3.3).

$$2dsin\theta = n\lambda \tag{3.3}$$

Where d is the spacing between adjacent parallel planes, θ is the angle between the incident beam and the crystal plane, n is an integer and λ is the wavelength. The distance between hkl planes in real space, where a is the lattice constant of a cubic crystal, can also be expressed as follows.

$$d_{hkl} = \frac{a}{\sqrt{h^2 + k^2 + l^2}} \tag{3.4}$$

The intensity of a Bragg reflection is dependent on the structure factor F_{hkl}. The structure factor can be expressed as

$$F_{hkl} = \sum f_j e^{-2\pi i(\mathbf{r}_j \mathbf{g}_{hkl})} = \sum f_j e^{hx_j + ky_i + lz_j} \tag{3.5}$$

Summed over all atoms present in the basis of the lattice. The vectors $\boldsymbol{r}_j$ and $\boldsymbol{g}_j$ are the position of the j'th atom in the unit cell and the j'th reciprocal lattice vector respectively. f_j is the scattering factor. In the case of aluminium, if the indices are partly even and partly odd, the structure factor becomes 0 and consequently the reflection will be extinct. However, if all indices are even or if all indices are odd, the structure factor equals $4f$ and the reflections appear.

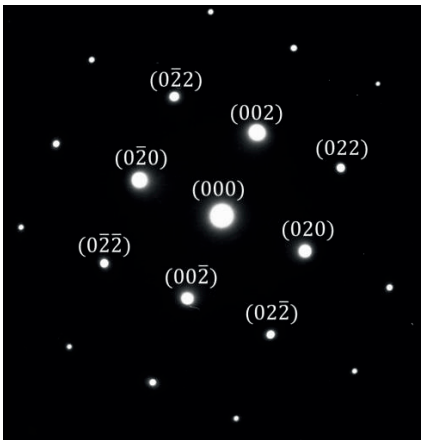

Figure 3.3 Diffraction pattern of the [100] Al zone axis. Some of the reflections, corresponding to parallel planes in Al, are indexed in the pattern.

3.1.3 High Resolution TEM

The high resolution (HR) imaging mode in TEM relies on the interference between the direct and diffracted beams, also known as phase contrast imaging. Contrast reversal complicates the imaging process, and can be expressed by 'the object transfer function for the process of image formation', $T(\vec{u})$, see Eq. 3.6 [56]. Contrast transfer mathematically describes how the image of the specimen is modified by aberrations that are present in HR-TEM.

$$T(\vec{u}) = A(\vec{u})E(\vec{u})2\sin(\chi(\vec{u})) \tag{3.6}$$

Here, $\vec{u}$ is the spatial frequency for a diffracted direction (a reciprocal lattice vector), $A(\vec{u})$ is the aperture function and $E(\vec{u})$ is the envelope function which includes the chromatic effects occurring from the objective lens in addition to the spatial coherence of the electron gun. In practise, both the aperture function and the envelope function cut off high spatial frequencies. The phase of the electrons that form the image can be distorted; this effect can be expressed by the 'phase distortion function' $\chi(\vec{u})$, as in Eq. 3.7.

$$\chi(\vec{u}) = \pi\Delta f\lambda\vec{u}^2 + \frac{1}{2}\pi C_s\lambda^3\vec{u}^4 = \frac{2\lambda}{\lambda}(C_s\frac{\lambda^4\vec{u}^4}{4} + \Delta f\frac{\lambda^2\vec{u}^2}{2}) \tag{3.7}$$

Where Δf is the amount of defocus used for image formation, C_s is the spherical aberration and λ is the electron wavelength.

When $T(\vec{u})$ is negative, the phase contrast will be positive, causing the atoms to appear dark with a bright background. An example of contrast reversal in TEM is given in Fig. 3.4. To illustrate phase contrast imaging further, a state-of-the-art HR-TEM image of a precipitate cross section is given in Fig. 3.5.

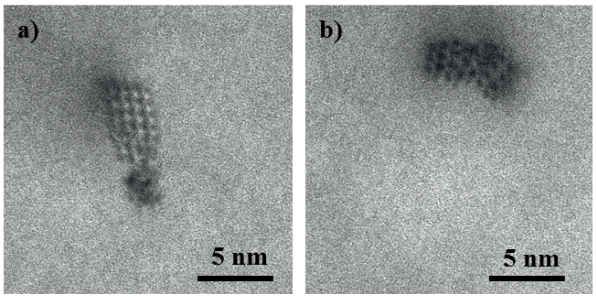

Figure 3.4 Contrast reversals in TEM. **(a)** The features appear bright on a darker background, suggesting $T(\vec{u})$ is positive. The precipitate cross section most likely consists of *β''*eye-like features. **(b)** The features appear dark on brighter background, suggesting $T(\vec{u})$ is negative. Both images are taken in a Philips CM30 operated at 150 kV, the precipitates are from the same micrograph ~ 20 nm apart.

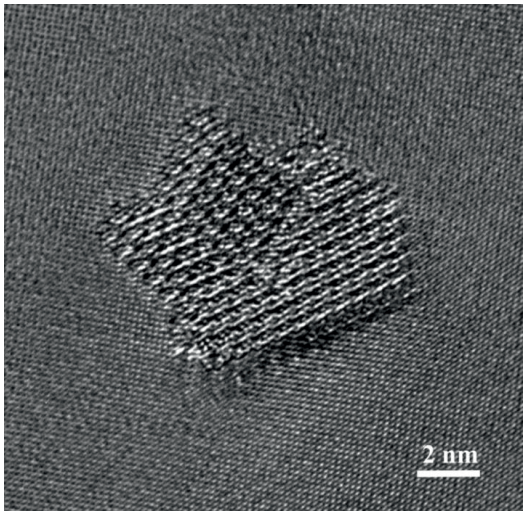

Figure 3.5 HR TEM image of a precipitate cross section in a lean Al-Mg-Si alloy. The aluminium lattice can be observed in two <001>Al directions in this image.

3.2 Scanning Transmission Electron Microscopy (STEM)

In STEM, the incident electrons are focussed to a probe which is scanned across the sample, and the transmitted electrons can be detected at different scattering angles. A simplified illustration of STEM is given in Fig. 3.6, also illustrating the different detectors that are typically used. There are several unique signals one can take advantage of in HR-STEM. Bright field (BF) STEM has similar contrast to BF-TEM while annular dark field (ADF) and HAADF-STEM offers Z dependent contrast. The BF and HAADF detectors integrate the signal over small and large scattering angles respectively, in the back-focal plane [56]. The intensity of each pixel position in the HAADF detector directly corresponds to the scattering strength of the same location in the sample. The intensity approximately follows Z^2, meaning heavy elements are more probable to scatter to higher angles [57].

In STEM the main resolution limiting factor is the size of the focussed beam, which is dependent on the coherency of the electron beam. The coherency of the electron beam is determined by the coherency of the electron source itself and the quality of the lenses in the microscope. An infinitely sharp feature in the sample will be blurred in non-perfect imaging systems; this "point-spread" can be expressed by the point spread function (PSF), as in Eq. 3.8 [58].

$$I(r) = O(r) * PSF(r) = \delta(r) * PSF(r) = PSF(r) \tag{3.8}$$

Where $I(r)$ is the image function, $O(r)$the object function and $\delta(r)$ is a Dirac delta function for the impulse response.

The contrast transfer function (CTF) describes the transferred beam in the post-sample optics in a TEM. The PSF on the other hand describes what is happening in the pre-sample optics, and is basically the Fourier transform of the CTF.

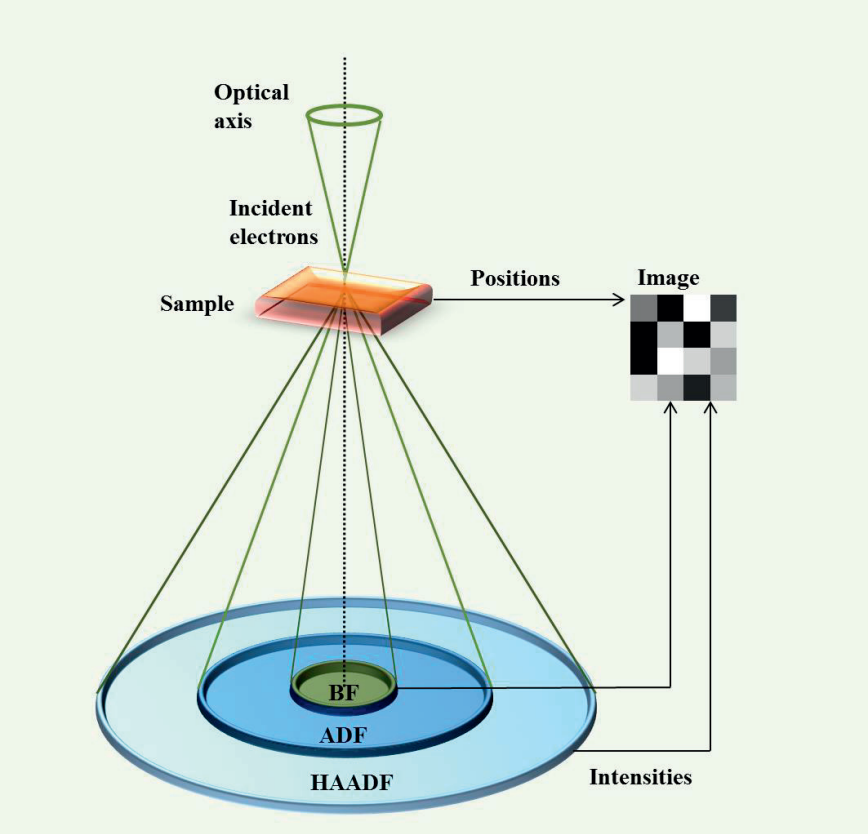

Figure 3.6 Schematic of a STEM setup with a bright field (BF), annular dark field (ADF) and high angle annular dark field (HAADF) detector.

3.2.1 Aberrations

As the electrons spiral about the optical axis in the TEM column, they may be subjected to astigmatic effects. Astigmatism and other aberrations occur if the electromagnetic lenses form non-uniform magnetic fields, or they might be consequences of the apertures and how they are introduced to the lenses. Consequently, the way the lenses affect resolution is determined by the aberrations arising as the beam travels through them.

The on-axis aberrations can be separated into different components, all incorporating distinct symmetries. The shapes of lower order components up to third order of axial aberrations are given in Fig. 3.7 for illustration.

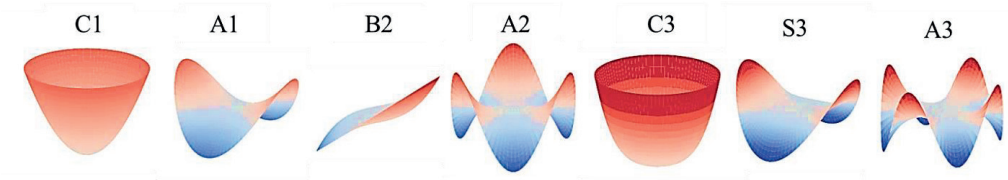

Figure 3.7 On-axis aberration components in 3D up to third order. Adapted from Fauske [59].

The geometrical aberration components from Fig. 3.7 can briefly be described as follows, with respect to image plane coordinates [59].

- C1 mainly describes the effect of defocus and its shape is symmetrically quadratic. In practice, this component makes a parallel beam parabolic.
- A1, A2, A3 are astigmatic with 2-fold, 3-fold and 4 fold azimuthal symmetry respectively.
- B2, also called axial coma[1]. Coma is an effect that makes a point in the specimen appear to have a "tail" when imaged. This effect is due to incorrect focus of beams that enter aperture planes at an angle. This aberration is parasitic as it arises from imperfect lenses or misalignments.
- C3 is commonly known as spherical aberration. Spherical aberrations basically focus beams entering the lenses at different angles to different points. C3 is symmetric to the fourth power.
- S3, also called the 'star aberration', is dependent on the coordinates in the image plane to the fourth power, with a 2-fold symmetry.

It is possible to compensate for astigmatic effects, and state of the art TEMs often has additional lenses that introduce compensating fields. The aberration correctors can be quadrupole, hexapole or octupole lenses which are located in the condenser lens system and the objective lens. It is important to remember however, that after compensating for spherical aberrations, chromatic aberrations become the next most persistent aberrations.

In ideal lenses, all rays emerging from a point in the sample should be focused to a conjugate point in the image plane. For a real lenses there are two aberrations dominating in uncorrected microscopes, both in TEM and STEM mode: spherical and chromatic aberrations. Spherical aberration causes rays entering the lens at high angles to be brought to a premature focus, see Fig. 3.8 (a). Because of this decrease in focal distance of the lens, as a function of the distance to the optic axis, we obtain a 'disk of least confusion'. The disk of least confusion, δ_s, can be expressed by Eq. 3.9. δ_s is dependent on the spherical aberration

[1] The term 'coma' is used because tilted waves will resemble a comet-like feature with a tail when focussed in the image plane.

coefficient, C_S, which is a constant length for a particular lens. β is here the maximum collection angle of the objective aperture.

$$\delta_s = \frac{1}{4} C_S \beta^3 \tag{3.9}$$

Chromatic aberrations on the other hand, cause electrons of different energies to have dissimilar focus points along the optic axis. This gives us the disk of least confusion dependent on the chromatic aberrations, δ_C [56].

$$\delta_C = C_C \beta \frac{\Delta E}{E_0} \tag{3.10}$$

Where C_c is the chromatic aberration coefficient of the particular lens, E_0 is the initial beam energy and ΔE is the energy loss of the electrons.

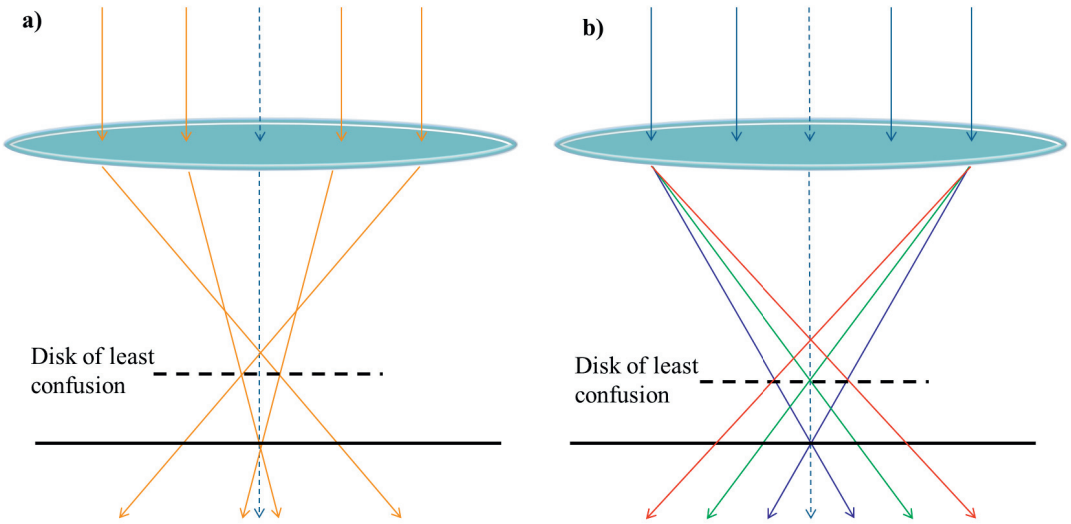

Figure 3.8 (a) Spherical aberrations (b) Chromatic aberrations. Adapted from [56]. The Gaussian image plane is indicated by the horizontal black solid line. The optic axis is indicated by blue dashed arrows.

3.2.2 Challenges in HR-STEM of Aluminium Alloys

There are several challenges when it comes to experimental work in HR-STEM and its related techniques. Some of the most tenacious challenges when working with lean aluminium alloys are sample contamination, sample drift, beam damage, scan noise and etching of precipitates during sample preparation. Some examples of problems encountered during experiments are given in Figs. 3.9 and 3.10.

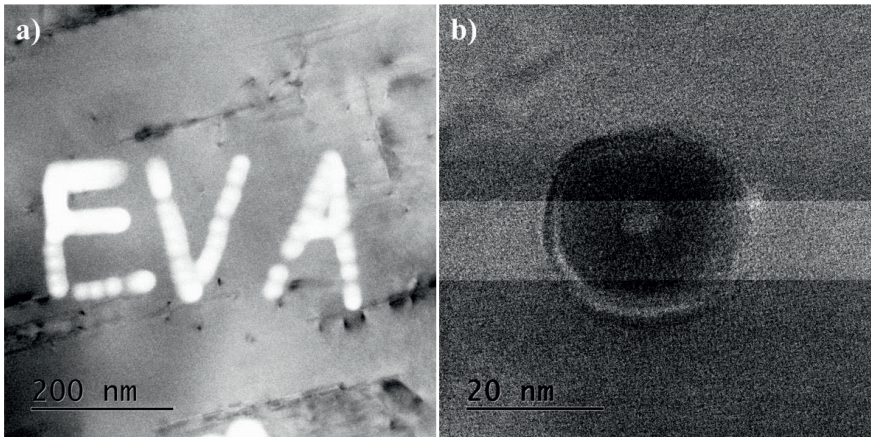

Figure 3.9 (a) Exceptional carbon contamination caused by the electron beam in STEM-mode at 200 kV. The image was taken after attempting x-ray energy dispersive spectroscopy of an aluminium alloy, **(b)** beam damage after using a too intense probe for lean aluminium alloys at 200 kV.

Contamination can be reduced by plasma cleaning the samples directly before inserting them into the microscope. A clean sample preparation procedure is vital, it is particularly important to use freshly made samples, as these have less hydrocarbons attached to the sample surface than old samples. Illuminating the sample at low magnification, with an intense probe also proved to be an efficient temporary solution, as the hydrocarbons get temporarily stationary on the sample surface.

Beam damage can occur if the probe is too intense, basically “burning” a hole into the material as in Fig. 3.9 (b). The sample and microscope should both be allowed to stabilize, preferably for some hours. If left alone for some time, the sample will cease to drift. Also, the probe correctors needs some time for stabilising after switching to STEM mode. Sample drift and scan noise is visualized in Fig. 3.10 (a) and (c) respectively. More detailed information on radiation damage and hydrocarbon contamination in TEM can be found elsewhere [60].

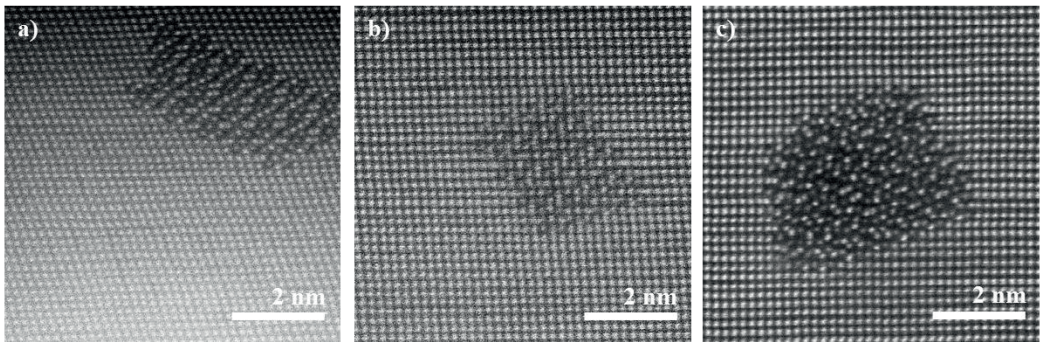

Figure 3.10 (a) A *β"* precipitate drifting towards the right. The higher intensity towards the end of the scan suggests contamination of hydrocarbons building up, **(b)** Al-matrix overlapping a precipitate and **(c)** almost perfect image, but scan-noise is present, making the Al-lattice appear "wavy" and giving the atomic columns abnormal shapes.

3.3 Electron Energy Loss Spectroscopy

Electron energy loss spectroscopy (EELS) is an important analytical tool in the TEM community, and it has proven to be relevant also when it comes to characterisation of aluminium alloys [61]. An illustration of the EELS setup is given in Fig. 3.11. Inelastically scattered electrons are directed into an energy loss spectrometer to measure the amount of energy lost after interacting with the sample. Spectroscopic data can be acquired point-by-point and often require significant post-acquisition processing. In this context, some specific EELS edges have been of interest, these are illustrated qualitatively in Fig. 3.12 with corresponding energy losses.

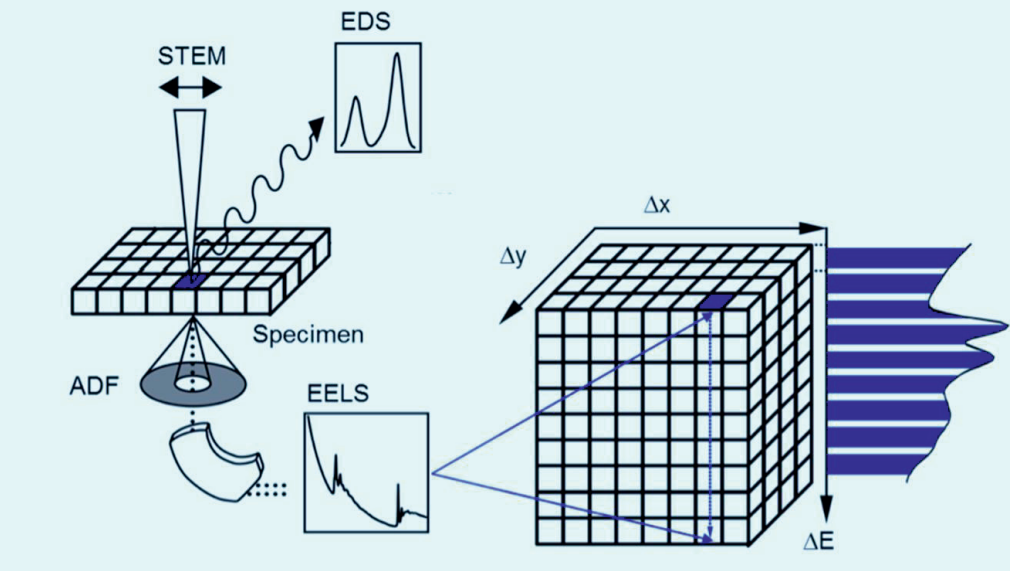

Figure 3.11 STEM - EELS schematic from Gatan [62].

The EEL spectrometer itself uses a magnetic field to deflect the electrons onto a detector. The electrons are subjected to a force, $\vec{F}$, according to Eq. 3.11.

$$\vec{F} = e(\vec{E} + \vec{v} \times \vec{B}) \tag{3.11}$$

Where e is the elemental charge, $\vec{E}$ is the electric field, $\vec{v}$ the velocity of the electrons and $\vec{B}$ is the magnetic field. Since low energy electrons are more deflected than high energy electrons, energy loss can be measured as differences in spatial positions on the detector.

It is mainly the coherency of the beam that affects the resolution of an EEL spectrum, although other temporal aberrations also contribute to a lower resolution. An energy loss spectrum is commonly divided into the low-loss and high-loss regime [63].

- Zero loss peak: is mostly due to un-scattered and elastically scattered electrons, but electrons losing only a small amount of energy also contributes to this peak. This peak will appear as the dominant peak in the spectrum for thin samples or materials with large mean free paths.
- The low-loss region in EELS is usually referred to as energy losses up to 50 eV. The dominant source of energy loss in this region is due to plasmons. Since plasmons are oscillations occurring for weakly bound electrons, these peaks will dominate the low loss region for light metals with free-electron structures. For aluminium the lowest energy-loss plasmon peak is at about 15 eV, and higher energy-loss peaks arise if the electrons excite multiple plasmons.
- High-loss is roughly said to start at energy losses above 50 eV. In this regime, the atoms become ionized as inner shell electrons are excited by the electron beam. The core-loss peaks are referred to as edges, and are element specific. The onset energy and appearance of an edge is dependent on the chemical environment in the vicinity of an atom, and is referred to as *fine structure*.
- The background is difficult to recognize if multiple scattering events occur, and other sources of noise or the detector itself might complicate things further. Usually, the background is modelled by assuming it follows an exponential or power-law decay.

EELS can be used to determine the thickness of a TEM sample. The model in this context assumes constant probability of electrons undergoing inelastic scattering events, as a function of distance covered through the sample material. The thickness, *t,* will according to this model be expressed as [64].

$$I_0 = I_{tot} e^{-\frac{t}{\lambda}} \qquad (3.12)$$

Where I_{tot} is the total lost intensity, I_0 is the zero-loss intensity and λ is the inelastic mean free path. The mean free path in Al alloys for an acceleration voltage of 150 keV can be approximated to 111 nm [64].

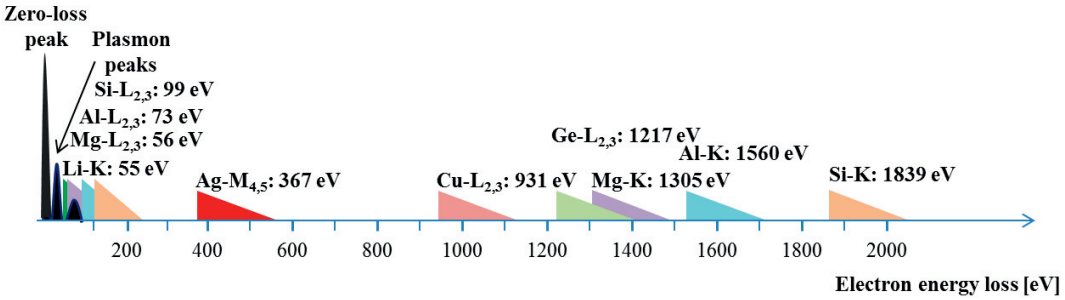

Figure 3.12 Relevant EELS edges in lean Al-Mg-Si alloys with increasing electron energy loss along the x-axis [65]. The edges are given the same shapes for simplicity.

If EELS is used in combination with STEM it is possible to acquire one EEL spectrum per pixel, enabling us to do atomically resolved EELS. This is done by data analysis of each EEL spectra, revealing the presence of one – or more elements at each projected scan position.

3.4 Techniques Employing the Photoelectric Effect

This section aims to explain the basics of the experimental techniques used for paper 7, which makes use of the photoelectric effect. Photoelectron spectroscopy (PES) is mainly used to distinguish the chemical composition and electronic structure of material surfaces. Electromagnetic radiation in the form of soft x-rays or UV light interacts with the electrons within the sample. If the electrons in the material become excited and gain energy above their binding energy and sample work function, they can be emitted into the vacuum. Once in the vacuum, the electrons are possible to analyse. The x-rays penetrate a long way into the sample, so when we talk about surface sensitivity in this context, this is due to how far into the material the electrons are able to escape from. Typically, the distance into the material where electrons can escape into the vacuum is about 3-4 λ, where λ is the inelastic mean free path of the electrons.

The interaction process can be simplified by a three-stage process [66]:

1. The electron is excited to a higher state after absorption of the incident photon energy.
2. The electron travels through the crystal to the surface-vacuum interface.
3. The electron is ejected into vacuum.

These are the three underlying stages of the photoemission process. The electrons, which are ejected into vacuum, can be detected by various methods. Usually hemispherical electron analysers are used, which depend on ultra-high vacuum (UHV) and disperses the kinetic energy of the emitted photoelectrons across a detector. An illustration of the photoemission

process and the energy alignment between sample and electron analyser is given in Fig. 3.13 [66].

Laboratory scale X-ray sources usually allow us to detect all elements with an atomic number of 3 and above. Because of the limitation in TEM related techniques to investigate Li-containing alloys, X-ray photoelectron spectroscopy (XPS) is a particularly well-suited alternative.

TEM related techniques like EELS does indeed detect Li, but the Li EEL edge unfortunately overlaps with that of Mg. PES related techniques has a great advantage to TEM when it comes to investigating the chemical composition of the material and doing in-situ work during heating.

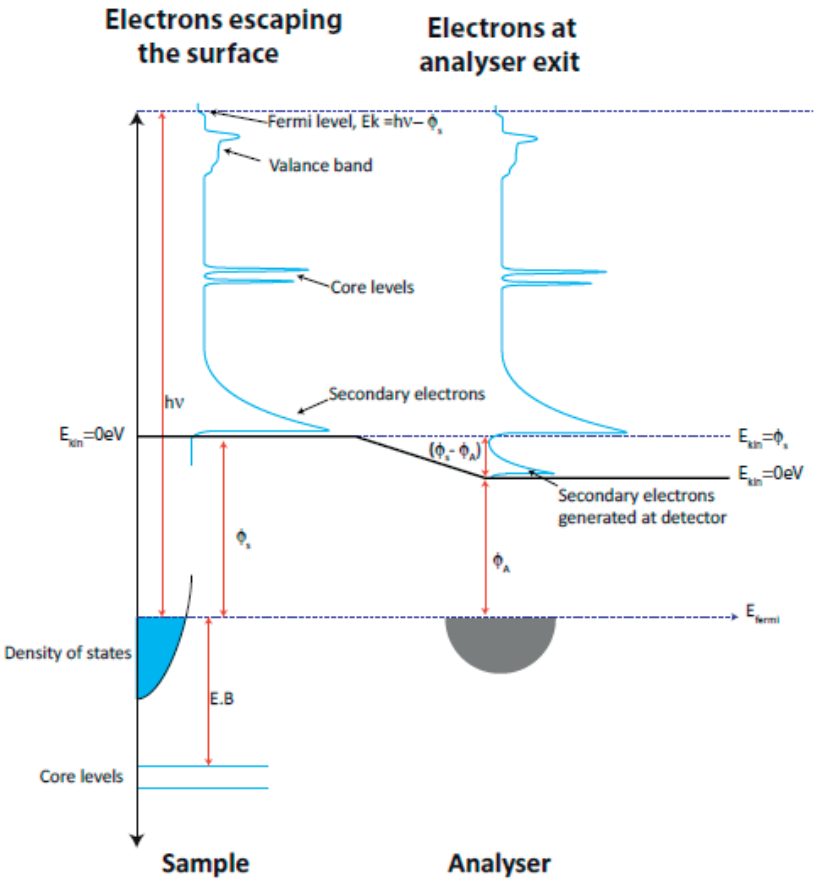

Figure 3.13 Illustrates the photoemission process and energy alignment between sample and electron analyser [66].

3.4.1 X-ray Photoelectron Spectroscopy (XPS)

XPS spectra can be obtained by irradiating materials with an X-ray beam while measuring the kinetic energy of electrons which have escaped the materials' surface. The electron binding energy, E_B, of each emitted electron can be determined from

$$E_B = hv - (E_K + \phi) \qquad (3.13)$$

Where hv is the photon energy, E_K is the kinetic energy of the electron, as measured by a detector, and ϕ is the work function of the detector.

The electronic structure of each element is unique, which allow us to directly identify which elements are present at the surface of the material. The binding energies produce specific sets of peaks, corresponding to the electron orbitals within the atoms, e.g. 1s, 2s, 2p, 3s, and so on.

3.4.2 SPELEEM

Spectroscopic photoemission and low energy electron microscope (SPELEEM) can be used alternately for XPEEM, low energy electron microscopy (LEEM), low energy electron diffraction (LEED), mirror electron microscopy (MEM) and other imaging modes [67]. A schematic of the SPELEEM set-up is given in Fig. 3.14.

XPEEM is a spectroscopic technique using X-rays as the primary illumination source. This method allows or the chemical state of the elements present on a material surface to be imaged with a lateral resolution approximately 20 nm. The emitted photoelectrons are possible to image by combining advanced electrostatic

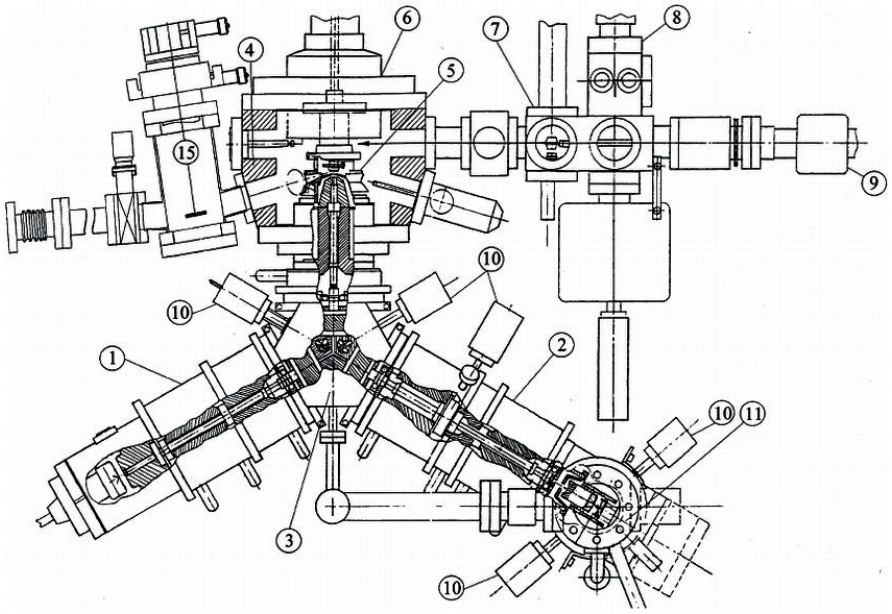

Fig. 3.14 Schematic of the spectroscopic photoemission and low energy electron microscope (SPELEEM): (1) electron gun, (2) image column, (3) magnetic beam separator, (4) specimen chamber, (5) magnetic objective lens, (6) sample manipulator, (7) preparation chamber, (8) air lock, (9) transfer rod, (10) illumination, selected area (SA) and contrast aperture, as well as energy slits, (11) analyzer, (15) soft X-ray refocussing mirror. Figure and figure text from Schmidt et al. [67].

This technique can give us information about surface properties like elemental composition, chemical bonding, electronic band structure, work function and crystallinity. An example of core level mapping is given in Fig. 3.15, showing how Mg goes to grain boundaries during heating. Core level spectra showing peaks which can be used for mapping is given in Fig. 3.16.

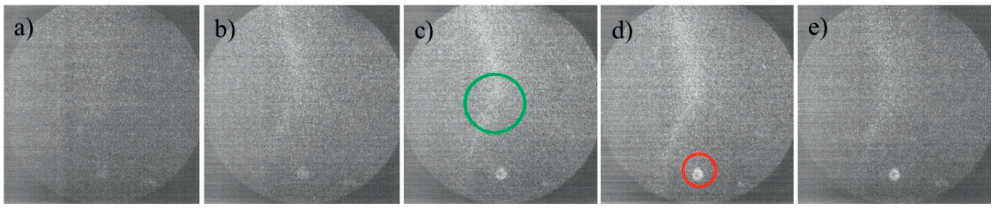

Figure 3.15 XPEEM images of an Al-Mg-Si-Cu alloy surface, showing the Mg 2p core level with increasing temperature. The areas in (a)-(e) are directly comparable to the image given in Fig. 3.16 (d). **(c)** The triple junction easily seen in Fig. 3.16 (d) is indicated by a green circle. **(d)** The red circle indicates a feature on the sample surface with increasing Mg content as a function of time and heating temperature.

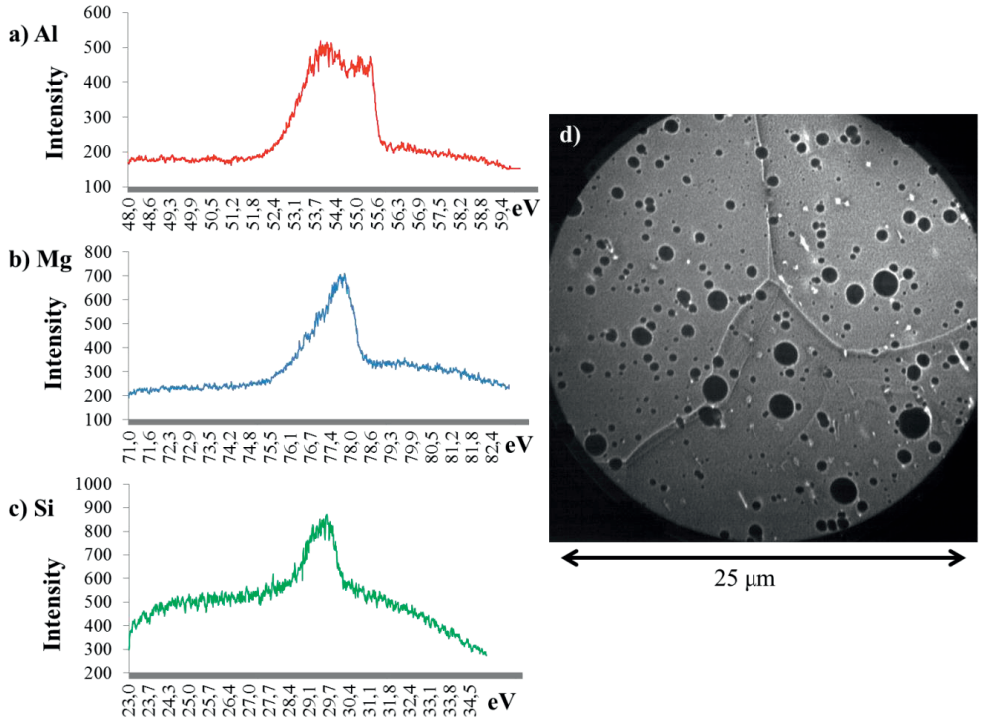

Fig. 3.16 Emitted photoelectron intensity core level maps of **(a)** Al 2p core level, **(b)** Mg 2p core level and **(c)** Si 2p core level. **(d)** A MEM image of the mapped region, the triple-junction where three grains meet is clearly visible in the middle of the image. The measurements were done on an Al-Mg-Si-Cu alloy after SHT at elevated temperature.

Chapter 4

Other Experimental Techniques

When it comes to aluminium alloys, one of their most important properties is mechanical strength. The most common and robust methods for determining strength are 'hardness indentation' and tensile testing. A brief explanation of TEM sample preparation will also be given in this chapter. Subsequently, the procedure of microstructure quantification by TEM and EELS will be explained, and finally an introduction to DFT and how it has been applied in this work will be given.

4.1 Hardness Measurements

Vickers hardness (HV) is a hardness indentation method where the indenter has the shape of a diamond shaped, square-based pyramid. Usually, the angle α between the opposite faces at the vertex of the pyramidal indenter is 136°. Vickers hardness can then be expressed as in Eq. 4.1 [68].

$$HV = \frac{F}{A} = \frac{2sin\frac{\alpha}{2}}{d^2} \tag{4.1}$$

F denotes the applied force on the indenter (usually 1 kg for aluminium alloys and 5 kg for steels), *A* is the surface area of the indentation and *d* is the average diagonal of the indentation. An illustration of the indentation method and the pyramidal indenter is given in Fig. 4.1.

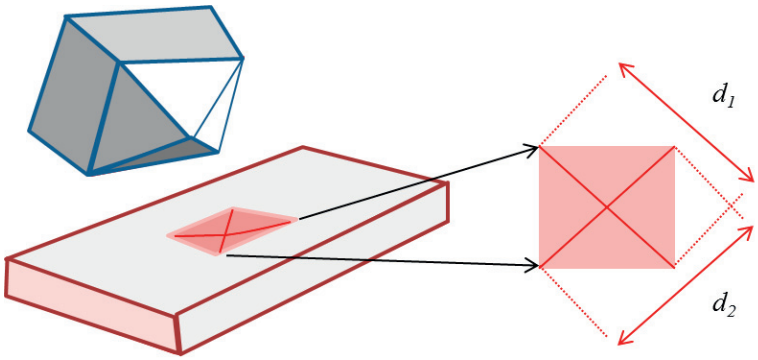

Figure 4.1 Vickers hardness indentation method. The average diagonal from d_1 and d_2 is used for hardness calculations. If the material is homogeneous, the two diagonal lengths will be equal.

To improve contrast of the indentations, prior to every set of HV measurements, samples were polished with SiC paper up to a fineness of 2500 #/cm^2. The hardness for each condition is given as an average of 10 indentations, the set consisting of five indentations from each side of the sample.

4.2 Tensile Strength

Tensile testing is often used to investigate the strength and ductility of metals and alloys. Tensile tests are usually presented as stress-strain diagrams, which can be divided into different regions depending on the mechanisms occurring in the material [6]. In the elastic region, where low stress is applied, the material will recover to its undeformed state. When the yield point is reached, plastic deformation becomes the dominating process, meaning that the deformation is not recoverable upon the release of the applied stress. The yield point, marked by 1 in Fig. 4.2, and elastic limit are difficult to separate, and are usually referred to as approximately equal.

For low stress, the stress-strain relationship is approximately linear and can be assumed to follow Hookes' law [6] (p. 55). However, the plastic deformation behaviour can be further divided into three parts succeeding the yield point: yielding, strain hardening and necking.

When the material is strained further after reaching the yield point, one might observe a plateau, often referred to as the 'yield point elongation'. This plateau occurs due to a diffusion related phenomenon, where dislocations break away from their interstitial pinning atoms and become re-pinned with a negligible increase in stress.

Moving further along increasing strain in the stress-strain diagram, the yield strength increases. By deforming the material, the density of dislocations in the material increases.

When the dislocation density increases, the stress needed to make dislocations move also increases, resulting in higher yield strength.

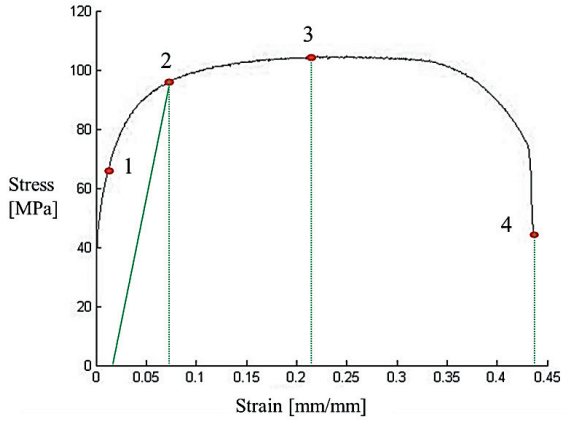

Figure 4.2 Typical stress-strain curve of an Al-Mg-Si alloy. 1: example yield point, 2: the offset yield point when a yield point is not easy to define [6], 3: ultimate strength and 4: fracture. The region between 2 and 3 is denoted the elongation region, while the region between 3 and 4 is the necking region. The green line terminating in 2 indicates the slope following Hooke's law when starting at 0.02 strain.

The ultimate strength, marked by 3 in Fig. 4.2, refers to the maximum strength required to fracture the material in two bits, this is indicated by the number 3 in Fig. 4.2. The final part of typical stress-strain curves is the 'necking region', where the tensile samples simply start to 'neck' and finally ruptures. The rupture is marked by 4 in Fig. 4.2.

4.3 TEM Sample Preparation

To study the nanosized precipitate needles with TEM it is necessary to prepare ultrathin samples where at least one spatial direction is thinner than ≈100 nm. TEM samples can in principle be taken from anywhere within the bulk material and from any time during the heat treatment. For extruded rods it is however common to avoid areas close to the surfaces because of surface effects.

Slices with surface normals parallel to the extrusion direction are cut and polished to a foil with thickness of about 100 μm. Small disks of about 3 mm diameter are then stamped out from the foil and electropolished. Polishing the samples with electrolyte ensures that only the centres of the disks are thinned and eventually creates holes. If the area around the hole through the sample is electron transparent, it can be studied by TEM.

All TEM specimens in this work have been electropolished to obtain electron transparent areas. A twin-jet Tenu-Pol 5 from Struers was used, with an electrolyte consisting of $\frac{1}{3}$ nitric acid and $\frac{2}{3}$ methanol. The electrolyte had to be cooled to about -25 °C with liquid nitrogen throughout the process. The optimal voltage used for aluminium alloys is usually 20 V, but can vary.

Before inserting the samples in the TEM, they were decontaminated in a Fischione plasma cleaner, model 1020, for 3-7 minutes in O_2/Ar plasma.

4.4 Instruments

A Philips CM30 TEM operated at 150 kV was used for precipitate statistics in combination with a parallel electron energy loss spectrometer (PEELS) for thickness measurements. The PEELS was a model 601 from Gatan. The most important results from these measurements are presented in Paper 1, 2, 5 and 6.

The HAADF-STEM images and the STEM-EEL spectra in this work were acquired in a spherical aberration corrected (both probe and image) JEOL ARM200F, equipped with a cold FEG. The operation voltage was 200 kV, the probe size 0.08 nm and the inner collector angle 50 mrad. All precipitates were imaged along one of the <100>Al directions along the needle/lath extension, normal to the cross-section. The microscope was operated at 80 kV for strain mapping and 200 kV for atomic resolution imaging and EELS.

4.5 Quantification of Microstructure from TEM and EELS

The nanosized precipitate needles in aluminium alloys are the main contributors to the age hardening effect. Consequently, they should be studied both as single precipitates and as precipitate distributions.

In this study high purity alloys have been investigated, all with an Al base metal with a purity level of 99.9 wt %. For precipitation kinetics it is useful to know how much of the solute is available for precipitation. Si is easily consumed by iron-rich phases that are present in 6xxx alloys. The effective solute of Si is thus assumed to be one quarter of the wt % of iron [69].

For quantification of the precipitate microstructure, bright field TEM images were acquired in a Philips CM30 operating at 150 kV. Since knock-on damage occurs at about 170 kV, the operation voltage should be either well below or above this value. Since the needles grow along the three <001> Al directions the least complicated visualisation is along one of these. It is beneficial to slightly tilt the sample away from the <001> Al axis, this makes the needles appear darker than the matrix due to diffraction contrast.

The corresponding thicknesses of each imaged area were obtained from EELS measurements. The imaged areas for statistics were not taken in the vicinity of grain boundaries, large particles or other features that may cause irregularities in the precipitate distribution.

Three parameters are of particular interest when it comes to quantifying the precipitate microstructure: cross section, length, number density and, based on these three, the volume fraction. Experience has shown that precipitate number densities vary little between grains in alloys with identical composition and heat treatment history. To obtain sufficient data for precipitate statistics from each condition, a minimum of 1000 needles were counted to estimate number density, 500 needle lengths were measured and 50 cross sections were calculated. Several grains were inspected from each condition to make sure the statistics were based on representative areas.

The precipitate number density, ρ, for an imaged area can be expressed by the number of counted precipitates, N, the imaged area , A, and its thickness, t.

$$\rho = \frac{3N}{At} \tag{4.2}$$

It is assumed that the number density of precipitates is the same in all three <001> Al directions. Only precipitates growing along the viewing direction are counted, resulting in the factor 3 in Eq. 4.3. Since the needle length is significant as compared to the thickness of the imaged area, a correction of the lengths needs to be applied. Several measured needle lengths "belong to a thicker area" as they have been cut during sample preparation, the effective thickness should therefore be extended to $(t + \lambda)$, where λ is the average needle length.

$$\rho = \frac{3N}{A(t + \lambda)} \tag{4.3}$$

The average needle length can be found from the expression

$$\lambda = \frac{l_m}{1 - \frac{l_m}{t}\cos\theta \tan\phi} \tag{4.4}$$

Where l_m is the measured needle length, θ is the angle between the precipitate needles lying perpendicular to the incident electron beam and the specimen surface. θ is difficult to measure accurately, which is why an estimate of 45° is used. The tilt angle in the microscope

is denoted ϕ here. The full methodology has been developed elsewhere, and can be read in detail in [30]. This work is tedious, and a semi-automated MATLAB script has been used for statistical analysis. The precipitates still have to be marked by hand by using this script, but saves time as compared to a completely manual approach.

4.6 Density Functional Theory (DFT)

DFT is based on the standard theory behind quantum mechanical systems and is particularly helpful for simulating electronic properties of atoms, molecules and condensed phases. In this context, DFT has been applied to simulate the solute bonding energies and volume misfits in aluminium.

DFT is mainly used in order to determine three-dimensional electron wave functions in a many-body system, and we have here assumed the two theorems of Hohenberg-Kohn. These theorems state that, firstly, for a system in its ground state the electron density can be used to determine the external potentials acting on the electrons [70] [71]. Secondly, a function of the electron density can be determined for any external potential. Based on the Hohenberg-Kohn theorems, it should be possible to calculate the electronic properties [70]:

$$\left[-\frac{\hbar^2}{2\mathrm{m}}\nabla^2 + \mathrm{v}_{\mathrm{effective}}(\vec{\mathrm{r}})\right]\phi_{\mathrm{i}} = \epsilon_{\mathrm{i}}\phi_{\mathrm{i}}(\vec{\mathrm{r}}) \tag{4.5}$$

Where $\hbar$ is the Planck constant divided by 2π, the effective potential at position $(\vec{\mathrm{r}})$ is $\mathrm{v}_{\mathrm{effective}}$, the orbital energy is ϵ_{i} and the Kohn-Sham orbital is $\phi_{\mathrm{i}}(\vec{\mathrm{r}})$. Further on, the electron density, $\rho(\vec{\mathrm{r}})$, of an N-body system can be expressed as:

$$\rho(\vec{r}) = \sum_{i}^{N} |\phi_i(\vec{r})|^2 \tag{4.6}$$

And $\mathrm{v}_{\mathrm{effective}}(\vec{\mathrm{r}})$ is a function of the electron density, the external potential due to the nuclei, $\mathrm{v}_{\mathrm{external}}(\vec{\mathrm{r}})$ and the exchange-correlation potential $\mathrm{v}_{\mathrm{ex-corr}}(\vec{\mathrm{r}})$.

$$v_{effective}(\vec{r}) = v_{external}(\vec{r}) + e^2 \int \frac{\rho(\vec{r}')}{r - r'} d\vec{r'} + v_{ex-corr}(\vec{r}) \tag{4.7}$$

Finally, the total energy of the system, $E[\rho]$, can be expressed as a function of the electron density:

$$E[\rho] = T_s[\rho] + \int v_{external}(\vec{r})\rho(\vec{r})d\vec{r} + V_H + E_{ex-corr}[\rho] \tag{4.8}$$

Where T_s is the kinetic energy, V_H is the Coulomb potential and $E_{ex-corr}$ is the exchange-correlation energy.

4.6.1 Interaction Energies

DFT was applied to find bonding energies between different solute elements and/or vacancies. The lattice parameter used for the calculations is based on the relaxation of an aluminium supercell consisting of 5x5x5 aluminium unit cells. The unit cell relaxed to 20.20474 Å, i.e. a = 4.04095Å. The interaction energies are estimated from the difference between total energies. All calculations have the same cell size and parameter settings so that any systematic errors should cancel out. The bonding energies between two elements are calculated from the 1st to 8th nearest neighbour positions. The uncertainty is quite high in the binding energy calculations, between 5 – 10 %, since the total energies of the systems that are subtracted is about -1865 eV. It should be noted that the computed energy differences are quite small and the diffusivity consists of several components.

The Vienna ab initio simulation package (VASP) [72] [73] was used to execute the DFT calculations in this work [70] [71], using the projector augmented wave method (PAW) within the PBE (Perdew-Burke-Ernzerhof) generalized gradient approximation. For accurate energies, a separate calculation was performed using the tetrahedron method with Blöchl correction for the smearing.

Bonding/interaction energies were calculated based on Eqs. 4.9 and 4.10.

$$E_Y = E_{Al499_Y} - \frac{499}{500}E_{Al500} \tag{4.9}$$

$$E_{YZ} = E_{Al498\_YZ} - \frac{498}{500}E_{Al500} - E_Y - E_Z \tag{4.10}$$

The calculations were based on a cell consisting of 500 Al atoms, Y and Z represents an atom or a vacancy replacing one of the Al atoms in the cell. E_Y and E_Z are the solid solution energies of atom Y and Z respectively. The interaction energy between the two elements Y and Z in the Al cell is calculated by subtracting the solid solution energies of each element from the total electronic energy of the cell. A more detailed explanation of how to calculate formation energies of structures and solid solution energies of atoms are explained in [74].

4.6.2 Misfit Volumes

In order to obtain consistent results for misfit volumes, Δv_m, it is not enough to calculate them directly from a DFT volume relaxation of single solute atoms incorporated in perfect aluminium crystals. Here, the more complex method is used, with 27- and 64-atom supercells [75]. The pressure depending on concentration of solute is calculated from 1-3 solute atoms present in the supercells. It has been found that the dependence of pressure on solute concentration is approximately linear [76], from this, misfit volumes can be calculated using the slope of the curve and a DFT-computed bulk modulus, *B* of pure aluminium.

$$\Delta v_m = \left(\frac{\partial \Delta v_m}{\partial c}\right) c_{1sol} = \left(\frac{1}{B}\frac{\partial p}{\partial c}\right) c_{1sol} \tag{4.11}$$

Where c_{1sol} is the concentration of one solute in the aluminium supercell. The misfit volumes are taken as an average from the separate values based on each supercell. Some example plots of pressure as a function of concentration is given in Fig. 4.3, with corresponding misfit volumes based on the above equations.

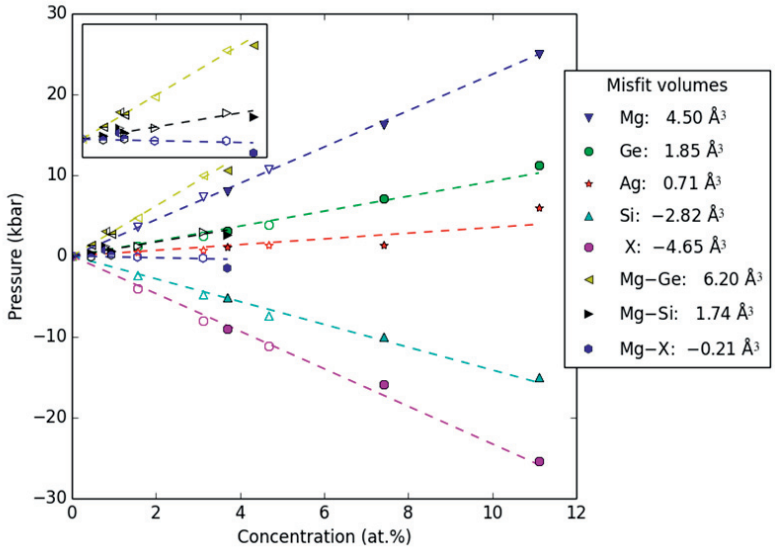

Figure 4.3 Misfit volumes of the alloying elements and vacancies (X) in fcc aluminium. For single elements in Al: the open symbols indicate calculations based on 3x3x3 primitive cells (27 atoms) and the filled symbols indicate calculations based on 4x4x4 primitive cells (64 atoms). For pairs of elements in Al (insert): open symbols indicate calculations based on 1 pair in 3x3x3, 4x4x4, 5x5x5 and 6x6x6 primitive cells and filled symbols indicate 2 pairs in 4x4x4 and 6x6x6 primitive cells. Dashed lines show linear fits to the data for each element or pair. See [24] for more information.

Part II

Papers

Paper 1

Effects of Germanium, Copper, and Silver Substitutions on Hardness and Microstructure in Lean Al-Mg-Si Alloys

Metallurgical and Materials Transactions A, 46A (2015) 4369 – 4379

Is not included due to copyright

Paper 2

TEM and HAADF-STEM Investigations on the Effect of Cu and Ge Additions on Precipitation in 6xxx Al Alloys

Microscopy and Analysis January (2016) 14 - 16

TEM and HAADF-STEM investigations on the effect of Cu and Ge additions on precipitation in 6xxx Al alloys

E A Mørtsell[1], C D Marioara[2], S J Andersen[2], J Røyset[3], O Reiso[3] and R Holmestad[1]

1 Department of Physics, NTNU, 7491 Trondheim, Norway, 2 SINTEF Materials and Chemistry, N-7465 Trondheim, Norway 3Hydro Aluminium R&D Sunndal, N-6600 Sunndalsøra, Norway

INTRODUCTION

The demand for environmental friendly, light alloys is higher than ever, and aluminium alloys have been deemed imperative in this context. In particular, the age-hardenable Al 6xxx series are used for large scale trades like car manufacturing and the packaging industry.

These alloys have Mg and Si additions to procure the metastable hardening phases which grow during heat treatment and are the main cause of strength in these alloys. The metastable strengthening phases are shaped as needles and grow along the three Al <100> lattice directions. As the alloy is heated, several precipitate phases form, depending on the duration of the heat treatment, temperature and the composition of the alloy[1]. The needles consist of the added alloying elements in addition to aluminium itself. The precipitation sequence is given as[2-4]:

Supersaturated solid solution → atomic clusters → Guinier Preston-zones (pre-β″) → β″ → β′, U1, U2, B′ → β, Si (stable phases)

One of the major industrial challenges is how to increase extrusion speed while maintaining the alloy strength. While aluminium with no added solute would provide the maximum extrusion speed, this material would also be the weakest.

The main idea behind this work was consequently to lower the amount of added solute in atomic percentage (at %) from a common industrial 6060 Al alloy, while maintaining the initial strength. This was attempted by lowering the added amount of Mg and Si and adding back a lower at % of copper and germanium. These two elements were chosen because of their known effect on precipitation[5,6].

The precipitate structures need to be characterized down to the atomic level to clarify if the added elements contribute to the strengthening phases.

For this purpose, aberration-corrected high angle annular dark field scanning transmission electron microscopy (HAADF-STEM) has several advantages. HAADF-STEM can provide very high spatial resolution, it is less affected by objective lens defocus and specimen thickness than conventional high resolution transmission electron microscopy (HR TEM) and it exhibits atomic number contrast (Z - contrast) where heavier atomic columns appear brighter[7,8]. This technique is well suited for locating the Cu and Ge in these alloys because of the high Z-contrast in the HAADF-STEM images, Cu (Z = 29) and Ge (Z = 32) containing atomic columns will provide a relatively high intensity compared to Mg, Al and Si atomic columns. Actual atomic column positions correspond directly to intensity peaks in the HAADF-STEM images.

MATERIALS AND METHODS

MATERIAL AND SAMPLE PREPARATION

Three alloys have been used for this study; the dense reference is denoted A0 and falls within the specification limits of the industrially common AA6060 alloy. The alloy with reduced Mg and Si content and back-added Cu and Ge additions is denoted ACG. Finally the lean reference alloy with reduced Mg and Si additions but no Cu or Ge is denoted A1. All three alloys have normal levels of Fe and Mn (less than 0.1 at %), which do not contribute to the precipitate structures.

The alloys were cast as cylindrical billets and extruded as 2 cm diameter round profiles. Samples were cut perpendicular to the extrusion direction and solution heat treated at 530 °C for 5 minutes in a salt bath. The samples were held at room temperature for 4 hours before being heated gradually to a final temperature of 195 °C in an air circulating furnace. The samples were then held at this final artificial ageing temperature for 4 hours, when they were close to peak hardness. Finally the samples were water quenched to room temperature. A full description of the casting, homogenization, extrusion and a complete heat treatment is given in[9].

The sample blocks were sliced perpendicular to the extrusion direction and polished into foils of approximately 100 µm thickness. Disks of 3 mm were stamped out from the foils and electropolished using an electrolyte consisting of one third nitric acid and two thirds methanol. Liquid nitrogen was added to the solution to keep it at -25 °C. The TEM specimens were plasma cleaned for 7 minutes immediately before inserting them into the TEM.

TEM AND HAADF–STEM

The TEM bright field images presented and used for statistics in this work were taken by a Philips CM30 TEM operated at 150 kV and equipped with a Gatan PEELS system. The HAADF-STEM images were recorded with a spherical aberration (Cs), double corrected JEOL ARM200F, operated at 200 kV. The probe size was 0.08 nm and the inner collection angle 50 mrad.

RESULTS

TEM AND HAADF–STEM

The precipitate microstructure was quantified with respect to the precipitate

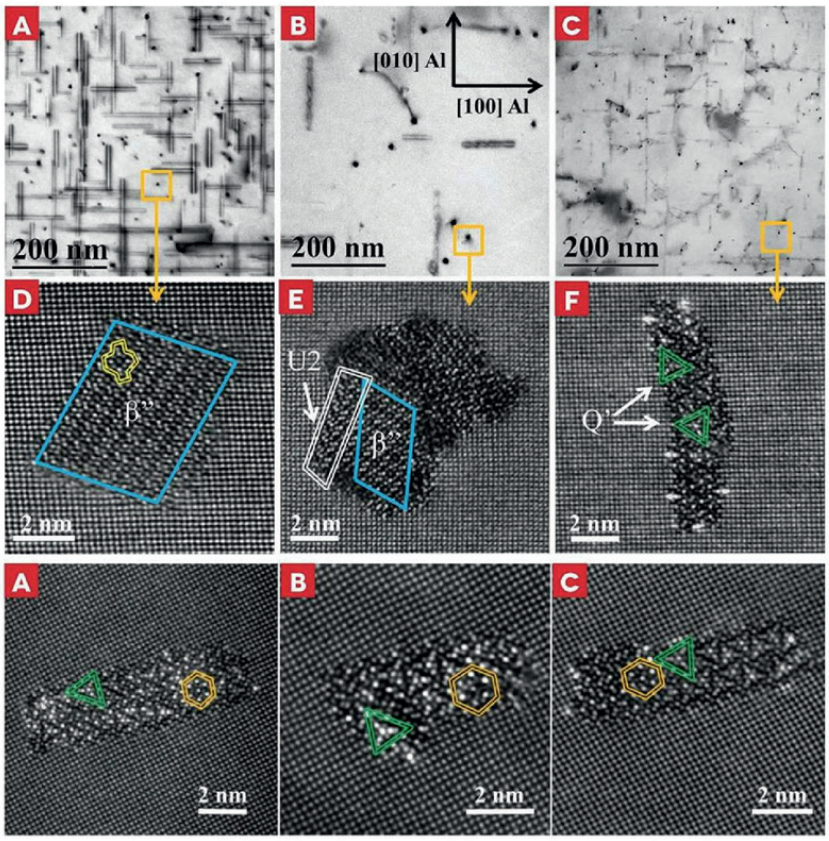

FIGURE 1, top. a) - c) TEM images illustrating precipitate microstructure in A0, A1 and ACG respectively. d) – f) HAADF STEM images of precipitate cross sections from A0, A1 and ACG respectively. An "eye" in the β'' phase is indicated in (d) with double yellow lines. (e) is based on Fig. 1 (c) in Mørtsel *et al*[10]

FIGURE 2, above. Three precipitates from the alloy ACG, containing Cu and Ge in addition to Mg and Si. The hexagonal Si/Ge-network network of high intensity columns is easily detectable and indicated by orange double line hexagons. The triangular local Cu symmetry, common in Q'/C phases is indicated by double green lines

needle cross sections, lengths, number densities and volume fractions. The full statistical procedure is explained in[1]. The microstructural differences between the three alloys could easily be detected by eye when comparing the TEM images in Fig. 1 (a) - (c). The dense reference A0 has needles of about 100 nm length, Fig. 1 (a), which were found to be mainly of β" type[9]. The lean reference A1 shows a very different microstructure, where the needles are very few and large compared to A0, see Fig. 1 (b). The precipitate needles in the Cu and Ge added alloy ACG are remarkably smaller than in the two other alloys and have a much higher number density as can be seen from Fig. 1 (c). The images in Fig. 1 (a) - (c) are taken at similar thicknesses and are directly comparable.

When looking at the microstructure of the three alloys at higher resolution it becomes clear that it is not only the sizes and number densities that differ between the needles. Atomic details in individual precipitates become detectable as we turn to HAADF-STEM as a characterization technique. Three typical precipitate cross sections from each alloy are given in Fig. 1 (d) - (f). Each bright spot in the images corresponds to an atomic column normal to the image plane.

In the commercial alloy A0 a majority of the precipitates are of the β" type, the phase associated with peak hardness of the 6xxx alloys [2, 3]. A precipitate consisting mainly of β" is shown in Fig. 1 (d), the so called β" "eyes" can easily be recognised in the cross section. Disordered precipitates with no repeating unit cells are also found in this alloy, although they are not appearing frequently and they always contain elements of the β" phase in their structures.

The lean alloy A1 has by far the largest precipitate needles and the number density is about 50 times smaller than that of ACG. When looking closer at the precipitate cross sections, as the example in Fig. 1 (e), most of them seem to be combinations of β', U2 and disordered regions. However, also β" areas appear frequently as fragments of the cross sections.

The Cu and Ge added alloy exhibited a completely different structuring of needle cross sections, see an example in Fig. 1 (f) and Fig. 2. The precipitates in ACG consist of combinations of regions belonging to different precipitate phases where the most frequently appearing phase is the Cu-containing Q' phase[6]. In addition, a hexagonal network of high intensity columns, associated with the presence of the Si/Ge-network[5], appears in almost all precipitate models.

DISCUSSION

Both Cu and Ge were present in all observed cross sections in ACG, which brings about the explanation that the two elements are active during the nucleation process of the precipitates. This idea is supported by precipitate statistics[9], where the same amount of solute as in A1 creates 50 times more precipitates of smaller cross sections and shorter lengths in ACG. Cu and Ge seem to cause more precipitate needles to nucleate with good structural stability during the following ageing treatment.

The disordered regions of the precipitates in Figs. 2 and 3 exhibit a hexagonal order of high intensity columns. These columns have a projected distance of ≈ 0.4 nm affirming that they are occupied by silicon. This is commonly known as the hexagonal Si-network, which is confirmed to appear in disordered precipitates[4,5]. The Z-contrast is very high in most areas where the hexagonal network is observed, confirming that Ge must replace or partly occupy Si network columns [5].

From the precipitate cross section in Fig. 3 the columns forming 'eye'-like units/molecules in β" can easily be observed, these are indicated with yellow double lines. The yellow lines point out symmetry in the cross section; from their centres and outwards can be seen similar structure elements unfolding at opposite heights. Several yellow lines indicate the cross-section has an inversion centre, which could be the location where a smaller cluster nucleated the precipitate. For instance, the β" eyes can all be found at opposite heights on each side of the inversion centre. The centre of the precipitate is disordered; still the hexagonal Si-network is present across this area as indicated by the red solid lines.

Recent publications have shown that Ge has the highest vacancy binding energy as compared to the other alloying elements in this work[11]. The relatively high solute-vacancy binding energy causes Ge to be surrounded by vacancies, more so than the other alloying elements. Somehow this stabilizes more of the clusters. Also Ge addition seems to limit formation of dislocation loops, thereby reducing heterogeneous nucleation and slowing kinetics. Ge is larger than the chemically similar Si, which corresponds well with the findings that vacancy bonding energy increases with size[12].

A higher number density of small needles seems to be a general rule when it comes to the increase of strength in aluminium 6xxx alloys. Thus,

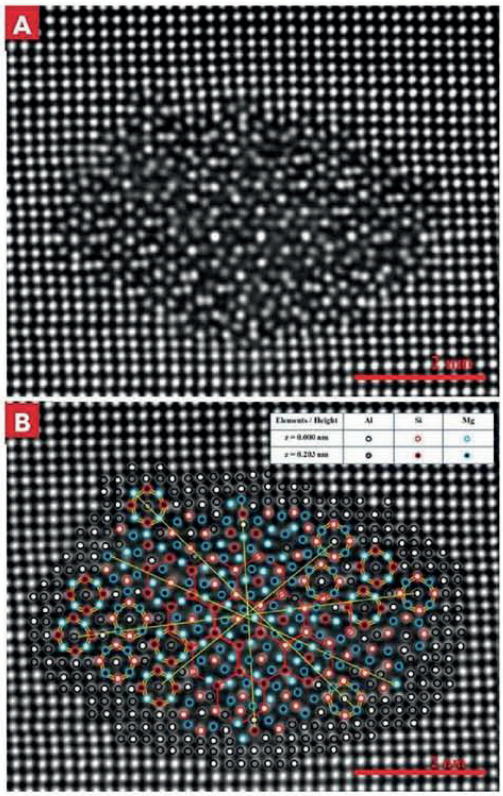

FIGURE 3
HAADF-STEM image of a precipitate needle cross section from A0. a) Original image and b) image with atomic overlay based on Z-contrast and precipitate models. The red lines indicate the hexagonal Si-network which is located in the central disordered part of the precipitate. The yellow lines indicate inversion points in the precipitate and the inversion centre should be located at the crossing of the yellow lines. β'' eyes are indicated by double yellow lines

when Ge creates a high precipitate number density of more disordered precipitates, this should lead to higher hardness values, which is exactly what experiments show.

SUMMARY AND CONCLUSIONS

The total amount of solute can be reduced in a common 6xxx aluminium alloy while maintaining the initial hardness. By replacing a fraction of the Mg and Si atoms with a lower fraction of Cu and Ge atoms, the precipitate microstructure is refined and the low amount of solute allows the extrusion speed of the alloy to be increased.

Both Cu and Ge were present in all observed precipitate cross sections and are believed to be important during the nucleation process, where their ability to bind to vacancies have been suggested as a significant cause. The Cu-Ge added alloy exhibits disordered precipitates, consisting of combinations of different phases. The hexagonal Ge/Si-network was identified in all observed precipitate cross sections.

REFERENCES

1 Marioara C D, Andersen S J, Zandbergen H W, Holmestad R 2005 *Metall. Mat. Trans. A*, 36, pp. 691 - 702.
2 Marioara C D, Nordmark H, Andersen S J, Holmestad R 2006 *J. Mater. Sci.* 41, pp 471 - 478
3 Edwards G A, Stiller K, Dunlop G L, Couper M J 1998 *Acta Mater.* 46, pp 3893 - 3904.
4 Marioara C D, Andersen S J, Jansen J, Zandbergen H W 2001 *Acta Mater.* 49, pp. 321-328.
5 Bjørge R, Marioara C D, Etheridge J 2013 *Imaging and Microscopy*, 4, pp. 36.
6 Saito T, Marioara C D, Andersen S J, Lefebvre W, Holmestad R 2014 *Phil. Mag.* 94, issue 5, pp. 520-531.
7 Nellist P D, Pennycook S J 2000 Elsevier 113, pp. 147 - 203.
8 Yamazaki T, Kawasaki M, Watanabe K, Hashimoto I, Shiojiri M 2002 *Ultramicroscopy* 92 pp. 181 - 189.
9 Mørtsell E A, Marioara C D, Andersen S J, Reiso O, Røyset J, Holmestad R 2015 *Met. Trans. A* 46, issue 9, pp. 4369 - 4379.
10 Mørtsell E A, Marioara C D, Andersen S J, Røyset J, Holmestad R 2015 *J. Phys.: Conf. Ser.* 644, 012028.
11 Wolverton C 2007 *Acta Mater.* 55, pp. 5867 - 5872.
12 Leyson G P M, Hector L G, Curtin W A 2012 *Acta Mat.* 60, pp. 3873 - 3884.

BIOGRAPHY

Eva A. Mørtsell finished her MSc at the Norwegian university of science and technology (NTNU) in 2012. She then started her 4 year PhD in Physics at NTNU with main supervisor Professor Randi Holmestad. Her work evolves around lean aluminium alloys, including hardness and tensile strength and characterization of precipitate needles at the atomic scale. The main characterization techniques are TEM, HAADF-STEM and EELS.

Randi Holmestad is a professor at the department of physics at NTNU (since 99). She is also an advisor for SINTEF Materials and Chemistry. Degrees: Dr. ing. (PhD) in materials physics, NTH, 1994, Siv. ing (MSc) in technical physics, NTH, 1991. Holmestads' present research interests are focussed on materials physics; transmission electron diffraction and microscopy (TEM), materials microstructure and the relation to macroscopic properties. She has initiated and been project leader for several externally funded projects over the past fifteen years, funded mainly by the Norwegian Research Council and Hydro Aluminium.

ABSTRACT

The strength loss that occurs in lean Al-Mg-Si alloys because of the reduction of Mg and Si can be compensated by adding back a lower fraction Cu and Ge atoms. The main hardening mechanism in Al-Mg-Si alloys is the formation and growth of nanosized precipitates shaped as needles. Material hardness has been correlated to precipitate parameters quantified by TEM. It is clear from the results that adding Ge and Cu strongly enhances the precipitate number density while reducing the precipitate sizes. HAADF-STEM confirms that both Cu and Ge enter the precipitate structures, without exceptions. Ge is believed to increase the number density of needles because of its strong interaction to vacancies in the Al matrix.

ACKNOWLEDGEMENTS

This work has been supported through the BIA RolEx project, no. 219371 by Hydro Aluminium and the Research Council of Norway. The contributors are greatly acknowledged for their support. Also thanks to the NORTEM project.

CORRESPONDING AUTHOR DETAILS

Eva Anne Mørtsell, Department of Physics, NTNU, 7491 Trondheim, Norway
E-mail address: eva.mortsell@ntnu.no

Microscopy and Analysis 30(1): 14-16 (EU), January 2016

Elemental Electron Energy Loss Mapping of a Precipitate in a Multi-Component Aluminium Alloy

Micron 86 (2016) 22 - 29

Paper 3

Micron 86 (2016) 22–29

Contents lists available at ScienceDirect

Micron

journal homepage: www.elsevier.com/locate/micron

Elemental electron energy loss mapping of a precipitate in a multi-component aluminium alloy

Eva A. Mørtsell[a,*], Sigurd Wenner[a], Paolo Longo[b], Sigmund J. Andersen[c], Calin D. Marioara[c], Randi Holmestad[a]

[a] Department of Physics, Norwegian University of Science and Technology (NTNU), 7491 Trondheim, Norway
[b] Gatan Inc., 5794 W Las Positas Blvd, Pleasanton, CA 94588, USA
[c] SINTEF Materials and Chemistry, N-7465 Trondheim, Norway

ARTICLE INFO

Article history:
Received 16 February 2016
Received in revised form 22 March 2016
Accepted 22 March 2016
Available online 13 April 2016

Keywords:
Al-Mg-Si alloy;
HAADF-STEM
EELS
Precipitation
Si-network

ABSTRACT

The elemental distribution of a precipitate cross section, situated in a lean Al-Mg-Si-Cu-Ag-Ge alloy, has been investigated in detail by electron energy loss spectroscopy (EELS) and aberration corrected high angle annular dark field scanning transmission electron microscopy (HAADF-STEM). A correlative analysis of the EELS data is connected to the results and discussed in detail. The energy loss maps for all relevant elements were recorded simultaneously. The good spatial resolution allows elemental distribution to be evaluated, such as by correlation functions, in addition to being compared with the HAADF image.

The fcc-Al lattice and the hexagonal Si-network within the precipitates were resolved by EELS. The combination of EELS and HAADF-STEM demonstrated that some atomic columns consist of mixed elements, a result that would be very uncertain based on one of the techniques alone. EELS elemental mapping combined with a correlative analysis have great potential for identification and quantification of small amounts of elements at the atomic scale.

1. Introduction

The 6xxx series of aluminium alloys are known to gain strength from precipitate phases which are partially coherent with the fccAl matrix and also based primarily on the main solute elements Mg and Si. The phases grow as needles during heat treatment of the alloy. Their partial coherency means strain-fields are set up in the matrix which will hinder dislocation movement. There are a number of different precipitate phases which can contribute to strength in the 6xxx series, the precipitation sequence in ternary Al-Mg-Si alloy is generally given as (Marioara et al., 2006).

SSSS → atomicclusters → GP-zones(pre-β'')(Edwardset al., 1998), (Marioaraet al., 2001) → β'' (Andersenet al., 1998), (Hastinget al., 2009) → β'(Vissersetal., 2007), $U1$(Andersenet al., 2007), U2(Andersenet al., 2005), β' → β, Si(stable)

In the precipitation sequence above, supersaturated solid solution is abbreviated 'SSSS' and Guinier-Preston-zones are abbreviated 'GP-zones'. The crystal structures of the meta-stable phases have mostly been solved by quantitative transmission electron microscopy (TEM) and first principles calculations.

Products of aluminium 6xxx alloys are processed into their final shapes by extrusion or rolling. In the case of extrusion, an important issue is how to keep energy consumption to a minimum. The extrusion process should be efficient while at the same time avoid compromising the final material properties. Pure aluminium is soft with excellent ductility. Any imperfections, like added solutes, will make glides more difficult, thus reducing ductility. While it is clear that extrusion speed can be increased by reducing the amount of solute, strain hardening rate and flow stress will decrease (Marioara et al., 2006), consequently causing a loss in strength in the final product.

In a previous study (Mørtsell et al., 2015) the overall amount of solute was reduced in a commercial 6060 Al alloy and small quantities of one or a combination of the three elements Cu, Ge and Ag were back-added as an attempt to find the optimal solution to the "strength vs extrudability issue". In this respect, composition, shape and structure of the precipitates are important parameters which can describe how mechanical properties of the material

* Corresponding author.
E-mail address: eva.mortsell@ntnu.no (E.A. Mørtsell).

http://dx.doi.org/10.1016/j.micron.2016.03.006
0968-4328/

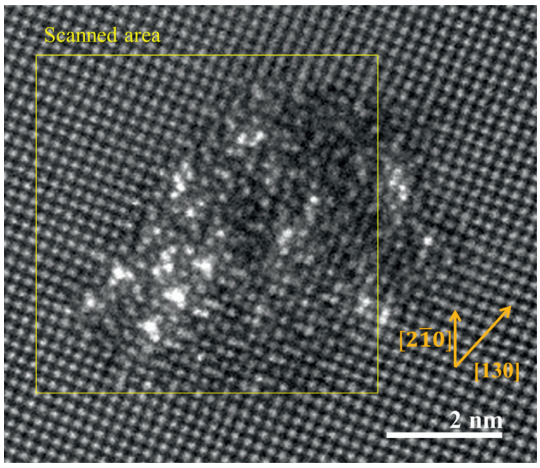

Fig. 1. HAADF-STEM image before the EELS scan of a precipitate cross section. The yellow square indicates the boundary of the area scanned for EELS mapping, the area is equivalent to the mapped regions presented in Figs. 2 and 5. (For interpretation of the references to colour in this figure legend, the reader is referred to the web version of this article).

change. When the alloy contains a higher number of different elements which enter the precipitates, they obviously become increasingly difficult to characterize at the atomic scale and they often become disordered. Disordered precipitates cannot be characterised using one distinct unit cell, since a systematic stacking cannot be detected. In the Al-Mg-Si system, because all precipitates have a similar Si-arrangement, 'disorder' pertains to a precipitate composed of small regions of different precipitate structures, from a subpart of a unit cell up to several cells. The atomic contrast in HAADF-STEM images is due to different proportions of electrons scattered to high angles by different elements. The intensity of atomic columns increases with atomic number (Z) of the elements in the scanned area (Rossel et al., 2012). HAADF-STEM images are much less affected by objective lens defocus and specimens thickness than high resolution TEM images. Since the alloy in this work has a large range of (Z, HAADF-STEM is particularly useful to study the precipitates.

Since elements like Mg, Al and Si are very close neighbours in the periodic table, and the observed atomic columns might be expected to consist of more than one element, HAADF-STEM images of the precipitates may be difficult to interpret correctly. EELS spectrum imaging can help to overcome this problem since each element adds a unique fingerprint to a spectrum through its core loss edge at a specific energy.

Previously, atomic scale EELS mapping of Cu and Ag in precipitates in 6xxx Al alloys has been executed successfully (Wenner et al., 2014), however, as far as we can see, there have been no reported studies where Mg, Si or Ge have been mapped in such precipitates. In this work we demonstrate how this technique represents a significant advance regarding analysis of precipitates in an Al-Mg-Si-Cu-Ag-Ge alloy.

2. Experimental

The composition of the investigated alloy is presented in Table 1, as measured by inductively coupled plasma optical emission spectroscopy. Symbolic representation of elements in Figs. 5 and 6 is given in (Table 2).

Table 1
Quantified alloy composition and effective solute (S_{eff}).

	Si[a]	Ge	Mg	Cu	Ag	Fe	Mn	S_{eff}[b]
wt%	0.35	0.03	0.30	0.03	0.03	0.20	0.03	0.69
at%	0.34	0.011	0.33	0.013	0.008	0.10	0.015	0.65

[a] Effective Si amount available for precipitation (Si*) is 0.05 wt% less than tabulated value (Tundal et al., 2012).
[b] Total effective solute S_{eff} = Mg + Si* + Ge + Cu + Ag.

Table 2
Symbolic representation of elements in Figs. 5 and 6.(For interpretation of the references to colour in this figure legend, the reader is referred to the web version of this article).

Elements/Height	Al	Si	Mg	Cu	Ag
z = 0.000 nm	⊕	○	⬡	◎	☆
z = 0.203 nm	●	●	■	◉	★

The alloys were cast as cylindrical billets of 4 kg. The billets were homogenized at 575 °C for 3 h and cooled to room temperature (RT) in air. The billets were extruded as round profiles with a diameter of 2 cm, and water quenched to room temperature within 5 s.

Samples (1 cm thick disks of diameter 2 cm) were cut from the extruded profiles perpendicular to the extrusion direction. The samples were solution heat treated (SHT) in an air circulating furnace for 5 min after reaching 535 °C, and immediately water quenched to RT. The samples were held at room temperature for 4 h and then subjected to artificial ageing (AA) in an air circulating furnace keeping a final temperature of 195 °C for 4 h.

TEM specimens were prepared using a TenuPol-5 electropolishing unit from Struers. The electrolyte consisted of one part HNO_3 and two parts methanol, and was kept at temperatures between −25 °C and −30 °C by adding liquid nitrogen. The specimens were finally cold-stage ion polished in a Gatan PIPS at voltages below 3 keV. The thickness of the specimen is expected to be around 30 nm in the investigated area.

A complete description of the heat treatment can be found in previously published work (Mørtsell et al., 2015), where also hardness curves and TEM precipitate statistics from the current material can be found. To minimize contamination on the specimen surfaces, plasma cleaning was performed for 7 min in O_2/Ar plasma using a Fischione plasma cleaner model 1020.

The high angle annular dark field scanning TEM (HAADF-STEM) and EELS results were obtained in a double spherical aberration (Cs) corrected JEOL ARM200F with a cold field emission gun (FEG). The microscope was equipped with a Quantum Gatan image filter (GIF). The operation voltage was 200 kV and the probe size was about 0.08 nm. The dispersion was 1.0 eV/channel. A Gatan annular dark field detector was used, where the inner and outer detector angles read 67- and 155 mrad, respectively. With a dispersion of 1 eV, the GIF gives a 2000 eV field of view.

EEL spectra were acquired in the energy loss range 280–1900 eV. This energy loss range includes the edges Ag-$M_{4,5}$ at 367 eV, Cu-$L_{2,3}$ at 931 eV, Ge-L1, 2 and 3 at 1217, Mg-K at 1305 eV, Al-K at 1560 eV and Si-K at 1839 eV. The elemental maps were created using Gatan's software package Digital Micrograph. The manual integration of EELS edges were performed after power-law background subtraction.

Auto correlation was applied to each of the EELS maps to determine their self-similarities. This was done in Digital Micrograph by first performing a Fourier transform of the map. The resulting image was multiplied by its complex conjugate, and finally an inverse Fourier transform was calculated based on the preceding image (Inc., 1999). Also, cross correlations were performed in order to check the similarities between two EELS maps. Here, a Fourier transform was performed on each of the two maps. The

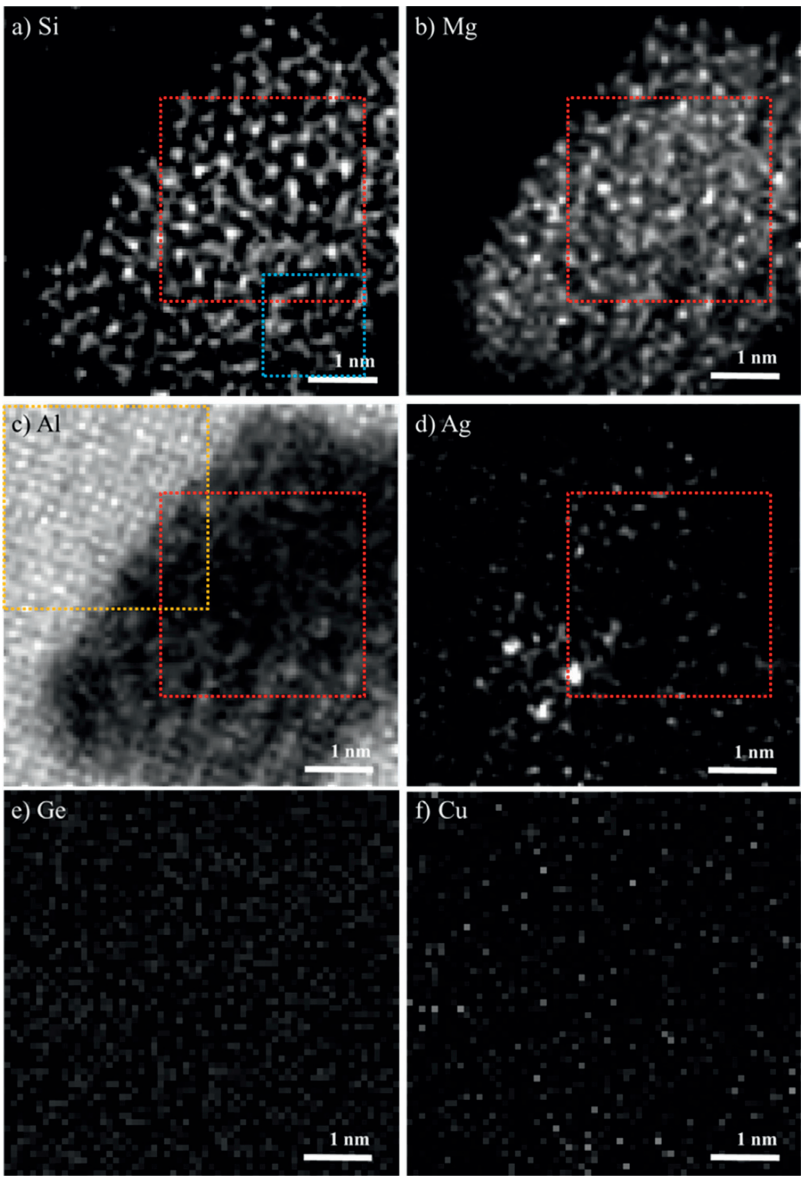

Fig. 2. EELS elemental maps, the red squares indicate areas chosen for auto correlations in Fig. 3 and cross correlations in Fig. 4 (a) Si-K edge, the blue square: auto correlation area of β'' —like features observed in the HAADF-STEM image in Fig. 1, (b) Mg-K edge, (c) Al-K edge, yellow square: auto-correlation of Al, (d) Ag-M edge, (e) Ge-L edge and (f) Cu-L edge. (For interpretation of the references to colour in this figure legend, the reader is referred to the web version of this article).

Fourier transform of the first map was then multiplied by the complex conjugate of the Fourier transform of the second map. Finally, the inverse Fourier transform of the resulting image was calculated (Inc., 1999). The maximum area from which it was possible to perform auto- and cross correlations was used in all cases, except for the Si auto correlation of the β''-like area in Fig. 3(b).

3. Results

Fig. 1 shows the raw HAADF-STEM image of the investigated precipitate cross section before the EELS scan. The area scanned by EELS is indicated in the image.

The elemental EELS maps are presented in Fig. 2, showing that Si, Mg, Al and Ag were detected within the precipitate cross section. Several intensity peaks in Fig. 2(a)–(d) correspond well with single atomic column positions in Fig. 1. However, regarding the Ge and Cu maps, the signal to noise ratio was too low to get any information.

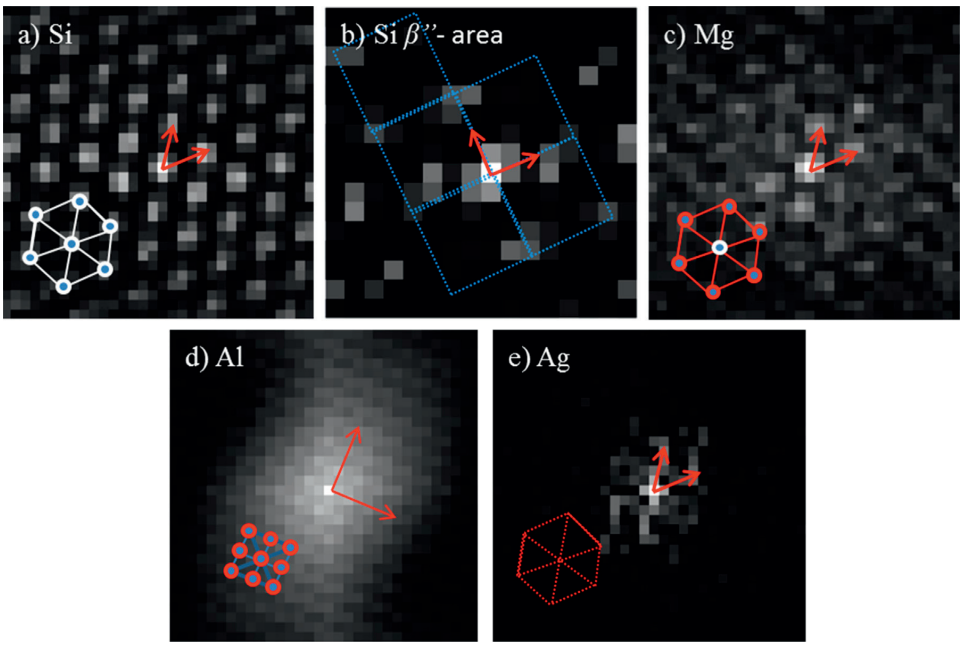

Fig. 3. Auto-correlation functions based on the EELS maps of the respective elements: (a) the Si-K edge from the area marked by a red square in Fig. 2, (b) the Si-K edge from the area marked by a blue square in Fig. 2. A square pattern appearing in addition the hexagonal pattern in (a) is highlighted with blue lines. The pattern appears larger because of the smaller selected area (c) the Mg-K edge from the area marked by a red square in Fig. 2 (b), (d) the Al-K edge from the area marked by the yellow square in Fig. 2 (c) and (e) the Ag-M edge from the area marked by the red square in Fig. 2 (d). The filled circles attached with solid lines indicate the pattern of intensity peaks in each image. The arrows illustrate vectors between intensity peaks in the auto correlation, describing areas of self-similarity in each image. (For interpretation of the references to colour in this figure legend, the reader is referred to the web version of this article).

The weak signal was a consequence of reducing the dose of the electron beam in order to preserve the sample from beam damage, also, the concentration of Ge and Cu in this particular precipitate seems to have been low. The Ge and Cu maps are still presented for comparison in Fig. 2(e) and (f), respectively. To find information on the periodicities in each EELS map, auto correlation maps were constructed for the four elements Si, Mg, Al and Ag. These are given in Fig. 3. The auto correlation map of Al is based on the Al matrix, the area is marked by a yellow square in Fig. 2(c). The residual maps are based on equivalent areas from the precipitate cross section, see Fig. 2. The comparison of similarity between the EELS maps of different elements are given by cross correlations in Fig. 4. Cross correlation is based on the same areas from the precipitate cross section when comparing two elements.

4. Discussion

The HAADF-STEM image in Fig. 1 resolves the fcc Al lattice and the atomic column arrangement of the precipitate needle cross section to be discussed. From this image it is clear that one or more element with a relatively high Z is present, particularly in the lower left region of the needle cross section, which exhibits a triangular arrangement of atomic columns. The lower right part of Fig. 1 seems to contain fragments resembling the eye-like features of the β'' phase, in which Si columns arrange in squares (Andersen et al., 1998). The β'' area is less distinct compared to the rest, suggesting that the needle does not extend all the way through the sample; consequently it should be partly covered by the Al matrix here. The remainder of the precipitate cross section seems partly disordered with fragmented triangular symmetry.

The EELS maps reveal more information about the atomic column arrangement in this complex precipitate cross section. Close investigation of the Si map in Fig. 2(a) reveals a set of distinct intensity peaks forming a hexagonal pattern across a majority of the precipitate cross section. Such hexagonal Si-networks have been discussed in several previous publications (Andersen et al., 2004), but it has not yet, to the best of our knowledge, been detected by elemental specific, atomic resolution, characterization techniques. The arrangement of Si-columns should however be square in the β''-region. There are square features in this region from Fig. 2(a), but they are not evident by eye, this is to be discussed further below.

The auto correlation of the Si map in Fig. 3(a) demonstrates the self-similarity of the Si arrangement. The pattern of intensity peaks is indicated with solid circles and solid lines. The arrows in Fig. 3 show, in simple words, how far the Si signal needs to be moved in order to coincide with itself. A hexagonal pattern clearly stands out, telling us that Si must be ordered in columns which form a hexagonal pattern in the precipitate cross section. The distance between the Si columns is approximately 4 Å when comparing the EELS map and the HAADF-STEM image. It can be concluded from this that we are in fact dealing with the above mentioned Si-network (Andersen et al., 2004). The square pattern corresponds exactly to the ordering and direction of Si columns in the β″eyes. It should be noted that the intensity peaks in Figs. 3 and 4 are more prominent along the x-direction than in the y-direction. This is because the fast scan direction is along the x-direction, causing the y-direction to be noisier.

While an overall arrangement of Mg columns from the EELS map in Fig. 2(b) is not obvious, quite a few intensity peaks stand out. The immediate impression from the Mg map is that Mg is not as bound to particular sites as Si, consequently the intensity is more diffuse

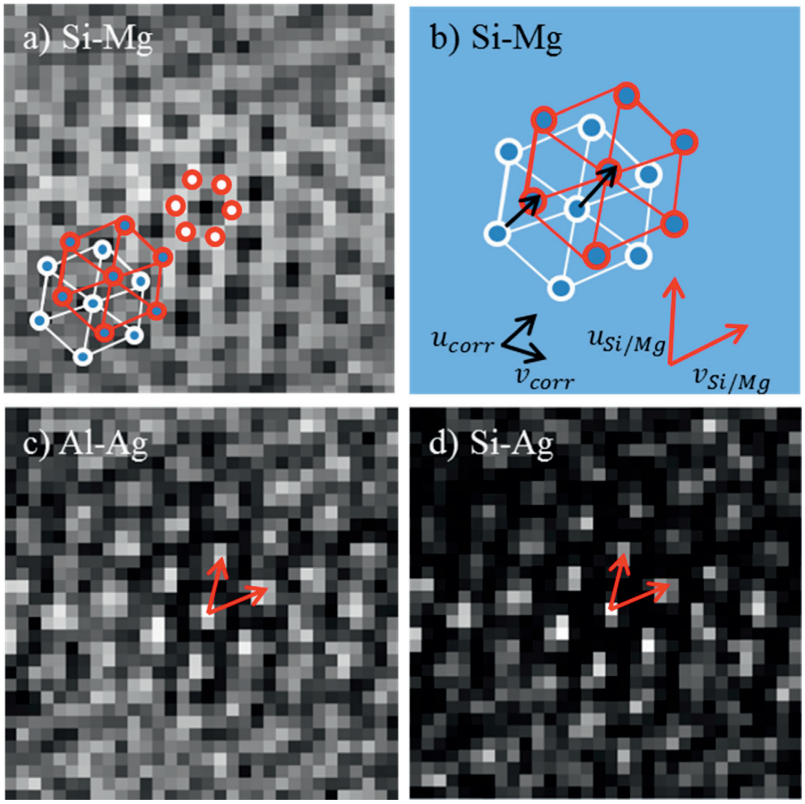

Fig. 4. Cross correlation functions based on the EELS maps: (a) Si-K edge and Mg-K edge. The red circles filled with white indicate the intensity peaks. The two hexagons illustrate the hexagonal patterns from the auto correlation of Si and Mg given in Fig. 3, (b) enlarged view of the hexagonal pattern in (a) where black arrows, marked u_{corr} and v_{corr}, illustrate the displacement of the Si intensity peaks needed to coincide with the Mg intensity peaks and vice versa. The vectors $u_{Si/Mg}$ and $v_{Si/Mg}$ in red from the auto-correlation of Si and Mg in Fig. 3 are given for comparison, (c) Al-K edge and Ag-M edge and (d) Si-K edge and Ag-M edge. Arrows indicate the displacement needed for the two signals to coincide. (For interpretation of the references to colour in this figure legend, the reader is referred to the web version of this article).

across the map. It is however clear that Mg is residing within the precipitate cross section, and there is no significant signal from the Mg-K edge in the Al matrix. The auto correlation of Mg given in Fig. 3(c) gives us some interesting additional information. It seems that sites occupied by Mg exhibit an overall hexagonal ordering within the precipitate cross section. Although more diffuse than for Si, the hexagonal pattern based on Mg in Fig. 3(c) cannot be mistaken.

When the EELS map from the Al-K edge was extracted, the Al-lattice surrounding the precipitate stands out, see Fig. 2(c). Because of the much lower density and non-continuous periodicity of Al columns inside the precipitate the signal is harder to make out here. The lower right part of the precipitate cross section, seemingly being partly overlapped by Al from Fig. 1, does indeed show an increased signal in the Al EELS map. There is also a diffuse Al signal, with some atomic columns standing out, from within the cross section. The auto correlation of Al in Fig. 3(d) shows a square pattern analogous to that of the Al lattice. It can be concluded that atomically resolved EELS picks up the periodicity of the Al lattice.

In Fig. 2(d) it becomes evident that the high intensity columns located at the lower left of the precipitate cross section must be occupied by silver. Some signal from the Ag-M edge is also emanating from other parts of the precipitate, including a diffuse intensity surrounding the obvious Ag columns.

The hexagonal Si-network is known to be replaced by a similar Ge-network when Ge is added to the alloy (Bjørge et al., 2010). The Ge-L edge could not be detected by EELS for this particular precipitate, see Fig. 2(e). One might speculate that the Si columns from the EELS map have a very small Ge occupancy based on findings in previous publications (Bjørge et al., 2010), however that the signal to noise ratio was too low to detect Ge in this case. The most probable conclusion is however that this particular precipitate does not accommodate any Ge.

From Fig. 2(f) it might be argued that a very faint Cu signal is present, although the signal is the same everywhere in the map. In Fig. 1 some known configurations usually containing Cu can be singled out. It is possible that the central atomic columns in the triangular configuration typically consisting of Cu can be replaced by other elements, since the signal is very low here (Saito et al., 2015).

Although the auto correlations of Si and Mg (Fig. 3(a) and (c)) may appear similar, cross correlating the two, see Fig. 4(a), reveals that the two are not located at the same sites in the precipitate cross section. In fact, from the cross correlated area of the precipitate cross section it can be seen that Si and Mg are never co-located at any point. This is also illustrated in Fig. 4(b) with vectors showing how the two signals must move relative to each other in order to overlap. This suggests a triangular arrangement of Mg columns surrounding each Si-network column, a model already discussed

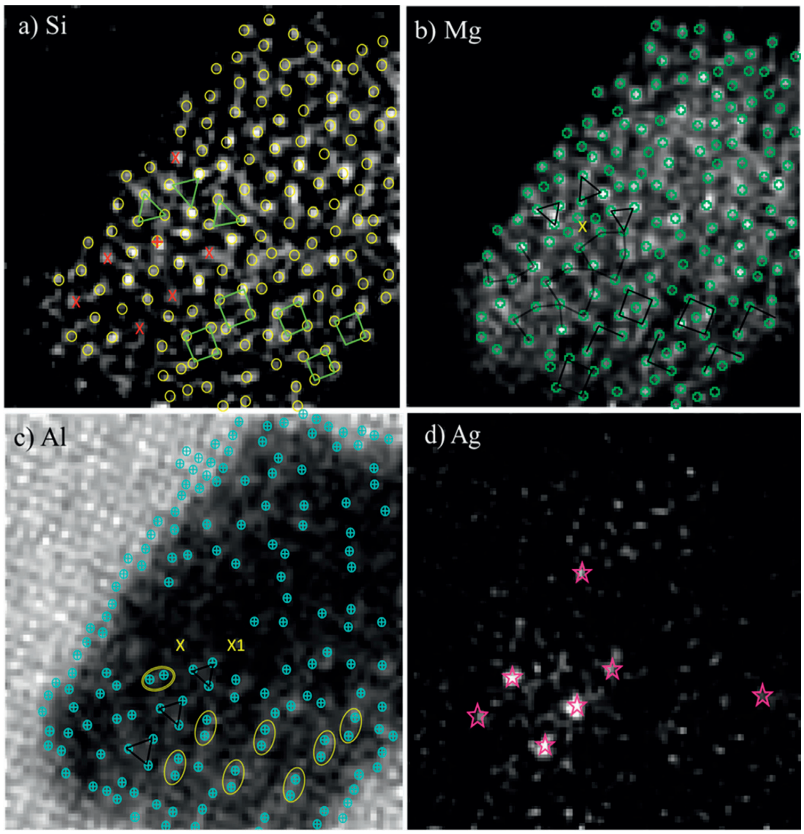

Fig. 5. EELS elemental maps of (a) The Si-K edge, (b) the Mg-K edge, (c) the Al-K edge and (d) the Ag-M edge with overlays of specific details in the atomic columns. See text for detailed explanations.(For interpretation of the references to colour in this figure legend, the reader is referred to the web version of this article.)

thoroughly by (Ehlers et al., 2014). The model suggests that a small set of local geometries can fully explain all precipitate needle cross section structures from the 6xxx alloy series. From these results, it should be possible to decompose the precipitate cross section from Fig. 1 into geometrical units based on the location of Si-network columns found in Fig. 2(a).

The cross correlation of Al and Ag in Fig. 4(c) indicates that the two elements occupy some of the same atomic columns, where the "co-occupation" forms a hexagonal pattern. Since Ag is found inside the cross section, we expect to see a tendency of hexagonal Ag ordering, as it often occupies Si column positions (Marioara et al., 2012). Since Ag exhibits a much stronger signal than Al, and it is reasonable to believe we have more Ag inside the needle precipitate than in the matrix, the cross correlation between Al and Ag from within the particle should be hexagonal.

The cross correlation between Si and Ag in Fig. 4(d) shows a very good fit between Si and Ag in the precipitate cross section. From these results it is evident that Si and Ag must occupy a significant amount of the same sites, also in areas where the signal from Ag is too low to be detected by eye.

Based on known local symmetries, the Z-contrast information of individual atomic columns and knowledge of precipitate structures in Al-Mg-Si alloys with other solute additions, we can compare the EELS maps and HAADF-STEM image and reveal the most probable atomic overlay of the columns in this precipitate cross section. As we have identified Ag to be the most likely "high Z element" present in the precipitate in Fig. 2, we will assume Si to be the element exhibiting the second highest intensity in Fig. 1. The visualization of the hexagonal Si network is shown in Fig. 5(a). Earlier work shows that the triangular symmetry marked by green triangles connecting triplets of Si atoms Fig. 5(a) most likely are Cu sites (Saito et al., 2015). The very low Cu intensity suggests that this configuration perhaps exchanges Cu with Ag. The centres of these triangles have high intensity peaks in the HAADF-STEM image, but are not shown explicitly in Fig. 5. The square configuration of the Si columns in the β'' region of the precipitate are marked with green squares in Fig. 5(a).

The intensity peaks from the Mg EELS map correspond to a significant amount of columns in the HAADF-STEM image. The atomic columns from EELS which fit well with the local geometry approach described in (Ehlers et al., 2014), are indicated with green symbols in Fig. 5(b). The Mg EELS map is, as mentioned earlier, more diffuse than the Si and Ag maps, hence low intensity areas not corresponding well with local geometries are not marked in this figure. However, some additional known Mg configurations can be identified. These particular configurations are pointed out by triangles in Fig. 5(b) correlating with those in Fig. 5(a), indicating Mg together with Si forming the triangular symmetry associated with the Cu configuration. Also, the larger triangles of black double lines indicate the column distribution of Mg which is found to exist in the β'_{Ag} phase (Marioara et al., 2012). Finally, the square arrangement of Mg columns in the equivalent positions in the β'' phase is recog-

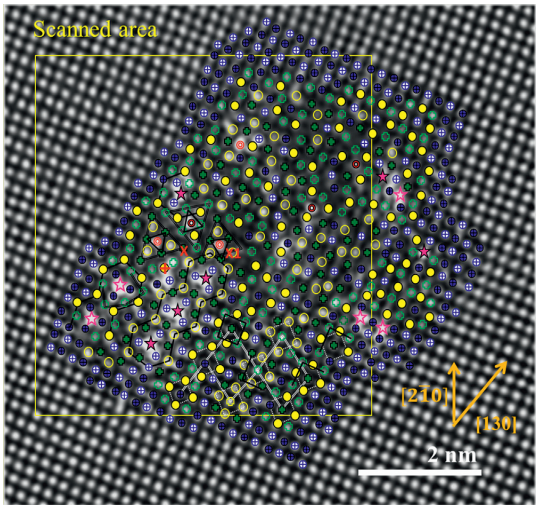

Fig. 6. Suggested atomic overlay based on the HAADF-STEM image from Fig. 1, EELS maps in Fig. 2, local geometries and the results in Figs. 3 and 4. For atomic column designation and heights, see legend in Table 2. The yellow square delimits the area of the EELS mapping, which is also equivalent to the regions presented in Figs. 2 and 5. The overlay is also based on knowledge of various precipitate structures and their internal units and symmetries (such as the square units of β" (Andersen et al., 1998) or the arrangement around Ag columns in β' (Vissers et al., 2007) together with the identification of the Si-network (Andersen et al., 2004) The known heights of the surrounding Al matrix and the necessary connections between the different structural units enable a bootstrapping of the heights over the whole cross-section. (For interpretation of the references to colour in this figure legend, the reader is referred to the web version of this article).

nised. These Mg columns are marked by squares (both complete and incomplete) in Fig. 5(b).

From Figs. 1 and 2(d) it is possible to deduce that all the obvious Ag atomic columns in the precipitate are placed in a local β'_{Ag} configuration (Marioara et al., 2012), see also the final model in Fig. 6. In this structure the three nearest atomic columns to the central Ag column are Al, as identified by EELS, see the connected black lined triangles in Fig. 5(c). These columns do however exhibit high Z-contrast in the HAADF-STEM image, which may indicate they are mixed Ag/Al-columns or that some of the intensity from the central Ag columns spills into nearby columns. It can be speculated that the hexagonal pattern in Fig. 4(c) is partly a consequence of Ag diffusing from its preferred sites and into nearby Al columns (Wenner et al., 2014).

Based on Z-contrast and local symmetry in the HAADF-STEM image, the sites marked by a red X in Fig. 5(a) should be occupied by Ag as in the β'_{Ag} phase, and signal from the Ag-M edge is, as expected, found to originate from these sites, as pointed out with stars in Fig. 5(d). However, the Si map in Fig. 5(a) also shows a significant intensity at the same sites, meaning that these columns must be mixed Ag/Si.

One column has been marked with a red '+' in Fig. 5(a). This column has a very high Z-contrast in the HAADF-STEM image and cannot only consist of Si. Consequently, the column should be mixed with one or more of the three heavier elements Ag, Cu or Ge. Taking into account the low EELS signal from Cu and Ge and that the nearby columns have a relatively high intensity in the HAADF-STEM image, it is likely that the columns are Ag enriched or subjected to intensity spread. It has been observed by Wenner et al. that Ag-rich areas do not overlap with Cu atomic columns (Wenner et al., 2014). Moreover, during the scan, silver might have diffused into nearby columns, or the intensity spread could be due to delocalization of the M-edges of silver, which can result in an apparent intensity spread to surrounding columns (Rossel et al., 2012).

An interesting site from the Mg map is marked by a yellow X in Fig. 5(b) and (c), here a weak Mg signal was detected, making it possible to consider this as a mixed Al/Mg column. According to both the C-plate and the Q-phase models (Torsæter et al.,2012), this site should be only Al, however, from quantitative nano-beam diffraction data of the Q' phase (Torsæter et al., 2008) this site should indeed be mixed Al and Mg.

The X1 site in Fig. 5(c) marks a column which according to the atomic overlay is expected to be a Si column. The EELS map of Si does certainly indicate some Si at this site, however, the Al signal from the Al map is even stronger. Since the Z-contrast of this column is relatively low, it is likely that we are dealing with a mixed Al/Si column. Determining this column to be mixed Al and Si would be impossible based on the HAADF-STEM image alone.

Based on the initial HAADF-STEM image in Fig. 1, the EELS maps in Fig. 2, correlation analysis, local geometry considerations and knowledge of previously well-known precipitate phases, we propose the model in Fig. 6 as the most probable distribution of atomic columns within the precipitate cross section. A few additional comments should be given based on the insight obtained from this analysis. By comparing Fig. 6 to Fig. 5(c) we see that the yellow ovals show pairs of Al columns which correlate to the Mg and Si pattern in Fig. 5(a) and (b), showing they are the Si3/Al sites of two neighbour molecules in β''. The yellow ovals in Fig. 5(c) indicate columns which are expected to be Al according to local geometry. Even though an Al signal is detected by EELS, the HAADF-STEM image shows high Z-contrast at the very same sites. Based on these findings, the yellow ovals are interpreted as columns of Al mixed with Ag.

Elemental mapping by EELS has a great potential for precipitate characterization on the atomic scale. By applying auto correlation and cross correlation techniques it is possible to extract global information from the elemental maps not apparent by eye. Several results from the HAADF-STEM and EELS studies could not have been attained without combining these techniques. In particular, columns in the precipitate cross section containing more than one element would be impossible to determine unequivocally.

5. Conclusions

A cross section belonging to a precipitate needle in a Al-Mg-Si-Cu-Ag-Ge 6xxx Al alloy has been investigated by HAADF-STEM, EELS and a correlative analysis of the EELS results. It has been shown that EELS elemental mapping is possible at the atomic scale for these types of precipitates and that the technique can be used to identify elements present in the precipitates. In particular, EELS could resolve the fcc lattice in the Al matrix and verify the existence of the hexagonal Si-network in 6xxx alloy precipitates. The correlative analysis based on the EELS results shows a global hexagonal arrangement of Si, Mg and Ag inside the precipitate, where Mg and Si do not coincide at any point. Specific sites where atomic columns consist of a mix of elements have been determined when combining EELS and HAADF-STEM images. Determination of mixed columns would be impossible in many cases when relying on only one of the techniques.

Acknowledgements

This work has been supported through the BIA RolEx project, no. 219371 by Hydro Aluminium and the Research Council of Norway. The TEM/STEM and EELS work was carried out on the NORTEM JEOL ARM200F, TEM Gemini Centre, Norwegian University of Science and Technology (NTNU), Norway.

References

Andersen, S.J., Zandbergen, H.W., Jansen, J., Træholt, C., Tundal, U., Reiso, O., 1998. Acta Mater. 46, 3283–3298.

Andersen, S.J., Marioara, C.D., Vissers, R., Frøseth, A.L., Derlet, P., 2004. Proc. 13th Eur. Mocr. Congr. (EMC) 2.

Andersen, S.J., Marioara, C.D., Frøseth, A., Vissers, R., Zandbergen, H.W., 2005. Mater. Sci. Eng. A 390, 127–138.

Andersen, S.J., Marioara, C.D., Vissers, R., Frøseth, A., Zandbergen, H.W., 2007. Mater. Sci. Eng. A 444, 157–169.

Bjørge, R., Marioara, C.D., Andersen, S.J., Holmestad, R., 1907. Metal. Mater. Trans. A 41, 2010.

Edwards, G.A., Stiller, K., Dunlop, G.L., Couper, M.J., 1998. Acta Mater. 46, 3893–3904.

Ehlers, F.J.H., Wenner, S., Andersen, S.J., Marioara, C.D., Lefebvre, W., Boothroyd, C.B., Holmestad, R., 2014. J. Mater. Sci. 49, 6413–6426.

Hasting, H.S., Frøseth, A.G., Andersen, S.J., Vissers, R., Walmsley, J.C., Marioara, C.D., Danoix, F., Lefebvre, W., Holmestad, R., 2009. J. Appl. Phys. 106.

Inc, G., 1999. "Fourier Processing,ïn Digital Micrograph 3.4 User's Guide. Pleasanton, Gatan, pp. 8-1–8-4.

Mørtsell, E.A., Marioara, C.D., Andersen, S.J., Røyset, J., Reiso, O., Holmestad, R., 2015. Meter. Trans. A.

Marioara, C.D., Andersen, S.J., Jansen, J., Zandbergen, H.W., 2001. Acta Mater. 49, 321–328.

Marioara, C.D., Nordmark, H., Andersen, S.J., Holmestad, R., 2006. J. Mater. Sci. 41, 471–478.

Marioara, C.D., Nakamura, J., Matsuda, K., Andersen, S.J., Holmestad, R., Sato, T., Kawabata, T., Ikeno, S., 2012. Phil. Mag. 92, 1149–1158.

Rossel, M.D., Ramasse, Q.M., Findlay, S.D., Rechberger, F., Erni, R., Niederberger, M., 2012. ASC Nano 6, 7077–7083.

Saito, T., Marioara, C.D., Andersen, S.J., Lefebvre, W., Holmestad, R., 2015. Philos.Mag. 94 (5), 520–531.

Torsæter, M., Ehlers, F.J.H., Marioara, C.D., Andersen, S.J., Holmestad, R., 2012. Philos. Mag. 92 (31), 3833–3856.

M. Torsæter, R. Vissers, C. D. Marioara, S. J. Andersen and R. Holmestad, Proceedings of ICAA11, vol. 2, p. 1338, 22–26 September 2008.

U. Tundal, O.Reiso, E. Hoff, R. Dickson and C. Devadas, in Proc. 10th International Aluminum Extrusion Technology Seminar, Miami, 2012.

Vissers, R., v. Huis, M.A., Jansen, J., Marioara, C.D., Andersen, S.J., Zandbergen, H.W., 2007. Acta Mater. 55, 3815–3823.

Wenner, S., Marioara, C.D., Ramasse, Q.M., Kepaptsoglou, D.M., Hage, F.S., Holmestad, R., 2014. Scr. Mater. 74, 92–95.

Atomistic Details of Precipitates in Lean Al-Mg-Si Alloys with Trace Additions of Ag and Ge Studied by HAADF-STEM and DFT

Submitted

Paper 4

Atomistic details of precipitates in lean Al-Mg-Si alloys with trace additions of Ag and Ge studied by HAADF-STEM and DFT

Eva A. Mørtsell*[1], Sigmund J. Andersen[2], Jesper Friis[2], Calin D. Marioara[2] and Randi Holmestad[1]

[1]Department of Physics, Norwegian University of Science and Technology (NTNU), 7491 Trondheim, Norway

[2]SINTEF Materials and Chemistry, N-7465 Trondheim, Norway

*Corresponding author. E-mail address: eva.mortsell@ntnu.no

Abstract

Bonding energies and volume misfits for alloying elements and vacancies in multi-component Al-Mg-Si alloys have been calculated using density functional theory and the results have been compared with numbers obtained by atomic scale precipitate structure analysis, using high angle annular dark-field scanning transmission electron microscopy. The techniques in combination provide new insight into precipitation in these alloys. In the Ge containing alloy were found two new stacking configurations of the well-known strengthening phase *β''*. In the alloy with Ag a new Q'/C - like local configuration containing Ag was discovered, and a model has been proposed. The experimental results are justified by simulations.

Keywords: aluminium alloys, HAADF-STEM, density-functional theory, Si/Ge, nanosized precipitates, crystal structure

1 Introduction

The current focus on environmental-friendly materials underlines the increasingly important role light metals will have to play. Aluminium alloys are light but at the same time strong, and when the products have served their purpose they can be recycled using just a fraction of the initial energy costs. They can be tailored-made with desirable combinations of material properties such as corrosion resistance, formability and ductility, which lead to reduced material usage, lower costs and longer life.

Aluminium 6xxx alloys are shaped by extrusion or rolling into products. A final ageing heat treatment hardens the products, creating nanosized semi-coherent, needle-shaped precipitates to form from the alloying elements. The precipitate needles obstruct dislocations, consequently increasing the material strength. The needles in 6xxx alloys mainly consist of Mg and Si in addition to Al itself [1] [2] [3], but other added elements may enter the precipitates as well. Elements like Li, Cu, Zn, Ag and Ge have proven to be beneficial for the nucleation and growth of precipitates, and they have consequently been added in multiple combinations and amounts [4] [5] [6] [7] [8]. It is beneficial for the extrusion and rolling processes to keep the alloys as lean as possible. Thus, we need to know how small (also combined) additions of solutes, together with heat treatment, make changes to the precipitate

microstructure (i.e. modify types of precipitates, their (dis)order, numbers, sizes and distribution). In this context, detailed knowledge about properties and behaviour of the single solute atoms in supersaturated solid solution can also be important. This concerns their interaction with the Al matrix, that is, with each other and with quenched-in vacancies. Our observations have indicated that precipitation has relation to size of the solute atom as well as to its ability to attract vacancies. We have therefore decided to look more closely into adding Ag and Ge to a lean, industrially relevant Al 6xxx alloy, relating calculated parameters like solute misfit volumes and vacancy bonding energies to experimental observations.

It has recently been found that, if a small amount of Ag is added to an Al-Mg-Si alloy GP-zone formation is enhanced, which correlates with an increased peak hardness of the material [4]. HAADF images showed that Ag occupies Al sites in the matrix as well as in the precipitate, but preferably in the immediate vicinity of the interface [9]. Despite the similar volumes and elemental (fcc) structure of Ag and Al, within the precipitate Ag does copy the behaviour of aluminium, occupying columns between Si (network) columns. In fact, Ag also occupies the otherwise autonomous Si sites. Further on, as the material overages, the β'_{Ag} phase forms [9].

Ge has been added to aluminium alloys in several preceding studies [5][10] [11]. It is clear that Ge not only passively substitutes Si, but even in very small quantities has a strong refining effect as observed upon heat treatment, yielding a distribution with smaller precipitate needles of higher number density than with only Si. The refinement corresponds with a significant increase in material strength. Although somewhat bigger, Ge clearly occupies Si sites, for example in regions based on the hexagonal column arrangement (Si-network). That Si and Ge occupy the same atomic sites/columns in a precipitate structure is understandable from their chemical similarity; both are diamond elements. However, in contrast of the apparent seamless substitution in the hexagonal Ge-network, Ge still manages to wreak havoc in most precipitate particles, causing structural disorder even to the point that no repeating unit-cell is detectable in the cross-section plane, or reducing them to assemblies of disordered fractions of known phases. The periodicity along the needles, however, is still intact. By full replacement on the expense of Si, isomorphs of the Mg-Si containing precipitates show up and more order reappears, but the β'' phase completely fails to form [10].

In age hardenable aluminium alloys, the quenched-in vacancy concentration achieved after the cooling from homogenization or solution temperatures is a very important factor for the subsequent nucleation stage of hardening precipitates, partly taking place at room temperature [12] [13]. Vacancies can assemble in clusters and form dislocation loops [13], which can later initiate inhomogeneous and coarse precipitates. The effect gets smaller with more solute and with higher vacancy affinity of the solute elements. It has been demonstrated that vacancy binding energies generally increase with atom size, however not without exception [14]. The elements used in Wolverton's work [14] have vacancy binding energies increasing as Mg, Si, Ag and Ge. A higher solute-vacancy binding corresponds with a higher probability of one or more nearby vacancies.

In this study, we wish to elucidate interesting features recently discovered in the precipitate microstructures from two selected alloys containing Ag or Ge [11]. Structural details observed in the precipitates are discussed in connection with bonding energies and volume misfits acquired through density function theory (DFT) calculations. In this respect, both Ge and Ag are convenient solute elements to investigate because of their high Z-contrast in high angle annular dark-field scanning TEM (HAADF-STEM) experiments. A major part of the results presented in this work is based on the possibilities of direct determination of atomic columns when using the HAADF-STEM technique, which is affected little by objective lens defocus and specimens thickness compared to high resolution TEM [15] [16].

2 Experimental

2.1. Materials and microscope

Table 1 shows the compositions of the investigated alloys, as measured by inductively coupled plasma optical emission spectroscopy. For a complete description of the heat treatment and TEM specimen preparation, see [11].

Table 1 Alloy composition, effective solute (S_{eff}).

		Si[a]	Ge	Mg	Ag	Fe	Mn	S_{eff} [b]
Ag added alloy	wt%	0.35	–	0.30	0.10	0.20	0.03	0.70
	at%	0.34	–	0.33	0.025	0.10	0.015	0.65
Ge added alloy	wt%	0.35	0.10	0.30	–	0.20	0.03	0.70
	at%	0.34	0.04	0.33	–	0.10	0.015	0.66

[a] Effective Si available for precipitation (Si*) is tabulated with an amount 0.05 wt % less [17].
[b] Effective solute S_{eff} = Mg+Si*+Ge+Ag.

The HAADF-STEM images in this work were acquired in a spherical aberration corrected (both probe and image) JEOL ARM200F, equipped with a cold FEG. The operation voltage was 200 kV, the probe size 0.08 nm and the inner collector angle 50 mrad. All precipitates were imaged in a <100>Al direction (here called [001]Al) along the needle/lath extension, which is normal to the cross-section.

Before insertion, the TEM specimens were decontaminated in a Fischione plasma cleaner, model 1020, for 5-7 minutes in O_2/Ar plasma.

2.2. Details for DFT calculations

DFT was applied to find bonding energies between different solute elements and/or vacancies. The lattice parameter used for the calculations is based on the relaxation of an aluminium supercell consisting of 5x5x5 aluminium unit cells. The unit cell relaxed to 20.20474 Å, i.e. a = 4.04095Å. The interaction energies are estimated from the difference between total energies. All calculations have the same cell size and parameter settings so that any systematic errors should be cancelled out. The bonding energies between two elements are calculated from 1st to 8th nearest neighbour positions. The uncertainty is quite high in the binding energy calculations, between 5 – 10 %, since the total energies of the systems which

are subtracted is about -1865 eV. It should be noted that the computed energy differences are quite small and the diffusivity consists of several components.

The Vienna ab initio simulation package (VASP) [18] [19] was used to execute the DFT calculations [20] [21], using the projector augmented wave method (PAW) within the PBE (Perdew-Burke-Ernzerhof) generalized gradient approximation. The plane wave energy cut-off was 400 eV. For all calculations gamma-centred k-points were used, with maximal k-point distances of 0.25 $Å^{-1}$ in each direction. The electronic accuracy for self-consistent loops was set at 10^{-6} eV. The atomic positions were relaxed to a maximum force of 0.001 eV/Å between atoms, using 1st order Methfessel-Paxton for smearing of partial occupation and a smearing factor of 0.2. For accurate energies, a separate calculation was performed using the tetrahedron method with Blöchl correction for the smearing.

Interaction energies are calculated based on equations (1) and (2) below.

$$E_Y = E_{Al499_Y} - \frac{499}{500} E_{Al500} \tag{1}$$

$$E_{YZ} = E_{Al498\_YZ} - \frac{498}{500} E_{Al500} - E_Y - E_Z \tag{2}$$

The calculations are based on a cell consisting of 500 Al atoms, Y and Z represents an atom or a vacancy replacing one of the Al atoms in the cell. E_Y and E_Z are the solid solution energies of atom Y and Z respectively. The interaction energy between the two elements Y and Z in the Al cell is calculated by subtracting the solid solution energies of each element from the total electronic energy of the cell. A more detailed explanation of calculating formation energies of structures and solid solution energies of atoms are explained by Ninive et al. in [22].

3 Results

3.1 Interaction energies and volume misfits

Fig. 1 illustrates the interaction energies, as calculated by DFT, between a number of elements including Mg, Ge and Ag in all combinations and the interaction of all three with a vacancy (designated X) in aluminium, as a function of interatomic fcc distances up to two unit distances (8.1 Å). The two first represent the nearest neighbour distance (2.86 Å), and the extent of the unit cell (4.05 Å). The calculations clearly suggest that Ge binds more strongly to vacancies than any of the other alloying elements in this work, while the least favourable arrangement is two vacancies as nearest neighbours.

The calculation of volume misfits of all the relevant elements and vacancies (X) are presented in Fig. 2. The volume of Si is according to Leyson et al. about 13.95 $Å^3$ [23]. Our calculations returned a volume for Si about 13.77Å and that of Ge of about 18.43 $Å^3$. It should be noted that a misfit volume here represents the net expansion or contraction of the entire supercell relative to the substitution of one Al atom by a solute atom or vacancy at 0 K.

As the real situation is more complex, a solute atom can be near other solute atoms and vacancies at times. The time spent in the vicinity of each other will depend on the interaction energy at the particular site. A solute-solute or solute-vacancy pair will have more possibilities to deform the surroundings in order to reduce the energy and misfit than a single solute atom. Also, lattice vibrations at ambient temperature further complicate the picture. This means that the theoretical misfit volumes in Fig. 2 cannot be taken as absolutes. They may be considered as ideal maximum values of isolated solute elements in Al, comparable in a relative sense. The solute-solute or solute-vacancy binding energies give clues about which pairs are likely to reduce the misfit. For example, of the elements in Fig. 1 the bonding between Ge and a vacancy (Ge-X) when on nearest neighbour positions is very low. This means there is a high likelihood of finding a vacancy as nearest neighbour to a Ge atom, something that should tend to relax the surrounding matrix of the pair. The situation is more complex as two or more solutes also attract vacancies and more solute, and as binding energy varies with distance (Fig. 1). An analysis of the information given in Figs. 1 and 2 will be connected to experimental results and presented in the "Discussion" section.

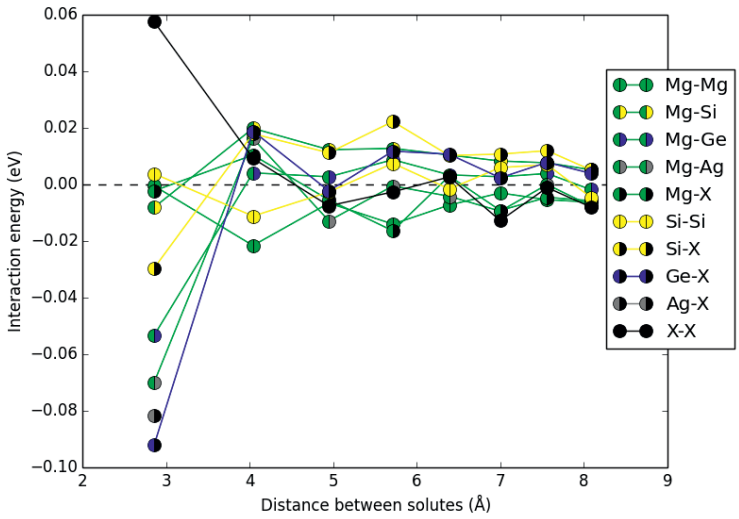

Fig. 1 Interaction energies between the alloying elements and/or vacancies (X) in fcc aluminium as a function of separation distance, from 1st to 8th nearest neighbours.

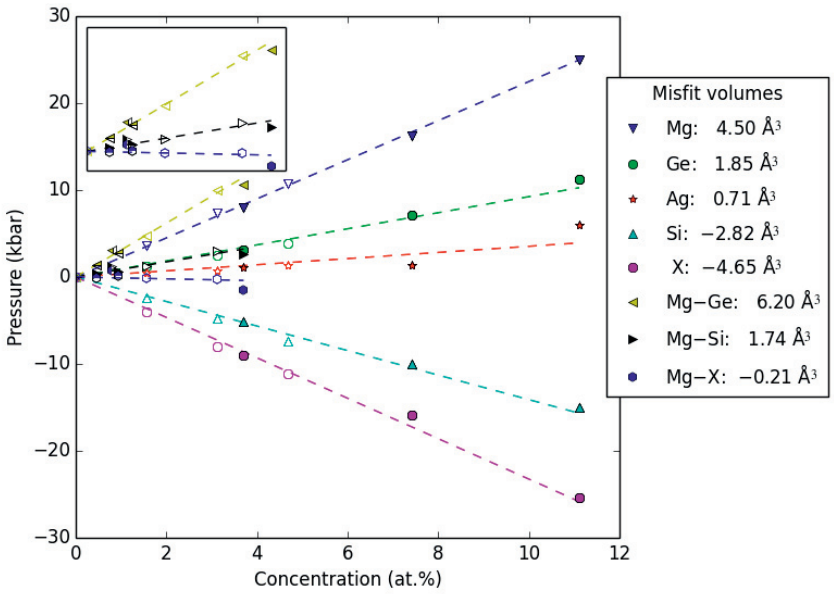

Fig. 2 Misfit volumes of the alloying elements and vacancies (X) in fcc aluminium. For single elements in Al: the open symbols indicate calculations based on 3x3x3 primitive cells (27 atoms) and the filled symbols indicate calculations based on 4x4x4 primitive cells (64 atoms). For pairs of elements in Al (insert): open symbols indicate calculations based on 1 pair in 3x3x3, 4x4x4, 5x5x5 and 6x6x6 primitive cells and filled symbols indicate 2 pairs in 4x4x4 and 6x6x6 primitive cells. Dashed lines show linear fits to the data for each element or pair. The misfit volumes are calculated from the slopes as described in [23].

3.2 Detailed overview of precipitate microstructure

Both the Ag - and the Ge - added alloy contained a high number density of the hardening phases, with discernible contents of all added elements. For a complete overview of statistics and comparisons see [11].

Since the hardening phases are all needle/lath shaped along <001> Al, the images show cross-sections with Al and precipitate columns in parallel with this zone axis. In Fig. 3 one representative precipitate (cross section) is given from each alloy. Figs. 4, 5 and 6 have full atomic overlay, based on the Z-contrast from HAADF-STEM, inter-atomic distances and local similarities with well-known structures in the Al-Mg-Si/Ge system (see also [6], [9] and [24]).

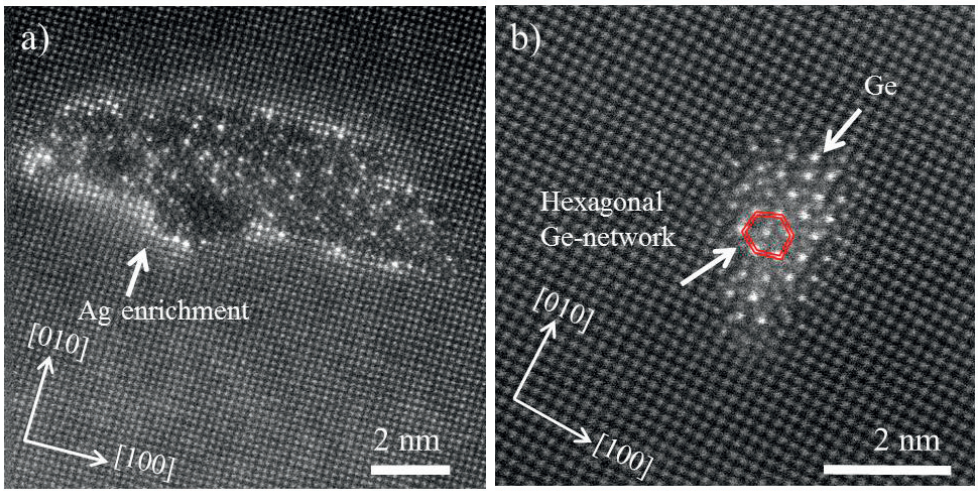

Fig. 3 HAADF STEM raw images of typical precipitate cross-sections from the two alloys illustrating that both Ag and Ge enter and strongly affect atomic structure. **a)** Large lath-shaped precipitate in Ag added alloy. The high contrast just outside the interface suggests a considerable amount of Ag fully or partly occupying the Al columns. **b)** A smaller precipitate in the Ge added alloy. The red, double lined hexagon indicates the Ge-network which is extending over the entire precipitate cross section. Very high intensity at these sites verifies the presence of Ge.

3.2.1 Ag added alloy

The silver added alloy contained relatively large precipitates, coarsely distributed in the matrix; see Figs. 3 (a) and 4. The precipitate cross sections had several features in common; in particular, Ag segregation in the matrix near the precipitate interface. Also, fragments of the β'_{Ag} phase appeared frequently together with disordered regions [11]. Interestingly, a new precipitate configuration containing Ag was observed. Similar configurations are normally reported to exist in Cu containing 6xxx alloys and are referred to as Q' or C-plate [6] [25]. In the present study, the "Cu-sites" in the Q'/C - like phase were occupied by Ag. An example of this stacking is given in Fig. 4, where the Q'/C - like local atomic configuration is indicated with yellow, double-lined triangles, hosting an Ag column in its centre. There also seems to be a dislocation progressing along the <010> Al direction through the precipitate, an approximate starting point is indicated by the yellow arrow in Fig. 4.

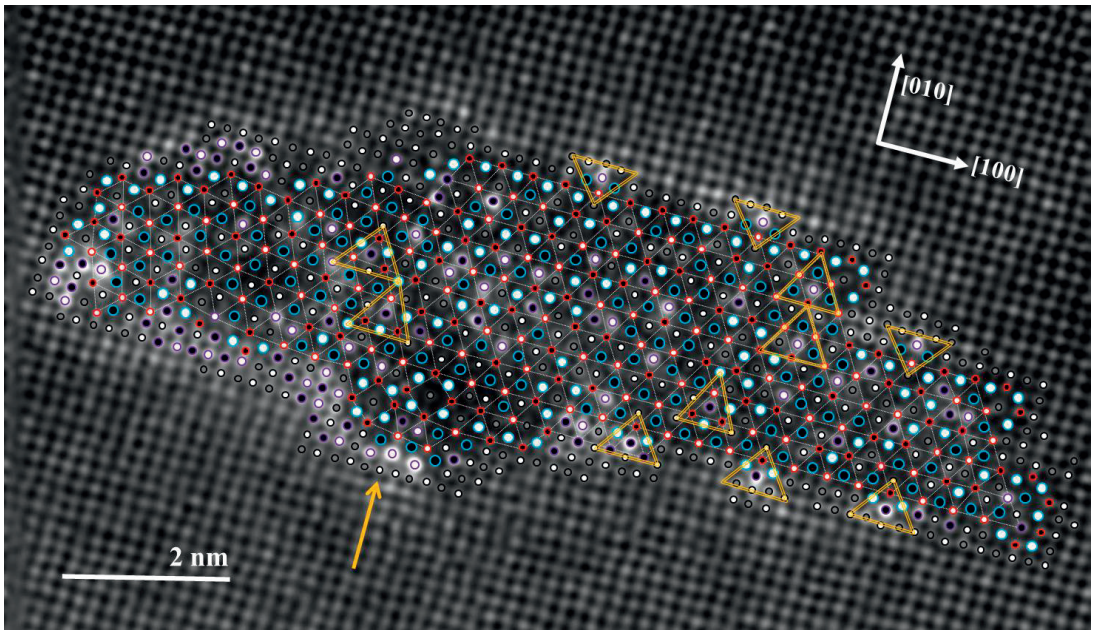

Fig. 4 Precipitate cross section in the Ag added alloy with atomic overlay, see Fig. 3 (a) for the original image. The segregation of Ag at the precipitate-matrix interface is evident. The hexagonal Si-network is indicated with dashed, white lines. The Q'/C - like local configurations, where Cu sites are replaced by Ag, are indicated with yellow triangles. For explanation of the symbolic representation of elements, see legend in Table 2.

3.2.1 *β"* stacking variations in the Ge added alloy

Version β_2"

Several of the precipitates in the Ge-added alloy demonstrated a second ordering of the "eye-like" *β"* molecules, this version of the *β"* phase will hereafter be referred to as β_2". An example of a precipitate cross section incorporating both regular *β"*, indicated by yellow lines, and the new β_2", indicated by white dashed lines, is given in Fig. 5 below. The smallest white squares inside the parallelograms show the location of the "vacated columns", also marked by X in Fig. 5 (b).

The β_2" cell consists of 22 atoms in the projected plane, corresponding to a supercell in the fcc Al lattice of 24 atoms. It should be noted that the common *β"* cell consists of 22 atoms, with an Al supercell of 22 atoms. Both β_2" and normal *β"* fulfil the requirements of space group C2/m, however the c-axis of β_2" lies along <100> Al instead of the usual Al <130> in *β"*. The ideal composition of β_2" is similar to that of *β"*, except for two additional "vacated atomic columns". The composition is given as $Al_6Mg_8D_8X_2$, where D is a mix of Ge and Si, and X here represents a vacant column (see also Fig. 5 (b)). The Si columns in both phases can all be described as "contained by rhombuses" that are pairs of isosceles triangles assembled in different ways. The triangles are the Si network cells of *β"*. In the supercells on the Al matrix, the triangles are bound by <100> Al and <120> Al directions. In the normal

β" phase, the two triangles are joined on a <120> plane (common leg), as pointed out by red arrows in Fig. 5 (b). In the second *β₂"* variant the bases of the triangles meet on a (100) plane, pointed out by yellow arrows in Fig. 5 (b).

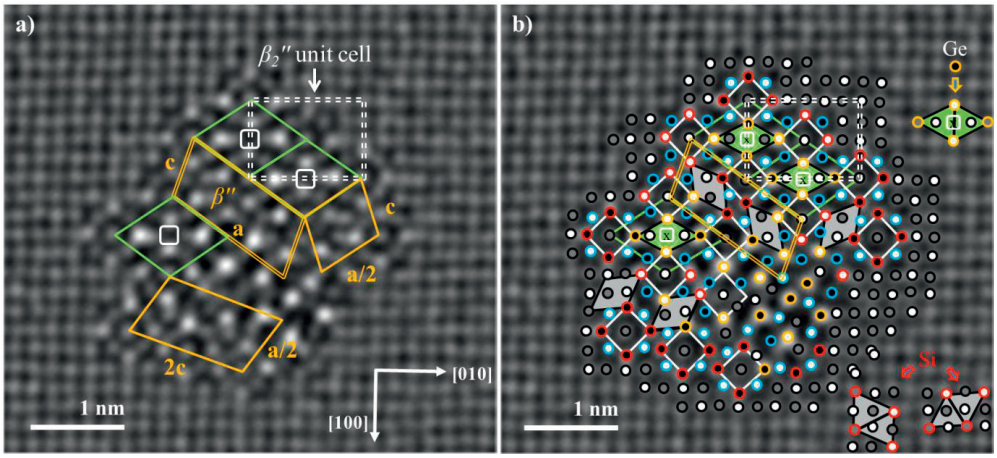

Fig. 5 Atomic overlay on the cross section of a precipitate in the Ge-added alloy. Determination of a particular column is based on knowledge of the structures / molecules, intensities in from HAADF-STEM and interatomic distances. See legend in Table 2. In (a) ***a*** = <320> a_{Al} = 14.6 Å and ***c*** = ½ <130> a_{Al} = 6.40Å. Yellow parallelograms indicate *β"* regions and white, green parallelograms indicate *β₂"* regions. A *β₂"* unit cell is indicated by white dashed lines.

Table 2 Symbolic representation of overlay of elements in Figs. 4, 5, 6 and 7.

Elements / Height	Al	Si	Mg	Ge/Si (D)	Ag/Al
z = 0.000 nm	○	○	○	○	○
z = 0.203 nm	●	●	●	●	●

Version *β₃"*

A third version of the *β"* phase was discovered in the Ge containing alloy, this phase will hereafter be referred to as *β₃"*. This stacking variant was not observed as frequently as *β₂"*, but it occurred occasionally as a fragment in cross sections, combined with *β"*. A cross section incorporating both the *β"* and the *β₃"* configuration is shown in Fig. 6. The *β₃"* region is marked by white dashed lines. The phase fulfils the requirements of space group C2/m with an ideal composition $Al_{10}Mg_8D_8$. This phase has a cell consisting of 26 atoms; simultaneously its supercell in the Al matrix also covers 26 atoms. The deviation in composition between *β₃"* and '*β"*and *β₂"'* is the additional Al columns in the cell.

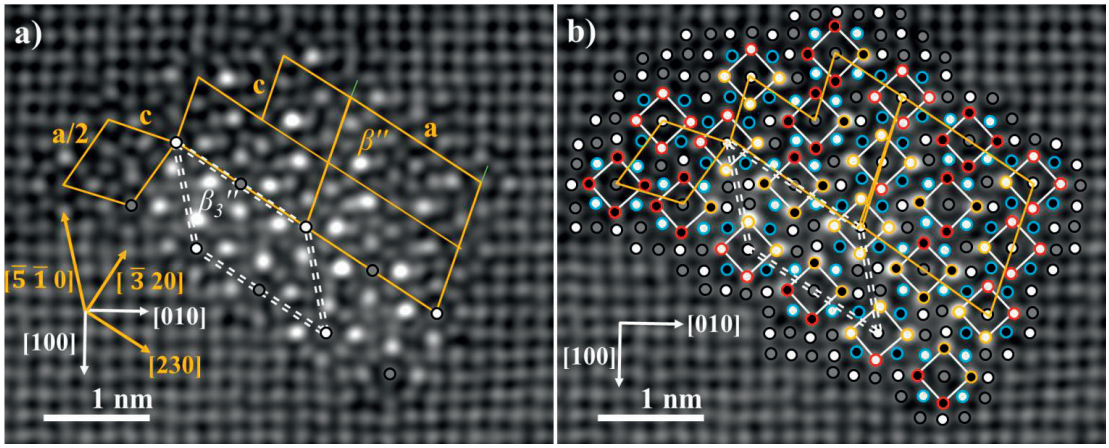

Fig 6. Precipitate exhibiting the *β₃"* (white dashed lines) stacking variation of molecules of *β"*. The regular *β"* regions are indicated with yellow solid lines. For explanation of the symbolic representation of elements in (b), see Table 2.

The c-axis of *β₃"* lies along <-5-10> Al instead of <130> Al in *β"*, while the a-axis lies along <230> Al for both variants. The difference between the two could be described as shifting the bottom row of *β"*-eyes with ≈ ***a***/2 in parallel to the a-axis, consequently the angle between ***a*** and ***c*** is 135° for *β₃"*. This shift is present in a Ge-rich area of the cross section; see Fig. 6 (b).

4 Discussion

4.1 Interaction energies and volume misfits

In Fig. 1 Mg-Si nearest neighbour (NN) interaction energy clearly shows that Mg and Si like to be at NN places, that is, it is favourable for these two elements to aggregate pairwise in Al. This result is backed up by the volume misfits in Fig. 2, where a Si atom will contract the Al lattice surrounding it, and Mg will expand it. Combined, Mg and Si seem to lower their misfit in the Al lattice, shown in the insert in Fig. 2. From Fig. 1 and 2 the most favourable Si-Si and Mg-Mg distance in fcc Al is 4.05Å. This would confirm the most common observation for the precipitates: Firstly, that Mg and Si can stay in columns along <001> Al (as they do in parallel with the precipitate extension), and secondly that such columns could alternate along the other <100> Al directions, with atoms as first NNs and columns separated by 2.025Å.

As shown in Fig. 1, Mg very weakly attracts vacancies in NN position and then seems to repulse them as 2nd NN. Successively Mg starts to attract vacancies at 3rd and 4th NN positions. The result showing that Mg does not seem to repel vacancies when in 1st NN position corresponds well with the results presented by Wolverton [14]. This indicates that both vacancies and Mg attract the valence electrons less than what Al itself does. From Fig. 2 it is clear that Mg will expand the Al lattice and intuitively this should attract a vacancy. When calculating the volume misfit of Mg and X together, as shown in Fig. 2, we see that the misfit becomes lower than that of Mg or X alone.

Ag should pull strongly on vacancies according to Fig. 1. The precipitate distribution in the Ag-added alloy is however very coarse in comparison, meaning that it does not seem to initiate a high number of nucleation sites, as Ge does. The volume misfit of Ag in Al is however very small. Pure Ag is fcc, as Al itself, and has a relatively high solubility in Al [26]. In the vicinity of a precipitate there would be regions with expansive and contractive strain, meaning slightly more and less space for the solute. We believe this could explain the tendency of Ag accumulating in the Al lattice close to the particle. This also means that for Ag, the most important factor in precipitation should be its volume and its ability to attract vacancies comes in second.

Based on the calculations given in Fig. 1, Ge should pull more strongly on Mg as a NN than Si does. Also, as Ge has a stronger pull on vacancies than Si does, it should be more effective at nucleating clusters. It seems likely that the attraction on both Mg and a vacancy is significant for the ability of Ge to procure favourable nucleation sites for precipitate needles. This result also explains why Ge is mostly localised at the centre of the precipitates, which indicates it is active in the nucleation and growth of the needles from the very beginning. Ge is significantly larger than Si and expands the Al lattice, as opposed to contracting it as Si does, see Fig. 2. It is curious that the Mg-Ge interaction seems favourable at 1st NN places, see Fig. 1, meaning that in the beginning it cannot be the search for minimizing the lattice strain which sets off this aggregation. It is apparent that the charge distribution overcomes the disadvantage of volume misfit as Ge is added to the alloy.

Since the calculations are based on one atom in a (repeated) supercell for all solute elements, this means there is no surface to go to for the solute. Neither the atom nor the vacancy may cross the cell boundary and form a cluster. It should be noted that it is therefore difficult to draw conclusions regarding diffusion based on vacancy binding alone.

4.2 Ag added alloy

The small volume misfit of Ag in Al shown in Fig. 2 is supported by the features seen in Fig. 6, as Ag enriches the Al columns at the interface between the precipitate and the Al matrix. The hexagonal Si-network is present in a major part of this precipitate and is indicated with white triangles. The Si columns are separated by approximately 0.4 nm and the networks height distribution is unique for the precipitate structure [27]. Silver is undoubtedly present inside the precipitate cross section, but it is difficult to establish the occupancy of Ag in the atomic columns, as it is likely they also contain Al [28].

An interesting feature in the precipitate cross section presented in Figs. 3 (a) and 4 is the presence of Q'/C -, or β' -like fragments. These fragments are indicated by yellow triangles and were found both at the interface and within the precipitate. Q' and C-plate are documented in Cu-containing alloys and atomistic models have been proposed [6] [25]. In this case, no Cu has been added to the alloy, and the impurity level of Cu is too low for this phase to form. Because of the high Z-contrast in the HAADF-STEM images, the Q'/C sites which usually contain Cu must consequently be occupied by Ag in these precipitates. A model of the new Q'/C - like phase, based on the experimental results and [6] [25] is given in

Fig. 7. This shows how it is not only the volume misfits of the solute atoms, Fig. 2, which contribute to the phase formation. Although disposed to occupying Al sites because of similar size, Ag occupies additional sites within the precipitate because of its high interaction energies to other solute elements in Al. From Fig. 1 we see that the interaction energy between Ag and Mg is about – 0.7 eV, which is relatively strong compared to many of the other solute combinations. Based on this result we should expect to also find Ag incorporated in the precipitate structure, interacting with, among other elements, Mg. This is indeed found for both the Q'/C - like phase in Fig. 3, and at Ag sites in Fig. 4. DFT calculations confirmed that it is energetically favourable for the Q' phase to form in Al, and it does not cost much energy as the change in cell parameter is small.

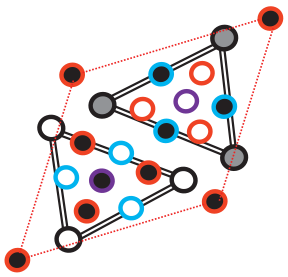

Fig. 7 Model of the Q'/C - like local configuration, where Ag occupies the site at the centre of the double-lined triangles. Symbols as in Table 2. The model is adapted from the model of the Cu-containing phase in [6].

4.3 *β"* stacking variations in the Ge added alloy

Models of the three *β"* variants are shown in Fig. 8, with the corresponding lattice parameters and other characteristics in Table 3. Other compositions are suggested for regular *β"* [1] with respect to the amount of Al or Mg in each unit cell. For simplicity, we here assume Al occupies the centre of each "eye" although this position can contain both Al and Mg [1]. The same applies for the sites often referred to as Si-3 sites since previous works have shown they are flexible, but usually containing Al in the interface [1]; see Fig. 8.

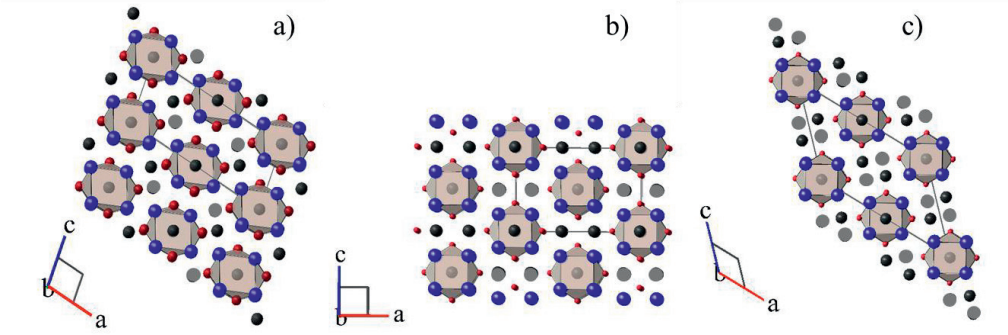

Fig. 8 The three stacking variations of *β"*, all containing two *β"* - eyes per unit cell: **(a)** Normal *β"* **(b)** β_2*"* and **(c)** β_3*"*. The symbolic representation is as follows: black = Al, blue =

Mg and red = Si. The shaded squares and Al atomic columns indicate z = 0.203 nm, while the "non-shaded squares and Al atomic columns" indicate z = 0 nm.

Table 3 Overview of *β"* precipitation variants in the Al-Mg-Si-Ge system. D denotes a mix of Ge and Si. Vacated columns are here denoted X and should not be confused with a single vacancy.

Phase	Composition	Space group	Lattice parameters [Å]
β"	$Mg_8D_8Al_6$	C2/m	a = 15.16, b = 4.05, c = 6.74, $\beta = 105.3°$
β_2"	$Mg_8D_8Al_6X_2$	C2/m	a = 12.15, b = 4.05, c = 8.1, $\beta = 90°$
β_3"	$Mg_8D_8Al_{10}$	C2/m	a = 15.16, b = 4.05, c = 10.33, $\beta = 135°$

4.3.1 Version *β_2"*

From Fig. 8 we see that the normal *β"* structure has "eyes", each claiming two Al columns (in (a), one Al column on both horizontal sides of the molecule), which account for all Al-columns within the cell. *β_2"* contains the same number of eyes and Al columns per molecule, but the alternative ordering means that the unit cell sheds one atomic column relative to the Al super-cell compared to regular *β"*, see Figs. 5 (a) and (b). The two missing columns in the *β_2"* structure means that vacancies must have been absorbed in the process of forming from solutes on fcc positions in the matrix. That *β_2"* lacks two columns compared to *β"* means that the same amount of atomic columns (same number of molecules) occupy a larger volume in the Al matrix. Using the extracted unit distances and if we assume the expansion only to occur in the precipitate normal plane, the cross-section area increases by 4 %. For a cylinder, this gives 2 % radial expansion. Consequently the tension needed to create an interface dislocation is lowered when the *β_2"* stacking occurs. This precipitate type would therefore aid the struggle of keeping added solute to a minimum in lean 6xxx alloys, while at the same time maintaining the material strength.

The *β_2"* stacking has been observed in similar Al-Mg-Si alloys, but only as one rhombic unit consisting of four "eyes", hence, it seems Ge is the reason why it becomes energetically favourable for *β_2"* to grow more. DFT simulations of precipitates containing both Si and Ge showed that removing the atomic column marked by X in Fig. 5 (b) is indeed energetically favourable for an infinitely long precipitate, and more so for precipitates containing Ge. Moreover, the energy required to form a unit cell of *β_2"* is less than that required to form a unit cell of normal *β"*. DFT revealed it to be advantageous to replace Si with Ge in *β_2"*, which is exactly what we observe. Another interesting feature of *β_2"* is its c-axis lying along <100> Al instead of <130> Al. It has been reported by Bjørge et al. how completely replacing Si by Ge in 6xxx alloys leads to precipitate phases with c-axis lying along <100> Al [10], and no *β"* phases form anymore. Normally, the Si-network aligns along <130> Al, however, as Si is replaced by Ge, the hexagonal Ge/Si-network aligns along the <100> Al

direction. The β_2'' phase could indeed be an intermediate phase variation in this retrospect, where also here Ge additions cause the c-axis to shift towards the <100> Al direction.

From the NN perspective in Fig. 1 it seems very probable that Mg and Ge would interact closely in the precipitation process, especially since the interaction energy is about five times larger than that between Si and Mg. However, from the misfit volumes in Fig. 2, Mg and Ge has a higher volume misfit as a pair than Mg and Si. When considering the volume of the three stacking variations in Fig. 8, it is clear that β_2'' has a higher volume per "eye" than β''. It seems that the bonding energy between Ge and Mg is high enough to override the relatively large volume misfit of the "eye-like" β'' structure caused by this combination of elements, and we obtain eyes with Ge occupying Si-sites. Ultimately, it appears that these Ge-containing eyes are more likely to form other stacking variations because of higher volume misfit with the Al matrix.

4.3.2 Version β_3''

The β_3'' phase has a cell consisting of the same number of atomic columns as its corresponding supercell in Al (26 to 26). β_3'' does not contain any vacated columns, but more Al columns than both β'' and β_2''. As seen in Fig. 8 (c), there are two extra Al-columns per "eye", that is, 8 per two 'β'' eyes' instead of 4. More Al inside the precipitate is often associated with a more loosely bound structure, yielding it less efficient as a dislocation impediment. It is possible that we are dealing with a phase normally occurring early in the precipitation sequence, and that upon further heat treatment it would transform into β'' or β_2''. As shown in Fig. 6 the c-axis lies along <-5 -1 0> Al. This stacking variation leads to the largest unit cell of the three variants presented in Fig. 8 because of the additional Al columns. The supercell in Al has the same number of atomic columns as the unit cell of β_3''. It could be argued that this phase has a lower Ge content than β_3'', making the volume misfit with the Al lattice less crucial.

5 Conclusions

Two lean, industrially relevant Al-Mg-Si alloys with Ag or Ge additions were investigated. Precipitate microstructure was examined in detail by HAADF-STEM and the results were corroborated by DFT simulations.

In the Ag added alloy, a version of the Q'/C – local configuration, containing Ag at the Cu - sites was discovered. The low misfit volume of Ag in Al explains why silver often occupies Al columns at the interface of the precipitate surfaces. High binding energies to vacancies and Mg at the same time explain why silver also enters the precipitate structure and sometimes behaves like Cu.

Two new stacking variations of the β'' phase, referred to as β_2'' and β_3'', were discovered in the Ge-added alloy. Germanium's high affinity to vacancies suggests that the element creates more nucleation sites for precipitate needles, thus refining the precipitate microstructure. β_2'' only appears frequently in the Ge-added alloy. This phase sheds two atomic columns relative to the Al matrix. DFT simulations showed this to be energetically favourable. A high

occupancy of Ge together with Mg inside the precipitate structure requires a change in the stacking of *β''*-eyes because of higher volume misfit in Al. The third variant of the *β''*-phase, β_3'', might be associated with an intermediate phase early in the precipitation sequence because of its higher Al content.

Acknowledgements

Hydro Aluminium and the Research Council of Norway are greatly acknowledged for their support through the BIA RolEx project, no. 219371. The TEM and STEM work was carried out on the NORTEM JEOL ARM200F in the TEM Gemini Centre at NTNU, Norway. This research was supported in part with computational resources provided by NOTUR, http://www.sigma2.no.

Bibliography

[1] H. S. Hasting, A. G. Frøseth, S. J. Andersen, R. Vissers, J. C. Walmsley, C. D. Marioara, F. Danoix, W. Lefebvre and R. Holmestad, *J. Appl. Phys.,* vol. 106, 2009.

[2] C. D. Marioara, H. Nordmark, S. J. Andersen and R. Holmestad, *J. Mater. Sci.,* vol. 41, pp. 471 - 478, 2006.

[3] R. Vissers, M. A. v. Huis, J. Jansen and C. D. M. S. J. A. H. W. Zandbergen, *Acta Mater. ,* vol. 55, pp. 3815 - 3823, 2007.

[4] M. Kubota, J. F. Nie and B. C. Muddle, "Characterization of Precipitation hardening responce and as-Quenched Microstructures in Al-Mg(-Ag) alloys," *Mater. Trans.,* vol. 45, pp. 3256 - 3263, 2012.

[5] K. Matsuda, S. Ikeno and T. Munekata, "HRTEM Study of Precipitates in Al-Mg-Si and Al-Mg-Ge Alloys," *Mater. Sci. Forum,* Vols. 519 - 521, p. 221, 2006.

[6] T. Saito, C. D. Marioara, S. J. Andersen, W. Lefebvre and R. Holmestad, "Aberration-corrected HAADF-STEM investigations of precipitate structures in Al-Mg-Si alloys with low Cu additions," *Philosophical Magazine,* vol. 94, no. 5, pp. 520 - 531, 2015.

[7] K. Stiller, P. J. Warren, V. Hansen, J. Angenete and J. Gjønnes, "Investigation of precipitation in an Al-Zn-Mg alloy after two step ageing treatment at 100C and 150C," *Materials Science and Engineering: A,* vol. 270, no. 1, pp. 55 - 63, 1999.

[8] F. W. Gayle and J. B. V. Sande, "Composite precipitates in an AlLiZr alloy," *Scripta Metallurgica,* vol. 18, no. 5, pp. 473 - 478, 1984.

[9] C. D. Marioara, J. Nakamura, K. Matsuda, S. J. Andersen, R. Holmestad, T. Sato, T. Kawabata and S. Ikeno, *Phil. Mag.,* vol. 92, pp. 1149 - 1158, 2012.

[10] R. Bjørge, C. D. Marioara, S. J. Andersen and R. Holmestad, *Metal. Mater. Trans. A,* vol. 41, p. 1907, 2010.

[11] E. A. Mørtsell, C. D. Marioara, S. J. Andersen, J. Røyset, O. Reiso and R. Holmestad, *Metallurgical and Materials Transactions A,* vol. 46, no. 9, pp. 4369 - 4379, 2015.

[12] L. A. Westfall, "An investigation of nano-voids in quenched aluminium by small-angle x-ray scattering," Queen's University, Kingston, Ontario, Canada, 2008.

[13] V. Gavini, K. Bhattacharya and M. Ortiz, "Vacancy clustering and prismatic dislocation loop formation in aluminium," *Phys. Rev. B,* vol. 76, p. 180101, 2007.

[14] C. Wolverton, *Acta Mater. ,* vol. 55, pp. 5867 - 5872, 2007.

[15] T. Yamazaki, M. Kawasaki, K. Watanabe, I. Hashimoto and M. Shiojiri, *Ultramicroscopy,* vol. 92, p. 181, 2002.

[16] P. D. Nellist and S. J. Pennycook, *Ultramicroscopy,* vol. 78, p. 111, 1999.

[17] U. Tundal, O.Reiso, E. Hoff, R. Dickson and C. Devadas, in *Proc. 10th International Aluminum Extrusion Technology Seminar*, Miami, 2012.

[18] G. Kresse and J. Hafner, "Ab initio molecular dynamics for liquid metals," *Phys. Rev. B,* vol. 32, pp. R558 - R561, 1993.

[19] G. Kresse and J. Furthmüller, "Efficiency of ab initio total energy calculations for metals and semiconductors using a plane wave basis set.," *Comput. Mater. Sci.,* vol. 6, pp. 15 - 50, 1996.

[20] P. Hohenberg and W. Kohn, "Inhomogeneous Electron Gas," *Phys. Rev.,* vol. 136, pp. B864 - B871, 1964.

[21] K. W. and S. L. J., "Self-Consistent Equations Including Exchange and Correlation Effects," *Phys. Rev.,* vol. 140, pp. A1133 - A1138, 1965.

[22] P. H. Ninive, A. Strandlie, S. Gulbrandsen-Dahl, W. Lefebvre, C. D. Marioara, S. J. Andersen, J. Friis, R. Holmestad and O. M. Løvvik, "Detailed atomistic insight itno the beta" phase in Al-Mg-Si alloys," *Acta Materialia,* vol. 69, pp. 126 - 134, 2014.

[23] G. P. M. Leyson, L. G. Hector and W. A. Curtin, "Solute strengthening from first principles and application to aluminum alloys," *Acta Mat.,* vol. 60, pp. 3873 - 3884, 2012.

[24] M. Torsæter, F. J. H. Ehlers, C. D. Marioara, S. J. Andersen and R. Holmestad, "Applying precipitate-host lattice coherency for compositional determination of precipitates in Al-Mg-Si-Cu alloys," *Philosophical Magazine,* vol. 92, no. 31, pp. 3833 - 3856, 2012.

[25] C. D. Marioara, S. J. Andersen, T. N. Stene, H. Hasting, J. Walmsley, A. T. J. V. Helvoort and R. Holmestad, *Philosophical Magazine,* vol. 87, p. 3385, 2007.

[26] A. J. McAlister, “The Ag-Al (Silver - Aluminum) system,” *Bulletin of Alloy Phase Diagrams,* vol. 8, no. 6, pp. 526 - 533, 1987.

[27] F. J. H. Ehlers, S. Wenner, S. J. Andersen, C. D. Marioara, W. Lefebvre, C. B. Boothroyd and R. Holmestad, “Phase stabilization principle and precipitate-host lattice influences for Al-Mg-Si-Cu alloy precipitates,” *J Mater Sci,* vol. 49, pp. 6413 - 6426, 2014.

[28] E. A. Mørtsell, S. Wenner, P. Longo, S. J. Andersen, C. D. Marioara and R. Holmestad, “Elemental electron energy loss mapping of a precipitate in a multi-component aluminium alloy,” *Micron,* April 2016.

The Effects and Behaviour of Li and Cu Alloying Agents in Lean Al-Mg-Si Alloys

Submitted

Paper 5

The effects and behaviour of Li and Cu alloying agents in lean Al-Mg-Si alloys

Eva A. Mørtsell*[1], Calin D. Marioara[2], Sigmund J. Andersen[2], Inga G. Ringdalen[2], Jesper Friis[2], Sigurd Wenner[1], Jostein Røyset[3], Oddvin Reiso[3] and Randi Holmestad[1]

[1]Department of Physics, Norwegian University of Science and Technology (NTNU), 7491 Trondheim, Norway

[2]SINTEF Materials and Chemistry, N-7465 Trondheim, Norway

[3]Hydro Aluminum R&D Sunndal, N-6600 Sunndalsøra, Norway

*Corresponding author. E-mail address: eva.mortsell@ntnu.no

Abstract

We show how replacing a fraction of Mg with Li in a lean Al-Mg-Si alloy gives comparable strength and enhanced temperature stability. Replacing solute with smaller amounts of Cu and Li also improves thermal stability and nearly compensates the strength loss for longer ageing times. High angle annular dark field scanning transmission electron microscopy (HAADF-STEM) documented Li and Cu causing modest structural changes to the main hardening precipitate, *β"*. However, density functional theory calculations verified the observation from HAADF-STEM that Li preferentially occupies Mg3 sites in the *β"* structure.

Keywords: Al-Mg-Si, TEM, HAADF-STEM, DFT, Lithium, Copper

Introduction

The major alloying elements in the age hardenable aluminium 6xxx series are Mg and Si, in typical amounts of 1 - 2 at %. Alloys of this series are rolled or extruded into final shapes. Hardening occurs during a subsequent 'artificial' ageing (AA) step – a heat treatment performed at a temperature around 180 ºC. The precipitation sequence in ternary Al-Mg-Si alloys is as follows [1].

Supersaturated solid solution → atomic clusters → Guinier-Preston-zones (pre-*β"*) [2] [3] → *β"* [4] [5] → *β'* [6], *U1* [7], *U2* [8], *B'* [9] → *β*, Si (stable)

The major hardening agent is the monoclinic *β"* phase. Full coherency, small size and high number density are probably the most essential parameters behind its strengthening capabilities. In ternary alloys with Mg/Si ratios near unity, high-resolution transmission electron microscopy (HRTEM) images taken along $\langle 001 \rangle_{Al}$ orientation reveal short needles along the two normal $\langle 100 \rangle_{Al}$ directions in the plane. The cross-sections of these *β"* needles along the viewing direction appear monoclinic, with edges defined by cell parameters $\boldsymbol{a}_{\beta''} \parallel \langle 3\bar{2}0 \rangle_{Al}$ and $\boldsymbol{c}_{\beta''} \parallel \langle 130 \rangle_{Al}$ and the monoclinic angle 105.3º. Close-ups of the cross-section show that *β"* is essentially a stack of identical units (column groups) with eye-like appearance. One 'eye' consists of nine columns with roughly 4-fold ordering (a Si_4Mg_4 ring

around a central $Mg_{1-x}Al_x$ column, $0<x<1$) plus two less conspicuous satellite columns on each side (ideally Aluminium), see also Fig. 5 (c, d). The satellite sites were originally assumed to be Si (Si3 positions), but later work has shown they are flexible sites, especially at the interface, where elements like Cu may be adopted to reduce strain [10]. One unit cell has two such $Si_4Mg_{4-x}Al_{2+x}$ units at the (00z) and (½, 0, z+½) special positions in the unit cell. They may be regarded as molecular units of *β''* and were recently shown to come in three different stacking variations [11], sometimes mixed. The stacking variations occur particularly frequently with small additions of Ge, where Ge (partially) occupies some Si columns.

Increasing the amount of solute to improve strength creates a dilemma: extrudability becomes worse. Less solute can also lead to sacrifices regarding surface quality. It has been shown in previous work, that maintaining strength is possible when parts of the Mg-Si content is replaced by a lower amount of Ge [12]. The solid solubility of Li in aluminium is high. With nearly a quarter the weight of aluminium, Li also reduces alloy density somewhat [13]. Koshino et al. have shown how small additions of Li to Al-Mg-Si alloys increase the age-hardening response [14]. From the previous investigations it appears that Li can be incorporated in the precipitates, and it has been argued that it does not alter the precipitation sequence. If so, the *β''* phase should still be the main hardening precipitate for these alloys, although the precipitate size, numbers and strength potential may be expected to change. Earlier studies also report how Li diffuses quickly towards the surface of the alloy and significant amounts can be depleted into air. Depletion of Li from the material surface also occurs for Al-Li alloys if the surface oxide layer has been removed [15]. It has been suggested that Li atoms diffuse to the surface faster than being replaced by Al atoms (which must imply they leave vacancies in their wake), and that the created surplus leads to vacancy agglomeration [16].

Cu is a common trace element in Al-Mg-Si alloys, for example from recycling, but it is also added on purpose by industry because it improves the material strength. In amounts as low as 0.1 wt % Cu can cause inter-granular corrosion [17]. Consequently, in this study the level has been kept at 0.05 wt %. When it comes to precipitate phases, Cu can substitute Al and Si sites within the structures but will also occupy sites at the precipitate interfaces [26-27]. Above some threshold Cu will suppress formation of β", promoting other phases to form. The precipitation sequence in Cu added 6xxx alloys can be given as follows [18] [19] [20] [21] [22].

Supersaturated solid solution → atomic clusters → Guinier-Preston-zones (pre-*β''*) [2] [3] → *β''* [6], L, S, C, QP, QC → *β'*, Q' → Q

In this work, for a 6060 alloy we remove a fraction of the solute, Mg and Si, and replace it either fully (Mg atom for Li atom) or with a lower fraction of Cu or Li, alone or combined. We investigate the hardening response of the alloys as function of artificial ageing and compare with the reference alloys (the 6060 alloy and its leaner version). From TEM images and EELS thickness measurements, we obtain size and density statistics about the hardening precipitates in <001>Al orientations when the alloys are at, or just prior to peak hardness

conditions. Also, cross-sections from precipitates aligned in the viewing direction of the same conditions are investigated in more detail using high angle annular dark-field scanning TEM (HAADF-STEM), which is less affected by objective lens defocus and specimen thickness as compared to conventional HRTEM, hence consistently producing images of bright atomic columns against a dark background [23] [24]. Finally, density functional theory (DFT) is applied to investigate how the formation enthalpy changes when Li incorporates into β'', in the purpose of understanding important structural observations.

Experimental

Composition measurements (see Table 1) of the alloys were performed by inductively coupled plasma atomic emission spectroscopy.

The alloys were in the shape of cylindrical cast billets weighing 4 kg. They were homogenized for 3hours within 1-2 hours prior to extrusion, performed at a temperature of 575 °C followed by air-cooling to room temperature (RT). The billets were heated to about 540 °C before extrusion into solid cylinders of 2cm diameter.

Cylindrical samples in lengths of 1 cm, cut perpendicular to the extrusion direction were heat treated according to the illustration in Fig. 1. Each sample was solution heat treated (SHT) at 535 °C in an air circulating furnace for 5 minutes, where after it was quenched in water to RT immediately after removal from the furnace. Furthermore, the samples were naturally aged for 4 hours at RT before being artificially aged (AA) at 195 °C.

Table 1 Alloy composition, effective solute (S_{eff}) and solute reduction ΔS relative to RX0

Alloy	Si[a]	Mg	Cu	Li	Fe	Mn	S_{eff} [b]	ΔS[c] (- %)
RX0 wt%	0.45	0.37	–	–	0.20	0.03	0.77	–
RX0 at%	0.43	0.41	–	–	0.10	0.015	0.80	–
RX1 wt%	0.37	0.32	–	–	0.20	0.03	0.64	16.8
RX1 at%	0.36	0.36	–	–	0.10	0.015	0.66	16.7
RXL0 wt%	0.440	0.290	–	0.026	0.20	0.030	0.71	9.1
RXL0 at%	0.423	0.322	–	0.101	0.097	0.015	0.80	0.0
RXLC1 wt %	0.370	0.320	0.050	0.006	0.200	0.030	0.70	9.1
RXLC1 at %	0.356	0.356	0.021	0.023	0.097	0.015	0.71	11.3
RXL1 wt %	0.420	0.270	–	0.013	0.200	0.030	0.65	15.6
RXL1 at %	0.404	0.300	–	0.051	0.097	0.015	0.71	11.3

[a] Effective Si available for precipitation (Si*) is 0.05 wt % less the tabulated amount [25]. [b] Effective solute S_{eff} = Mg+Si*+Cu+Li. [c] Removed solute fraction as percentage of content in RX0 (AA6060 reference alloy). RX1 is the leaner reference. 'L' and 'C' signify Li and Cu, respectively.

Details of heat treatments and TEM sample preparation are described in [12], TEM specimens were made from samples subjected to AA for 4 hours (close to peak hardness). Thin slices cut perpendicular to the extrusion direction were mechanically polished using SiC

paper, to a thickness of approximately 100 μm. Disks of 3 mm diameter were stamped out from the foils and electrochemically thinned by a twin-jet Tenu-Pol 5 from Struers. The electrolyte consisted of 1 part nitric acid and two parts methanol, which was kept at approximately -25 °C by adding liquid nitrogen.

Behind the statistics of the precipitate microstructure presented in Table 2 are particle counts together with length and cross-section measurements extracted from TEM images, for this purpose acquired in a Philips CM30 instrument operated at 150 kV. The average thickness for each imaged area was estimated using parallel electron energy loss spectroscopy (PEELS). For a more complete description of the procedure leading to the statistics in Table 2, see [26]. In Table 2, the number densities and needle lengths are based on at least 1000 needles distributed over 8 – 10 imaged areas. The needle cross sections are averages from a minimum of 100 cross sections. The volume fractions are within 95 % confidence intervals. Although statistics generally originates from (the centre of) one grain from each alloy only, we inspected multiple grains to ensure that the microstructure was representative. For alloy RXL0, the images indicated strong local variations with a significant spread in needle sizes and number densities. Therefore, results in Table 2 from RXL0 are averages obtained from three different grains from three separate TEM specimens.

The HAADF-STEM images were acquired in a double corrected JEOL ARM200F, with 0.08 nm probe size and an inner HAADF collection angle of 50 mrad. Single images were acquired at 200 kV. Movies consisting of approximately 40 images were taken at 80 kV to correct drift and distortions by use of the Smart Align software [27]. Since 'Smart Align' uses a stack of images to do simple image translation, affine corrections and non-linear distortion corrections, these resulting images are much closer to the "real" imaged lattice with respect to atomic positions than corresponding single scans, and have a much higher signal-to-noise ratio. A stack of about 40 scans was used to create each 'Smart Align' image. A collection angle of 35 mrad was used for the 'Smart Align' images.

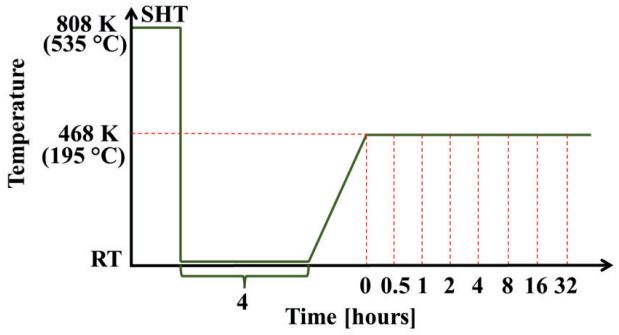

Fig. 1 Heat treatment overview. After quenching from solution temperature (535 °C), samples were held at RT for four hours before heated to the 195 °C artificial ageing temperature (at a rate 26 °C/hour). Vertical dotted lines indicate ageing times where water-quenching to RT completed the ageing.

For DFT calculations we used the Vienna ab initio simulation package (VASP) [28] [29]. The projector augmented wave method (PAW) within the PBE generalized gradient approximation was applied, with a plane wave energy cut-off of 400 eV. Gamma-centred *k*-points with maximal *k*-point distances of 0.25 $Å^{-1}$ in each direction were used for all the calculations. Methfessel-Paxton of 1st order was applied to relax the atomic positions to a maximum force of 0.001 eV/Å. For accurate energies, a separate calculation was performed based on the tetrahedron method with Blöchl correction for smearing, which is explained in detail by Ninive et al. in [30].

3 Results

3.1 Vickers hardness, TEM and precipitate statistics

Fig. 2 gives the age-hardening response of all alloys including the two references, where Vickers hardness (HV) is presented as a function of ageing time. The HV curves of RX0 (dense reference; originally used in industry) and RX1 (lean reference; reduced solute, but no additions) originate from an earlier study [12], but are presented here for comparison. The lean reference (RX1) ranges worst, the curve is well below all other alloys. RXL0 is a variation of RX0 with a quarter of Mg atoms substituted by Li, therefore containing the same amount of solute in atomic concentration. Table 2 shows the solute weighs 9.1 % less. The lithium addition in RXL0 compensates for the strength loss of the lean reference, reaching nearly identical peak hardness as the dense reference RX0, and even surpassing it for longer ageing times. The two other lithium added alloys, RXL1 and RXLC1, with slightly more solute than the lean reference, lay well above its curve. They show intermediate hardness values during the entire artificial ageing heat treatment. For longer ageing times RXLC1 is the more stable of the two alloys.

The four TEM micrographs given in Fig. 3 show typical morphology and distribution of the precipitates in the alloys. For RXL0, while the precipitate distribution generally is similar in all observable grains in the same specimens, in one specimen [Fig. 3 (a)] the precipitates were much coarser [compare with Fig. 3(b)]. As exemplified by the horizontal needle above the scale annotation in Fig. 3(a), a high amount of the coarser precipitates in RXL0 had wavy contrast lines in this specimen.

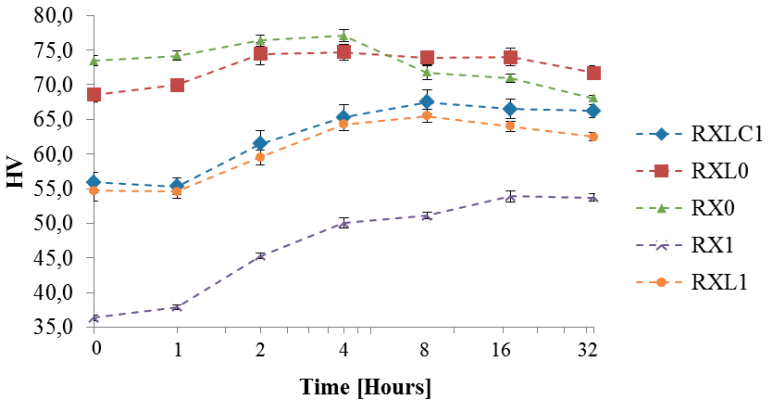

Fig. 2 Vickers hardness plotted as a function of artificial ageing time at 195 °C. Note that the x-axis has a logarithmic scale. RX0 (top) and RX1 (bottom) signify the dense and lean reference alloys, respectively. Letters 'L' and 'C' indicate lithium and/or copper in an alloy (see Table 1).

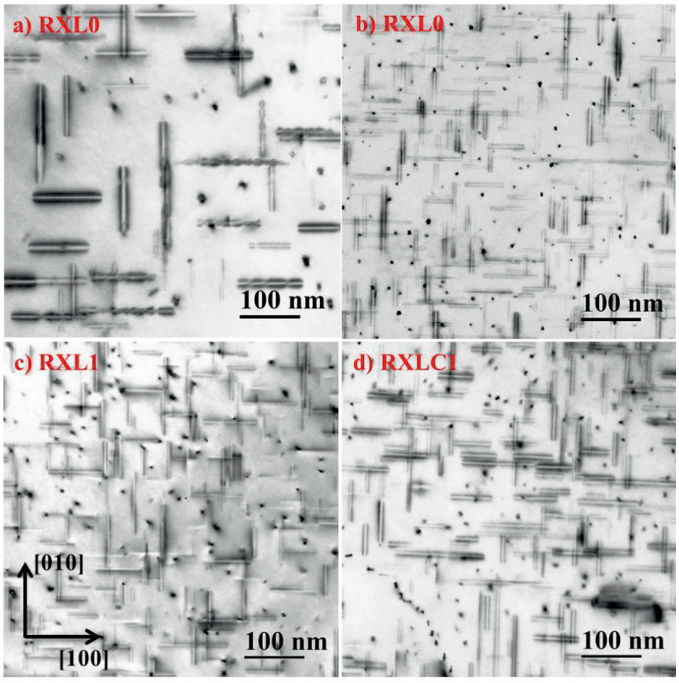

Fig. 3 TEM bright field images from each of the three Li-containing alloys at near peak hardness condition (4h AA at 195 °C). (a) RXL0, TEM specimen 1, (b) RXL0, TEM specimen 2 (c) RXL1 and (d) RXLC1.All images are taken along the <001>Al zone axis. The double contrast lines in the micrographs are needles along the two [100]Al directions in the viewing plane. The crystal directions are indicated by arrows in (c).

Intriguingly, Table 2 shows that the high hardness for alloy RXL0 corresponds to lowest precipitate number density and volume fraction. The precipitates in this alloy are largest, being on average longest and with highest cross-section area.

Table 2 Precipitate statistics obtained after 4h AA at 195 ºC. Average precipitate cross sections, needle lengths, number densities and volume fractions with corresponding errors estimated from TEM micrographs. RX0 and RX1 are included for comparison [12].

Alloy	Cross Section [nm^2]	Needle Length [nm]	Number Density [#/µm^3]	Volume Fraction [%]	HV
RX0	24,0 ± 2,0	95 ± 5	3200 ± 400	{0.64, 0.80}	77
RXL0	17,5 ± 1,0	78 ± 3	3400 ± 400	{0.36, 0.43}	75
RXLC1	16,9 ± 1,6	61 ± 5	6100 ± 700	{0.54, 0,71}	65
RXL1	13,1 ± 0,7	56 ± 3	8000 ± 950	{0.53, 0.64}	65
RX1	42 ± 4	243 ± 73	170 ± 50	{0.12, 0.19}	50

3.2 HAADF-STEM and DFT

Fig. 4 shows HAADF-STEM images recorded in $<100>_{Al}$ orientations showing cross-sections of precipitates representative of the various alloys near the hardness maximum. The observed cross-sections showed nearly just *β"* structure, which means *β"* is the foremost hardening phase in all alloys.

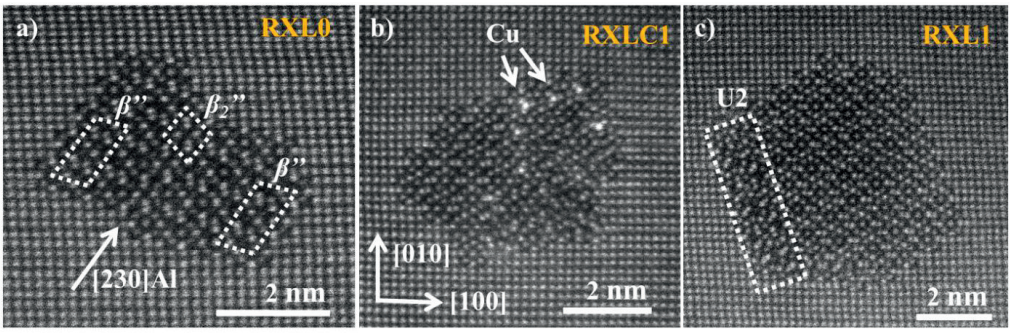

Fig. 4 Unprocessed HAADF-STEM images from **(a)** RXL0, the arrow points out a stacking fault along $a_{\beta''} \parallel \langle 230 \rangle_{Al}$. The dashed lines indicate *β"*and *β2"* unit cells, **(b)** RXLC1, where bright Cu columns can be observed. Two Cu columns are pointed out by arrows. **(c)** RXL1, the dashed lines indicate a U2 region. The crystal directions, as indicated by arrows in (b), are the same in all three images.

Among features frequently observed in precipitate cross-sections of RXL0, was a stacking fault running across the width, along the direction $a_{\beta''} \parallel \langle 230 \rangle_{Al}$. Fig. 4 (a) shows one example. This stacking fault generates units of *β2"* across the cross section. In general, a high

occurrence of β_2" has been found in the Li-containing alloys. Based on the results presented in this section, models of the β"-eyes are given in Fig. 5, with symbolic representation of elements given in Table 2. A significant amount of the Mg3 sites had a comparatively lower intensity than Mg1 and Mg2 sites in the HAADF-STEM images. Except for the Cu-containing alloy RXLC1, Fig. 4(b), not many precipitates were disordered, and other phases than β" were practically non-present, although interfaces of β" often could contain small regions of the U2 structure, see left side of the precipitate in Fig. 4 (c).

In RXLC1, a common triangular column group symmetry associated with Cu columns existed in several precipitate cross sections, exhibiting a high intensity in the HAADF-STEM images. Most cross sections contained a combination of fragments from both β" and Cu-containing phases like *Q'*, C-plate and β'_{Cu} [17]. Several precipitate cross sections contained only a few Cu columns, with the remainder being β". Among the observed cross sections, those significantly smaller than the average presented in Table 2 incorporated no Cu columns at all.

Three representative examples from the 'Smart Align' images are presented in Figs. 5 and 6, with atomic overlays. The original β" eye is shown in Fig. 5 (c) while the new model for Li-containing alloys is given in Fig. 5 (d). The symbolic representation of elements in Figs. 5 and 6 can be found in Table 3.

Table 3 Symbolic representation of elements in Figs. 5 and 6.

Elements / Height	Al	Si	Mg	Li
z = 0.000 nm	○	○	○	○
z = 0.203 nm	●	●	●	●

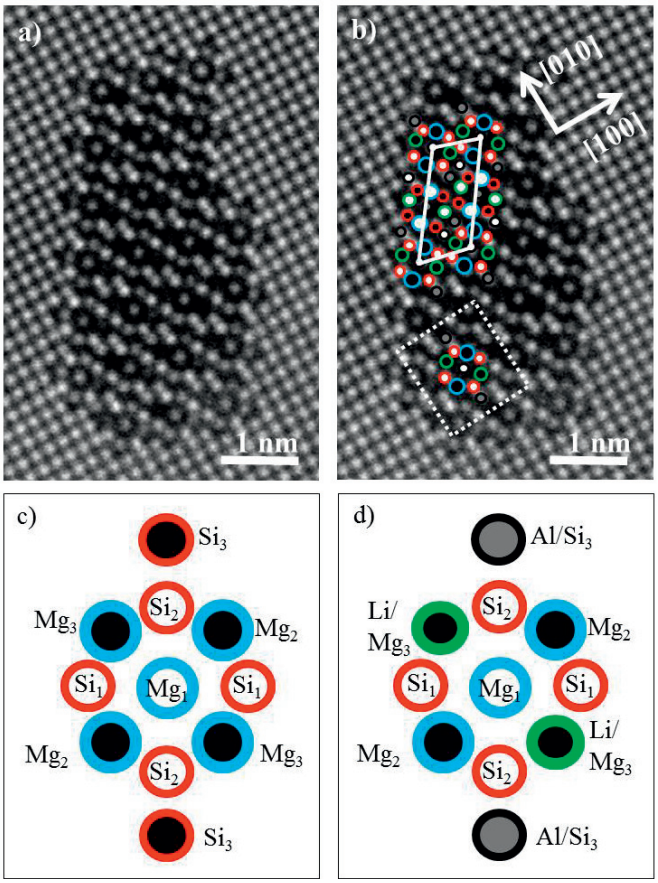

Fig. 5 (a) 'Smart Aligned' image of a *β"* precipitate cross section in RXL0. **(b)** Partial atomic overlay on the precipitate in (a), where a unit cell of *β"* is indicated by a white, solid lin parallelogram and a single *β"* – eye is indicated inside the white, dashed square. **(c)** The *β"*-eye as described in previous studies [30], **(d)** *β"* – eye containing Li at Mg3 sites, directly comparable to the eyes of same heights in the *β"* – unit cell. The elemental composition of the eye is based on intensity variations in HAADF-STEM 'Smart Aligned' images and DFT simulations. See Table 2 for symbolic representation of elements and heights.

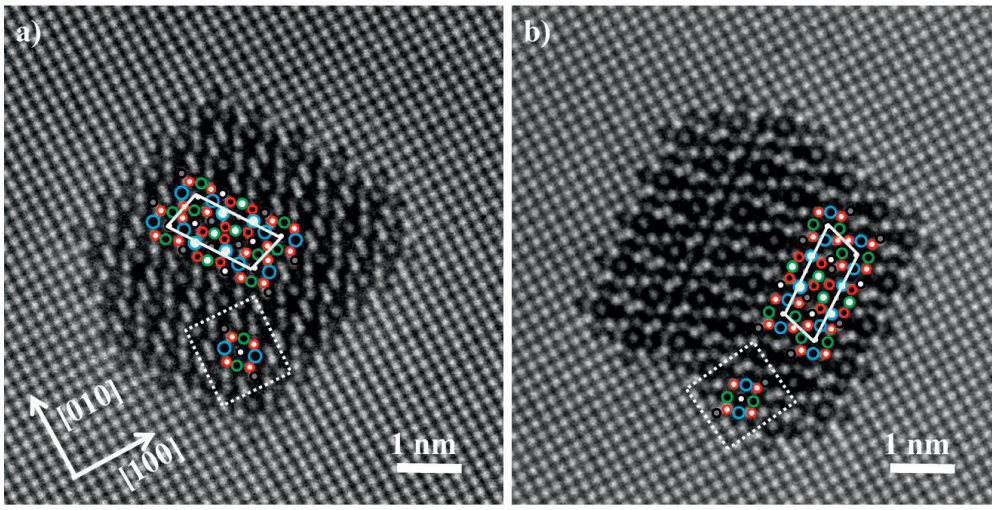

Fig. 6 'Smart Align' HAADF-STEM images of two *β''* precipitate cross section in RXL0, showing a different orientation of the unit cells, as compared to Fig. 5 (a), marked by solid white lines. Single *β''* – eyes are also indicated inside the white dashed lines. Both orientations show less intensity at Mg3 sites, suggesting more Li occupancy. In (b) a stacking fault along $a_{\beta''} \parallel \langle 230 \rangle_{Al}$ is also present. See Table 2 for the symbolic representation of elements.

Based on the findings presented above, DFT calculations of the *β''* (bulk) structure for various Li substitutions of the Mg sites was performed. The results are shown in Fig. 7. The curves show that a relatively high Li-occupancy at the Mg sites is energetically favourable. Substitution of Mg up to 60 % Li, i.e. to a formula $Mg_2Li_3Si_4Al_2$ seems to be the most favourable from Fig. 5, if the initial structure is $Mg_5Si_4Al_2$.

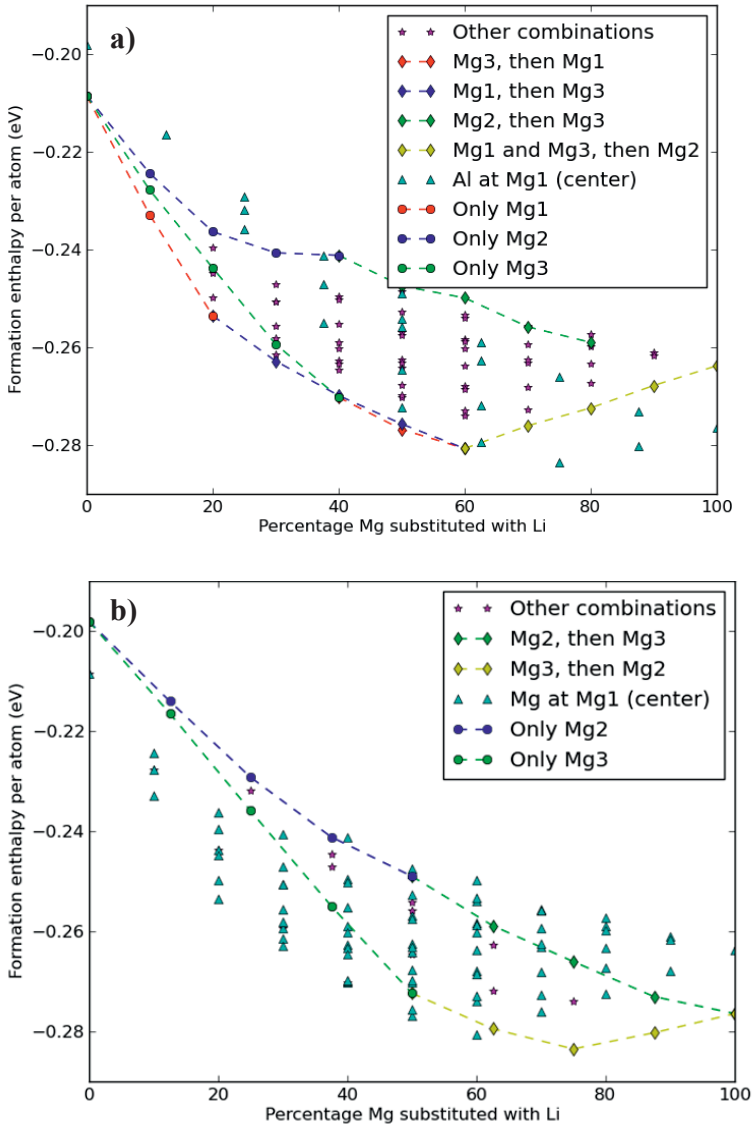

Fig. 7 DFT calculations showing the formation enthalpy per atom (eV) as a function of Li substituting Mg at different sites in the *β"* eye. **(a)** Curves based on substitutions having $Mg_5Si_4Al_2$ as the initial structure (*β"* with Al at Si3 sites). The blue pyramids correspond to the calculations presented in (b). **(b)** Curves based on substitutions having $Mg_4Si_4Al_3$ as the initial structure (*β"* with Al at Mg1 and Si3 sites). The blue pyramids correspond to the calculations presented in (a). The formation enthalpy per atom is lowest for Mg at Mg1 sites up to about 60 % Mg substituted by Li.

4 Discussion

4.1 Hardness, TEM and statistics

RXL0 has the largest and most coarsely distributed precipitates of the three Li-added alloys, but also the highest hardness (see Table 2). According to previous investigations [12], the precipitate size correlating with maximum strength should fall between that of RXL0 and the two other alloys, RXL1 and RXLC1. One possible reason for this discrepancy is that RXL0 showed a large variation in the precipitate sizes and densities from one TEM specimen to another, indicating the acquired statistics is not sufficiently accurate for interpreting macroscopic properties. Such variation could arise if TEM specimens are taken from varying distances to the surface of the extruded rods. However, here it was taken care to avoid preparing TEM specimens close to the surface. A better explanation lies with the high diffusivity of Li: Li is a fast diffuser towards the surface of the material during heat treatments in air, which means depletion may reach far into the material [16] [31]. This would in turn lead to lower concentration of Li in some TEM specimens, causing an excess of Si for precipitation and more Si rich phases.

Another reason for the precipitate size and strength results could be a change in hardening mechanisms. Precipitates contribute to strength, since dislocations must pass them either by looping or cutting [32]. If the size distribution of the precipitate needles in RXL0 has reached a critical size, strength decreases both with larger and smaller precipitate needle sizes. A critical size will exist above which the strengthening mode changes to looping. Assuming similar interface energies for the precipitates in all three Li-added alloys (which is reasonable since the hardening phase is the same), we expect RXL0 to have a precipitate microstructure slightly larger than the critical size. Thus, such size should have a cross-section of about 15 nm^2 and a length of 70 nm, according to Table 2. However, according to previous studies the critical size of the related β' phase should be much larger [33], which suggests we need to investigate the above mentioned mechanisms further.

RXLC1 has better thermal stability than the similar, Cu-free, RXL1. Adding Cu to the alloy creates more disorder in the precipitate microstructure, which is evident for a majority of the observed precipitate cross sections in HAADF-STEM. The smaller precipitate cross sections, with respect to the size distribution, incorporate no Cu. The larger cross sections do however contain Cu columns. This could be due to precipitates containing Cu being more coherent, and has a higher probability of growing to larger sizes. Another possibility is that Cu diffuses more slowly than Si and Mg and does not take part in the precipitation and growth until after small needles of Si and Mg has already managed to form. For long ageing times, the reference alloy over-ages and becomes softer, while RXLC1 is comparatively more stable. As a consequence, the difference in strength between RXLC1 and the (stronger) dense reference RX0 becomes practically insignificant with time.

Earlier results have shown that alloys containing a combination of Ge and Cu in small amounts can have strong refining effects on precipitates [12]. The precipitate number

densities in such alloys reach much higher values than alloy RX0, and have higher accompanying hardness, as less coherent needles act as more effective dislocation impediments. If both strengthening modes are active, the precipitate distribution, size and type have a well-tuned balance for optimising material hardness. We plan further investigations to pinpoint the reason behind the local variations in the precipitate sizes and numbers, and the correlation between coarser precipitates and high hardness, for the Li substitution of Mg.

4.2 HAADF-STEM and DFT investigations

Close inspection of Mg columns in Figs. 5 and 6 shows that nearly all Mg3 sites not close to an interface have significantly lower intensity than Mg1 and Mg2 sites in the same eye. In Al-Mg-Si alloys with no other solute additions, intensity in HAADF-STEM changes much less between different sites [30]. Consequently, the differences here are likely to stem from Li occupation, predominantly in Mg3 columns.

From Fig. 7 we note that the lowest formation enthalpy configuration assuming an initial Mg5Si4Al2 composition has 60 % Li substitution of the Mg sites, causing the Mg1 and Mg3 sites to fill up, while no substitution occurs at the Mg2 sites. Considering the low at % of Li added to the alloys, the Li occupancy is more likely to be below 20 % in Fig. 7. Filling Mg1 sites first and then Mg3 and vice versa does not seem to matter. Both sequences result in the same low formation enthalpy per atom. Mg1 sites have the largest "energetic gain" per atom and the Mg2 sites have the lowest gain per atom. However, Mg3 columns have twice as many atoms as Mg1 for each unit cell, which is one of the reasons why the Mg3 site gains more than Mg1 in Fig. 7.

From the experimental work, see Figs. 5 and 6, the low intensity at Mg3 sites appears systematic across the entire precipitate cross sections. However, less Li appear in Mg3 columns when the 'eyes' are adjacent to the Al-lattice or the commonly occurring stacking faults along$\langle 230 \rangle_{Al}$. The same effects are observed for a majority of the β'' precipitate cross sections, suggesting that Li filling of Mg3 sites happens consistently for Li-added Al-Mg-Si alloys. One of the differences between Mg2 and Mg3 sites when considering the β'' structure is that the Mg2 sites have slightly more symmetric surroundings. Mg3 sites have less space in their near vicinity than Mg2 sites, which suggests it is more favourable to fill these sites with Li, as Li has a smaller atomic radius than Mg [34]. That is, the need to create a column taking up less volume might be higher at Mg3 sites.

The formation enthalpy per atom is significantly lowered when Mg1 sites are filled with Mg and not Al. It is possible that Li favours the "symmetric surroundings" at Mg1, because of the near-cubic symmetry with 12 nearest neighbours. The main conclusion is that it is most beneficial for Li to go to Mg3 and Mg1 sites first, while Mg2 sites are the last sites per eye to be replaced with Li. It is interesting that Mg1 sites are not exhibiting a darker contrast in HAADF-STEM considering the DFT results. We are planning quantitative STEM investigations to determine the Li occupation at different Mg sites in β''.

5 Conclusions

The general objective in this work has been to investigate if strength in a 6060 alloy upon removal of a fraction of the solute Si and Mg can be maintained, either by less heavy elements or by adding back lower amounts of other solute. Replacing about a quarter of the Mg solute with Li (0.1 at %) showed Li entered the main strengthening phase *β''* without causing loss of strength. In fact, a slightly more temperature resistant alloy resulted. Replacement of a quarter of both Mg and Si with smaller and equal amounts of Li and Cu, whereby the weight fraction of solute was reduced by 9 % compared to its original value, resulted in a slight loss in strength. However, because of higher thermal stability, the loss approach zero after longer ageing times. Precipitate statistics acquired by conventional TEM enabled quantitative comparisons between the precipitate microstructures at peak hardness conditions. HAADF-STEM enabled comparison of the atomic structures. The alloy with 0.1 at % Li-replacement showed a microstructure comparable with the reference 6060 alloy. However, unexpected variations between TEM specimens were found, which are suspected to be linked to rapid Li depletion during heat treatment in air. HAADF-STEM showed that practically all the precipitate needles were of *β''* type, with Li occupying a significant amount of the Mg3 sites of the structure. This result was fully supported by density functional theory calculations.

Acknowledgements

The project has been supported through the BIA RolEx project, no. 219371 financed by Hydro Aluminium and the Research Council of Norway. The STEM work was carried out on the NORTEM JEOL ARM200F, TEM Gemini Centre, NTNU, Norway. The authors would also like to thank Birgitte Karlsen, SINTEF Materials and Chemistry for performing heat treatments and hardness measurements of the alloys.

Bibliography

[1] C. D. Marioara, H. Nordmark, S. J. Andersen and R. Holmestad, *J. Mater. Sci.,* vol. 41, pp. 471 - 478, 2006.

[2] G. A. Edwards, K. Stiller, G. L. Dunlop og M. J. Couper, *Acta Mater.,* vol. 46, pp. 3893 - 3904, 1998.

[3] C. D. Marioara, S. J. Andersen, J. Jansen og H. W. Zandbergen, *Acta Mater.,* vol. 49, pp. 321 - 328, 2001.

[4] S. J. Andersen, H. W. Zandbergen, J. Jansen, C. Træholt, U. Tundal og O. Reiso, *Acta Mater.,* vol. 46, pp. 3283 - 3298, 1998.

[5] H. S. Hasting, A. G. Frøseth, S. J. Andersen, R. Vissers, J. C. Walmsley, C. D. Marioara, F. Danoix, W. Lefebvre og R. Holmestad, *J. Appl. Phys.,* vol. 106, 2009.

[6] R. Vissers, M. A. v. Huis, J. Jansen og C. D. M. S. J. A. H. W. Zandbergen, *Acta Mater. ,* vol. 55, pp. 3815 - 3823, 2007.

[7] S. J. Andersen, C. D. Marioara, R. Vissers, A. Frøseth og H. W. Zandbergen, *Mater. Sci. Eng. A,* vol. 444, pp. 157 - 169, 2007.

[8] S. J. Andersen, C. D. Marioara, A. Frøseth, R. Vissers og H. W. Zandbergen, *Mater. Sci. Eng. A,* vol. 390, pp. 127 - 138, 2005.

[9] R. Vissers, C. D. Marioara, S. J. Andersen og R. Holmestad, *Aluminium Alloys,* vol. 2, pp. 1263 - 1269, 2008.

[10] T. Saito, F. J. H. Ehlers, W. Lefebvre, D. Hernandez-Maldonado, R. Bjørge, C. D. Marioara, S. J. Andersen, E. A. Mørtsell og R. Holmestad, «Cu atoms suppress misfit dislocations at the β″/Al interface in Al–Mg–Si alloys,» *Scripta Materialia,* vol. 110, nr. 1, pp. 6-9, 2016.

[11] E. A. Mørtsell, S. J. Andersen, J. Friis, C. D. Marioara og R. Holmestad, «Atomistic details of precipitates in lean Al-Mg-Si alloys with trace additions of Ag and Ge studied by HAADF-STEM and DFT,» *In progress,* 2016.

[12] E. A. Mørtsell, C. D. Marioara, S. J. Andersen, J. Røyset, O. Reiso og R. Holmestad, «Effects of Germanium, Copper, and Silver Substitutions on Hardness and Microstructure in Lean Al-Mg-Si Alloys,» *Metallurgical and Materials Transactions A,* vol. 46, nr. 9, pp. 4369 - 4379, 2015.

[13] I. Polmear, Light Alloys, From Traditional Alloys to Nanocrystals, Oxford UK1: Elsevier, 2006.

[14] Y. Koshino, M. Kozuka, S. Hirosawa og Y. Aruga, «Comparative and complementary characterization of precipitate microstructures in Al-Mg-Si(-Li) alloys by transmission electron microscopy, energy dispersive X-ray spectroscopy and atom probe tomography,» *Journal of Alloys and Compounds,* vol. 622, pp. 765 - 770, 2015.

[15] A. Sagara og K. Kamada, «Measurements of evaporation rate of Lithium from Al-Li alloy by depth profiling with an ion beam,» *Nuclear Instruments and Methods in Physics Research B,* vol. 44, pp. 373 - 376, 1990.

[16] H. L. Jr og P. Coleman, «Vacancy clustering in quenched Al-Li solid solution alloys studied by Doppler broadening spectroscopy,» *J. Phys.: Condensed Matter,* vol. 10, pp. 10423 - 10428, 1998.

[17] T. Saito, C. D. Marioara, S. J. Andersen, W. Lefebvre og R. Holmestad, «Aberration-corrected HAADF-STEM investigations of precipitate structures in Al-Mg-Si alloys with low Cu additions,» *Philosophical Magazine,* vol. 94, nr. 5, pp. 520 - 531, 2015.

[18] C. D. Marioara, S. J. Andersen, T. N. Stene, H. Hasting, J. Walmsley, A. T. J. V. Helvoort og R. Holmestad, *Philosophical Magazine,* vol. 87, p. 3385, 2007.

[19] D. J. Chakrabarti og D. E. Laughlin, *Prog. Mater. Sci.,* vol. 49, p. 389, 2004.

[20] C. Cayron, L. Sagalowicz, O. Beffort og P. A. Buffat, *Philos. Mag. A,* vol. 79, p. 2833, 1999.

[21] K. Matsuda, Y. Uetani, T. Sato og S. Ikeno, *Metall. Mater. Trans. A,* vol. 32, p. 1293, 2001.

[22] L. Arnberg og B. Aurivillius, *Acta Chem Scand A,* vol. 34, p. 1, 1980.

[23] T. Yamazaki, M. Kawasaki, K. Watanabe, I. Hashimoto og M. Shiojiri, *Ultramicroscopy,* vol. 92, p. 181, 2002.

[24] P. D. Nellist og S. J. Pennycook, *Ultramicroscopy,* vol. 78, p. 111, 1999.

[25] U. Tundal, O.Reiso, E. Hoff, R. Dickson og C. Devadas, i *Proc. 10th International Aluminum Extrusion Technology Seminar*, Miami, 2012.

[26] C. D. Marioara, S. J. Andersen, H. W. Zandbergen og R. Holmestad, *Metall. Mat. Trans. A,* vol. 36, pp. 691 - 702, 2005.

[27] L. Jones, H. Yang, T. J. Pennycook, M. S. J. Marshall, S. V. Aert, N. D. Browning, M. R. Castell og P. D. Nellist, «Smart Align - a new tool for robust non-rigid registration of scanning microscope data,» *Advanced Structural and Chemical Imaging,* vol. 1, 2015.

[28] P. Hohenberg og W. Kohn, «Inhomogeneous Electron Gas,» *Phys. Rev.,* vol. 136, pp. B864 - B871, 1964.

[29] K. W. og S. L. J., «Self-Consistent Equations Including Exchange and Correlation Effects,» *Phys. Rev.,* vol. 140, pp. A1133 - A1138, 1965.

[30] P. H. Ninive, A. Strandlie, S. Gulbrandsen-Dahl, W. Lefebvre, C. D. Marioara, S. J. Andersen, J. Friis, R. Holmestad og O. M. Løvvik, «Detailed atomistic insight itno the beta" phase in Al-Mg-Si alloys,» *Acta Materialia,* vol. 69, pp. 126 - 134, 2014.

[31] T. Schmidt, S. Heun, J. Slezak, J. Diaz og K. C. Prince, «SPELEEM: Combining LEEM and Spectroscopic Imaging,» *Surface Review and Letters,* vol. 5, nr. 6, pp. 1287 - 1296, 1998.

[32] J. D. Verhoeven, Fundamentals of Physical Metallurgy, London: John Wiley & Sons, 1975.

[33] K. Teichmann, C. D. Marioara, S. J. Andersen og K. Marthinsen, «TEM study of β′ precipitate interaction mechanisms with dislocations and β′ interfaces with the aluminium matrix in Al–Mg–Si alloys,» *Materials Characterization,* vol. 75, pp. 1 - 7, 2013.

[34] C. Wolverton, *Acta Mater. ,* vol. 55, pp. 5867 - 5872, 2007.

The Effect of 1 % Plastic Deformation and Elastic Strain on a 6060 Aluminium Alloy during Natural and Artificial Ageing

In progress

Paper 6

The Effect of 1 % Plastic Deformation and Elastic Strain on a 6060 Aluminium Alloy during Natural and Artificial Ageing

Eva A. Mørtsell*[1], Ida Westermann[2], Calin D. Marioara[2], Ketill O. Pedersen[2], Sigmund J. Andersen[2], Jostein Røyset[3] and Randi Holmestad[1]

[1]Department of Physics, Norwegian University of Science and Technology (NTNU), 7491 Trondheim, Norway

[2]SINTEF Materials and Chemistry, N-7465 Trondheim, Norway

[3]Hydro Aluminium R&D Sunndal, N-6600 Sunndalsøra, Norway

*Corresponding author. E-mail address: eva.mortsell@ntnu.no

Keywords: Al-Mg-Si alloy, transmission electron microscopy, elastic straining, plastic deformation, precipitation

Abstract

Effects of elastic strain on a 6060 Al-Mg-Si alloy during natural and artificial ageing or 1 % plastic deformation during natural ageing have been investigated. The elastic strain was kept at 50 % of the material yield strength. When applied at the beginning of natural ageing, elastic strain leads to an increase in tensile strength after artificial ageing, as compared to the unstrained material. By quantitative investigation of precipitate microstructure by transmission electron microscopy it was found an increased number density of finer precipitates in this condition. However, elastic strain does not seem to affect the precipitation when applied at other stages of the heat treatment. By comparison, for all heat treatment combinations, 1 % plastic deformation leads to increased hardness and tensile strength after artificial ageing due to introduction of dislocations. The highest tensile strength was measured for materials subjected to both elastic strain and plastic deformation combined.

1 Introduction

The development of aluminium alloys, and in particular that of 6xxx Al-Mg-Si alloys used for extrusion has become increasingly specialised. Such specialisation has resulted in materials which are competitive within the different standards of Europe, Asia and the US. It is possible to tailor material properties and extrudability based on improved understanding and control of alloy composition, thermo-mechanical processing and precipitate formation.

The main characteristic of Al-Mg-Si (-Cu) alloys is their ability to age harden. This characteristic is defined by a large increase in strength due to the formation of metastable, semi-coherent, nano-sized precipitates in the Al matrix as a consequence of artificial aging (AA) at temperatures usually between 150 °C to 200 °C [1, 2]. For a given alloy composition, combination of aging temperatures and holding times, different precipitate microstructures occur. The microstructures can be characterised by precipitate number density, size distribution, volume fraction and precipitate type. Each precipitate type has a specific crystal structure, composition, and characteristic interface with the Al matrix and may be optimised for certain alloy compositions and thermo-mechanical treatments. Precipitates influence the

overall ability of the Al matrix to obstruct dislocation movement, which is of great importance to macroscopic properties, like strength and ductility.

The final steps of a conventional heat treatment involve a solution heat treatment (SHT) at a high temperature above the solvus line of the system, a rapid cooling to room temperature (RT) and storage at RT (i.e. natural ageing, NA), followed by AA. The purpose of SHT is to dissolve the (Mg, Si) particles of the alloy so that the Mg and Si atoms from these particles are substituting positions in the Al lattice. In the extrusion process of lean Al-Mg-Si alloys, it is the extrusion process itself that serves as SHT, since the temperature of the material is brought well above the solvus temperature of Mg and Si. If the material is cooled rapidly, Mg and Si become supersaturated in solute, and unstable. With the help of simultaneously quenched-in supersaturation of vacancies, the solute atoms obtain sufficient mobility already at RT in order to form atomic clusters [3]. Increased AA temperature causes the microstructure to evolve and precipitate types change from coherent matrix-like to semicoherent and finally to incoherent, equilibrium phases. The transition of precipitate types is generally described by a precipitation sequence, which for the Al-Mg-Si system can be written as:

SSSS → atomic clusters [1, 3, 4] → GP-zones (pre - β'') [5] → β'' [6, 7] → β' [8], *U1* [9], *U2* [10], B' [11] → β, *Si* (equilibrium)

where SSSS is super saturated solid solution and GP-zones is Guinier-Preston zones.

The precipitate types regarded as most beneficial for material strength are GP-zones and β" [1, 2]. The post-β'' phases β', *U1*, *U2* and B' form upon over-aging. They give coarse microstructures characterised by low number densities of large precipitates, associated with a loss in strength [2, 12]. *U1*, *U2*, and B' are also known as types A, B and C respectively [13]. Previous work has found evidence of two types of atomic clusters, with ability to either prevent or promote precipitate nucleation during subsequent aging [3]. It has been shown that a storage at RT is detrimental for the formation of hardening precipitates in the case of dense alloys (with Mg + Si solute levels above 1 at %), while it is beneficial in the case of lean alloys [1, 14, 15]. It has been found that the promoting clusters form in denser alloys by performing a prebake at low temperatures (70 - 120 °C) prior to AA [16, 17].

All the metastable precipitates in the Al-Mg-Si (-Cu) system have one main coherency direction, parallel to the <100> Al directions. As a consequence, the precipitates assume the shape of needles, rods or laths elongated in one of the three directions. Therefore, all transmission electron microscopy (TEM) images used in this work were taken with the grains oriented along <100> Al directions, where approximately 1/3 of the needles can be observed in cross-section and 2/3 perpendicular to their lengths.

A dramatic change in precipitation has been observed to take place during AA in alloys which have been deformed during NA, or if AA and deformation are performed simultaneously [18, 19], relative to non-deformed alloys. Instead of homogeneous nucleation, in these cases precipitation occurs preferentially at the introduced dislocations leading to very inhomogeneous microstructures. Since dislocations are known to provide fast diffusion paths for the solute atoms, precipitation and growth are enhanced and peak hardness will be reached sooner. Accelerated kinetics shifts the precipitation sequence to the left, causing a

post-β'' type microstructure to nucleate sooner, that is, microstructure associated with overaging of the material. Overall, the strength during AA of the deformed material can be higher even if the net contribution from the precipitates is lower, because of strength induced by the dislocations themselves.

Changes in precipitate microstructure and mechanical properties in [18, 19] were well documented for a relatively high deformation level of 10 %. However, studying lower deformation levels is of utmost relevance. In the extrusion plant, the extruded profiles are straightened by stretching to plastic deformation in the range 0.5 – 1 % prior to age hardening. Industrial experience shows that such deformation has a measurable effect on the precipitation kinetics during AA.

In recent years, the knowledge of nucleation of precipitates in Al-Mg-Si alloy has been greatly enhanced, and it is clear that minute changes in alloy composition and process conditions may influence cluster formation and formation of the various precipitate types. Thus, it is of interest to investigate whether elastic strain, which will slightly alter the spacing between atoms in the lattice of the Al matrix, may have any detectable effect on the precipitation when applied either at the clustering stage (during NA) or at the early stage of AA.

In this work a lean 6060 alloy subjected to different combinations of elastic strain and 1 % plastic deformation during NA or AA at 160 °C has been investigated and compared to a non-deformed reference alloy. The hardness and yield strength were measured and discussed in connection to the precipitate microstructure investigated by TEM. Accordingly, the paper contains four parts: the investigation of the effect of plastic deformation combined with elastic strain, the effects of elastic strain alone, the precipitate microstructure investigated by TEM, and finally a discussion part.

2 Experimental and results

The alloy in this study was provided by Hydro Aluminium, Norway, in the shape of extruded profiles with a rectangular cross section with dimensions 5 x 40 mm^2. The profiles were extruded from ∅ 95 mm extrusion billets at an 800 ton laboratory press at SINTEF, Trondheim. The billets were heated to 540 °C in order to dissolve all (Mg, Si) - particles, then rapidly cooled to 500 °C just prior to extrusion. The extruded profiles were quenched into water just after the die exit in order to eliminate formation of new (Mg, Si) - particles. By this procedure, the required solution heat treatment is limited to 5 min at 500 °C and the possibility of grain growth during SHT of the extruded profiles is minimised. The chemical composition of the alloy used in all experiments is given in Table 1. The extruded profiles have a recrystallized grain structure, with an average grain size of approximately 100 μm.

Table 1: Chemical composition of the alloy in wt %.

Mg	Si	Fe	Mn	Al
0.37	0.41	0.04	0.05	Bal.

Tensile test samples were machined from the extruded profiles into two different geometries referred to in Fig. 1 as “large” (a) and “standard” (b), both with a thickness of 3 mm. To avoid influence on hardness measurements from possible surface layers of different grain structures, the samples were ground from 5 mm to 3 mm. Because TEM specimens had to be made with their normal parallel to the extrusion direction, the larger sample thickness was more convenient for TEM specimen preparation. Additional standard tensile test samples for TEM specimens were therefore made with the same geometry as in Fig. 1 (b), but with full thickness of 5 mm. A detailed explanation of the thermomechanical treatment and sample preparation is given in sections 2.1 and 2.2.

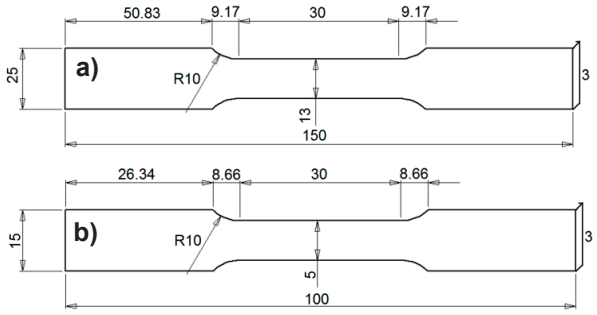

Fig. 1: Sketch of tensile test sample geometries used in the experiments: (a) large tensile test samples, (b) standard tensile test samples. All numbers are given in mm. The sketches are not to scale.

2.1 Influence of plastic deformation and elastic strain on subsequent age hardening

Fig. 2 shows the different thermo-mechanical processes used to investigate the influence of plastic deformation and elastic strain applied at different stages during heat treatment. In all cases, the SHT was 5 minutes at 500 °C in a salt bath, followed by water quench (W in Fig. 2) to RT. The samples were naturally aged for 24 h and artificially aged for 26 h at 160 °C in an oil bath. The heat treatment described in Fig. 2 (a) will be referred to as the reference sample, with no elastic strain or plastic deformation introduced. The reference samples were cut in lengths of 20 mm, perpendicular to the extrusion direction. In Fig. 2 (b) samples were subjected to elastic strain for 1 h immediately after quenching from SHT, while in Fig. 2 (c) samples were subjected to 1 % plastic deformation after quenching from SHT. As previously mentioned, plastic deformation to the equivalent of 0.5 – 1 % engineering strain is commonly used to straighten extruded profiles before AA. Combinations of plastic deformation and elastic strain are represented in Fig. 2 (d) and (e), where 1 % plastic deformation was introduced immediately after quenching from SHT, followed either directly by elastic strain and 24 h NA or by 24 h NA prior to elastic strain. The nominal strain rate of the plastically deformed samples was 10^{-2} s^{-1}, using a 25 mm extensometer.

The yield strength prior to elastic straining was determined first, as elastic strain was carried out at 50 % of the yield strength for the heat treatments given in Fig. 2 (b, d, e). Standard tensile specimens were used, and 50 % of the yield strength was determined as 18 MPa, 19 MPa, and 28 MPa for the conditions shown in Fig. 2 (b), (d), and (e), respectively. Two tensile specimens were used for each of the three tests in an MTS810 hydraulic test machine, and the nominal strain rate was 10^{-3} s^{-1}. An enlarged view of the elastic regions of the stress-

strain curves corresponding to the tensile tests prior to elastic straining as described in paragraphs 2.1 and 2.2 is presented in Fig. 3.

Standard tensile specimens were used for each of the different procedures shown in Fig. 2 (b-e), three parallel tensile tests were performed for each condition. Full stress-strain curves of the final conditions in Fig. 2, corresponding to AA for 26 h, were determined using a standard tensile testing set-up in an MTS810 hydraulic test machine operated at an initial nominal strain rate of 10^{-2} s^{-1}, equipped with a 25 mm extensometer. Full stress strain curves of the final conditions are plotted in Fig. 4.

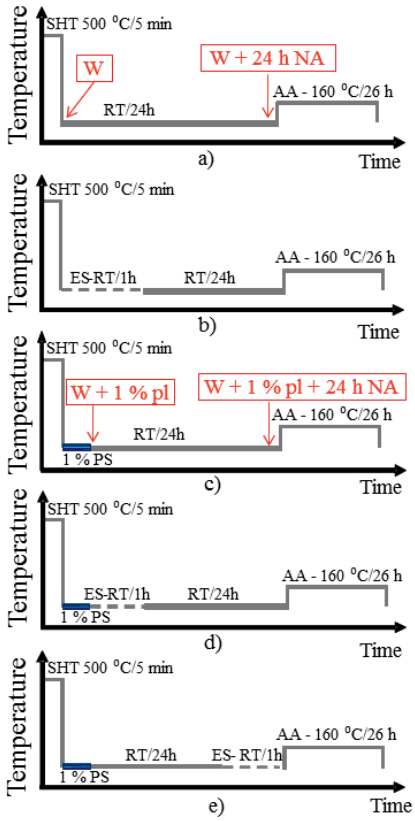

Fig. 2: Description of heat treatments where plastic deformation/strain (PS) was applied in combination with elastic strain (ES). A holding time of 1 h was chosen for elastic strain. The artificial aging was 26 h at 160 °C for all conditions. The heat treatment in (a) provides the reference. The red brackets with arrows indicate when the stress-strain tests in Fig. 3 were performed.

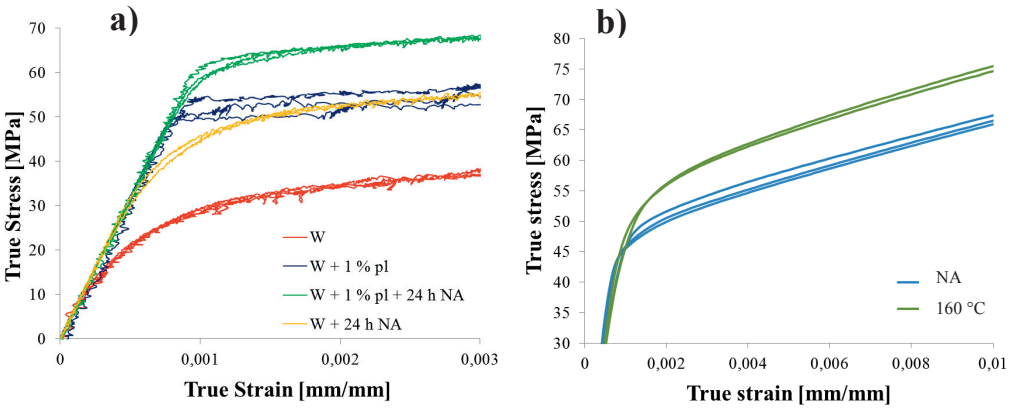

Fig. 3: Enlarged view of the elastic regions of the stress-strain curves corresponding to the tensile tests performed prior to ES as described in paragraphs a) 2.1 and b) 2.2. The corresponding points in the heat treatment are indicated in Fig. 2 with red brackets and arrows.

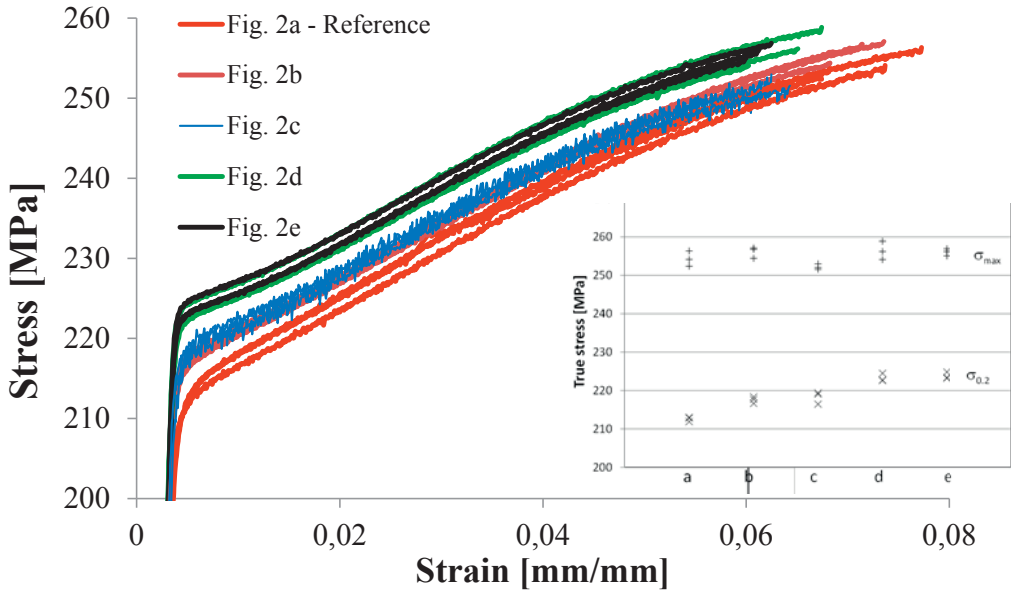

Fig. 4: Stress-strain curves corresponding to the heat treatments shown in Fig. 2. Three independent runs were performed for each condition. The insert shows σ_{max}, the ultimate tensile strength, and $\sigma_{0.2}$, the yield strength at 0.2 strain. Referring to Fig. 2 (a-e), heat treatments give three categories of strength: low (a), medium (b, c) and high (d, e).

The following can be concluded from the stress-strain curves in Fig. 4:

- The curves fall into three classes of strength: low (a), medium (b, c) and high (d, e).

- The yield strength of the reference sample (a) is lowest. Therefore, in comparison elastic strain (b), plastic deformation (c), or the combination of the two (d, e), increase the material strength after AA. Since a similar effect is absent in Fig. 5, where elastic strain was applied at the end of NA, it seems probable that elastic strain only enhances nucleation when performed directly after quick cooling (water quench), at the beginning of NA. At this point the matrix is in its most unstable state, being supersaturated in solute and vacancies and is more likely to be affected. When elastic strain is performed at the end of NA, clusters have already formed and the effect becomes negligible.

- The yield strength in curves (b) and (c) are similar, as are the ones in (d) and (e) with the highest values. This observation, together with the one above, show that strength increases with the amount of straining/ deformation applied to the material, i.e. reference → elastic strain → 1 % plastic deformation → elastic strain + 1 % plastic deformation.

2.2 Influence by elastic strain on subsequent age hardness

The influence of elastic strain on hardness evolution during aging has been investigated, where elastic strain was applied during NA or at the beginning of AA. The unstrained reference samples, each of dimension 15 x 15 x 5 mm^3, were cut from the extruded profiles. One piece was produced for each of the conditions as described below. The samples were ground from both sides to limit influence from extrusion marks/ effects and contamination etc. The pieces were given a SHT at 500 °C for 5 minutes in a salt bath, followed by water-quench (constituting condition 'W' in Fig. 5) and NA for 24 hours, before AA in an oil bath at 160 °C for 3 h, 7 h, 26 h and 11 days. Vickers hardness (HV) was measured within minutes for the 'W' condition in order to quantify the effect of atomic clusters forming during NA. HV was also measured after 24 h NA and after each AA time. In all cases, a DuraScan 70 machine from Struers was used with 1 kg load. Each HV data point is the average of six indentations with corresponding standard error [21]. In all cases, the hardness was measured on the surface of the extruded profiles, perpendicular to the extrusion direction. Fig. 5 gives a graphical representation of the thermomechanical treatment for all conditions and corresponding HV as a function of AA time.

The elastic strain was carried out at stress levels corresponding to 50 % of the yield strength, which had to be determined before the actual heat treatments could be carried out. For this purpose, two standard tensile specimens with dimensions given in Fig. 1 (b) were given a similar SHT as above, followed by water-quench and 24 h NA, after which they were tested at RT using an Instron tensile test machine, model no 1125. The tensile tests were performed according to [22]. Two other tensile specimens were subjected to the same heat treatment, with the difference that they had been tested in an air circulation oven at 160 °C immediately after 24 h NA. The tests at elevated temperature were performed according to [23]. A low nominal strain rate of 10^{-3} s^{-1} was used for both tensile tests. A yield strength of about 50 MPa was measured for both parallels in all tensile specimens. Following these measurements, the effect of elastic strain on hardness during subsequent AA was measured in the following way:

Three of the large tensile specimens (see Fig. 1 (a)) were given a SHT of 5 minutes at 500 °C in a salt bath, followed by water quench and 24 h NA, after which they were elastically strained to 25 MPa using a strain rate of 27 N/s. During NA, three specimens were held for 10 minutes, 1 h and 5 h respectively, after which hardness was measured, see the red arrows in Fig. 5 (a, c). Four small samples with dimensions 5 x 13 x 3 mm^3 were then cut from the gauge area of each of the elastically strained specimens and further artificially aged in an oil bath at 160 °C for 3 h, 7 h, 26 h and 11 days. In Fig. 5 (a) the AA times (red font) indicate the conditions chosen for TEM investigations, corresponding to 24 h NA + 1 hour elastic strain, followed by 26 h and 11 days of AA. In addition, TEM analysis was performed for the same AA times in the case of the unstrained reference sample. The hardness evolution for all conditions is shown in Fig. 5 (c).

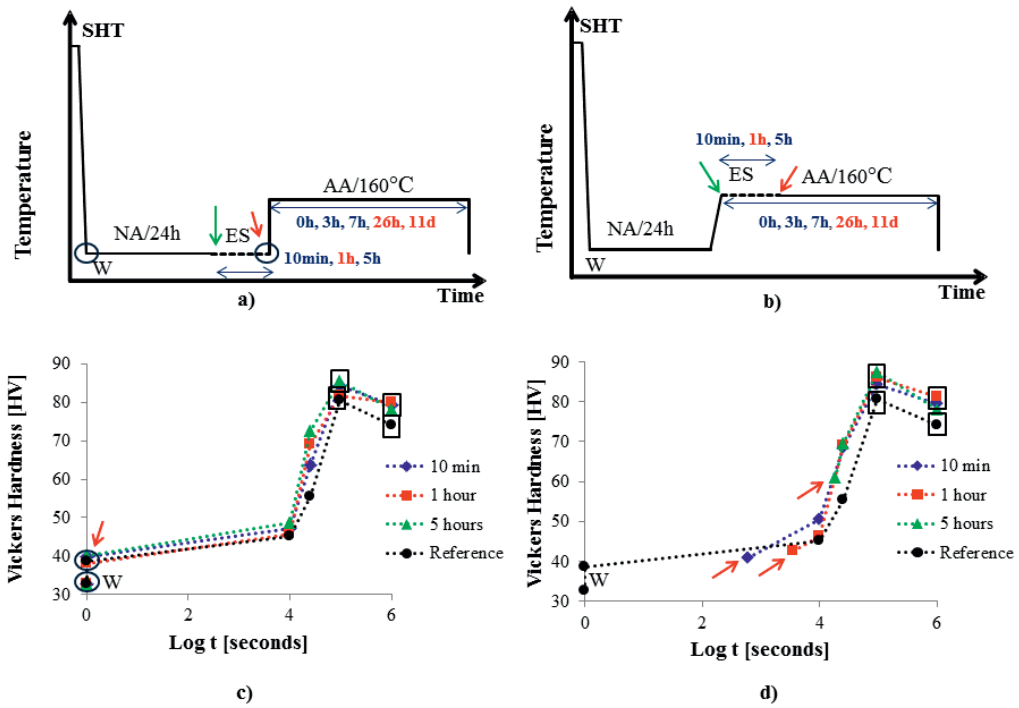

Fig. 5: Description of heat treatments with elastic strain (ES) applied during NA at RT (a) and at the beginning of AA (b). Holding times during ES and AA are indicated. Hardness evolution during AA are shown in (c) and (d) for the heat treatments in (a) and (b) respectively. Conditions chosen for TEM analysis are written in red text in (a, b) and their respective hardness indicated by large squares in (c) and (d). Red arrows indicate conditions and hardness just after ES. 'W' represents the condition and hardness of the reference sample after water-quenching from SHT. Green arrows in (a) and (b) indicate where the tensile tests presented in Fig. 3 were performed.

Another three large tensile specimens were given a SHT of 5 minutes at 500 °C in a salt bath, followed by water-quench and 24 h NA, after which they were brought to 160 °C in an air circulation oven and elastically strained to 25 MPa using a strain rate of 27 N/s. The three specimens were kept at 50 % of the yield strength at 160 °C for 10 minutes, 1 h or 5 h respectively, after which they were quenched in water to RT. Pieces of dimension 5 x 13 x 3 mm^3 each were cut from their gauge areas and HV was measured (see red arrows in Fig. 5 (b,

d)). Subsequently, the samples were placed in an oil bath at 160 °C for AA. The total holding time at the AA temperature (including the time needed for elastic straining) was 3 h, 7 h, 26 h and 11 days. A graphical representation of this heat treatment is shown in Fig. 5 (b) and the hardness evolution for all conditions is shown in Fig. 5 (d). The times in red font in Fig. 5 (b) indicate the conditions chosen for TEM investigations. The two conditions correspond to elastic strain for 1 h at 160 °C followed by (i) AA for 25 hours at 160 °C until a total 26 h at 160 °C, and (ii) followed by AA for 263 h at 160 °C, that is, a total of 11 days at 160 °C. The hardness corresponding to specimens selected for TEM investigations is shown in Fig. 5 (d). The red arrows in Fig. 5 (b, d) indicate the conditions at the end of the elastic straining time with corresponding hardness.

Based on the information in Fig. 5 the following observations can be made regarding the hardness evolution of the investigated conditions:

- The difference in hardness between condition 'W' and after 24 h NA in the case of the reference sample indicates an effect of atomic clustering during NA, see 'W' and red arrows in Fig. 5 (a, c). Some samples subjected to elastic strain show a slightly higher hardness after NA as compared to the reference sample, see Fig. 5 (c). This may be attributed to the effect of longer NA time because of the additional elastic strain, or internal variations in the material.

- The hardness during AA of all conditions subjected to elastic strain shows no clear differences from the reference. The elastically strained and reference conditions have a hardness peak after 26 h AA, after which hardness decreases, indicating the start of over-aging. Samples where elastic strain was performed during NA and samples where it was performed during AA both show similar evolution in hardness, although the peak hardness is slightly higher in the latter case. This difference is not larger than what could be attributed to statistical variations in the sample material. The holding time during elastic straining also does not affect the hardness evolution much during AA, although the spread in hardness as function of holding time of elastic strain is slightly higher in the case of elastic strain being performed during NA.

2.3 TEM investigations

In order to investigate the effects of 1 % plastic deformation, elastic strain or the combination of the two on precipitation, TEM specimens were prepared from the conditions listed below:

- The unstrained reference condition corresponding to AA for 26 h and 11 days, see Fig. 2 (a). These conditions will be referred to as Ref. 26 h and Ref. 11 d.

- Conditions corresponding to 24 h NA + elastic strain for 1 h during NA, followed by AA at 160 °C for 26 h and 11 days, see Fig. 5 (a, c). These conditions will be referred to as RT_ 1 h + 26 h and RT_1 h + 11 d.

- Conditions corresponding to NA for 24 h + elastic strain for 1 h at 160 °C followed by AA at 160 °C for 25 h and 263 h, see Fig. 5 (b, d). These conditions will be referred to as 160 °C _ 1 h + 25 h and 160 °C _ 1 h + 263 h.

- Conditions with a final AA for 26 h at 160 °C corresponding to the heat treatments described in Fig. 2 (b - e). These conditions will be referred to with the respective figure numbers.

Standard tensile specimens with the same geometry as shown in Fig. 1 (b) were used for this purpose, but with 5 mm thickness instead of 3 mm. The profile thickness of 5 mm was chosen to make disks with 3 mm diameter for the TEM specimens; these were punched out along the extrusion direction, from transversally cut slices. The disks were ground down to a thickness of 70-150 μm, after which they were electropolished using a Struers Tenu-Pol 5 electropolisher. The electrolyte consisted of one part HNO_3 and two parts methanol. The solution was kept at temperatures ranging from -25 °C to -30 °C by adding liquid nitrogen. The transmission electron microscope (TEM) used in this work was a Philips CM30, operated at 150 kV. TEM film negatives were used to obtain measurements of average precipitate needle lengths, cross sections, number densities and volume fractions. A Gatan parallel electron energy loss spectrometer (PEELS) was used to determine the thickness of the imaged areas. The method used for acquiring the quantitative results can be found in full detail elsewhere [2, 20].

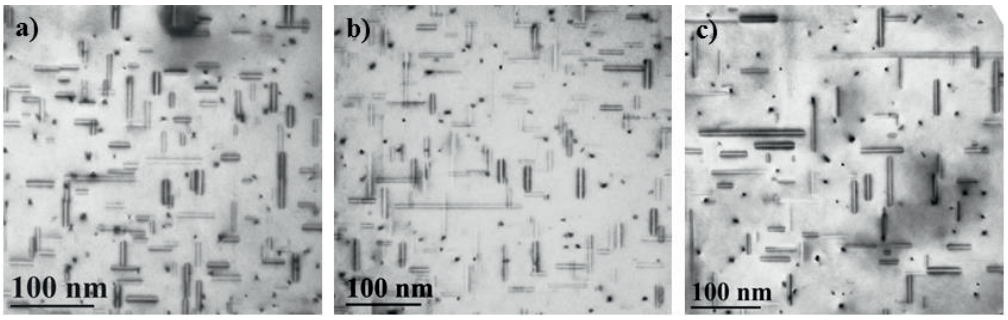

Fig. 6: TEM micrographs taken along a <100> zone axis, in areas with similar thicknesses. (a) Ref. 26 h; (b) 160 °C_ 1 h + 25 h (c) 160 °C_ 1 h + 263 h.

The quantitative results for average needle lengths are based on measurements of at least 1000 needles for each condition, while the average cross sections are calculated based on about 150 cross sections. All TEM micrographs were acquired along a <001>Al zone axis because of the preferential orientation of the metastable precipitates. Example TEM micrographs are shown in Fig. 6. It can be seen that the precipitation is reasonably homogeneous, in spite of some long precipitate needles. The quantified precipitate parameters are given in Table 2.

Table 2: Precipitate parameters for the conditions investigated by TEM. The volume fraction of precipitates has a 95 % probability of being within the intervals shown.

Condition	# Density [#/μm^{-3}]	Length [nm]	Cross Section [nm^2]	Volume Fraction [%]
Ref. 26 h	19600 ± 1600	34.1 ± 1.6	9.0 ± 0.3	(0.56, 0.67)
RT_1 h + 26 h	15300 ± 1700	34.3 ± 0.3	9.4 ±0.4	(0.47, 0.54)
160 ºC _1 h + 25 h	15700 ± 1600	28.7 ± 0.5	9.5 ± 0.3	(0.41, 0.47)
Fig. 2b	24500 ± 2700	29.9 ± 2.6	8.2 ± 8.2	(0.54, 0.66)
Fig.2c	17900 ± 1900	31.0 ± 1.2	8.4 ± 0.3	(0.44, 0.52)
Fig. 2d	16662 ± 1700	35.3 ± 0.3	9.2 ± 0.3	(0.52, 0.60)
Fig. 2e	16599 ± 1900	39.3 ± 2.8	8.6 ± 0.3	(0.51, 0.62)
Ref. 11 d	11900 ± 1400	48.8 ± 4.1	14.9 ± 0.6	(0.79, 0.96)
RT_1 h + 11 d	12900 ± 1600	48.0 ± 4.1	14.9 ± 0.8	(0.83, 1.02)
160 ºC _1 h + 263 h	11300 ± 600	55.4 ± 2.3	13.8 ± 0.6	(0.77, 0.91)

To investigate whether the hardening effect could be explained solely by precipitation hardening, dislocation densities were also examined. Six TEM micrographs were taken for three different heat treatment conditions at low magnification. The three conditions chosen were the reference sample as given in Fig. 2 (a), the elastic strain during NA sample as given in Fig. 5 (a) and finally the sample which was subjected to both plastic deformation and elastic strain during NA, Fig. 2 (e). These samples were chosen in order to compare dislocation densities and possible recovery processes as a consequence of the heat treatments they were given.

The samples were tilted slightly away from the same zone (<100> Al) where images of the needles were taken, as this turned out to give the best contrast between dislocations and the matrix. The micrographs were taken at the same TEM sample thickness of approximately 220 nm, and are shown in Fig. 7. The thickness was verified by using (P)EELS for each new area.

Fig. 7 gives the impression that the dislocation density is lowest for the reference sample in (a). No cell or subgrain formation is visible from the six micrographs taken at this condition. The six micrographs in Figs. 7 (b) and 7 (c), show some cell formation in certain areas, with the most obvious cell formation in Fig. 7 (c).

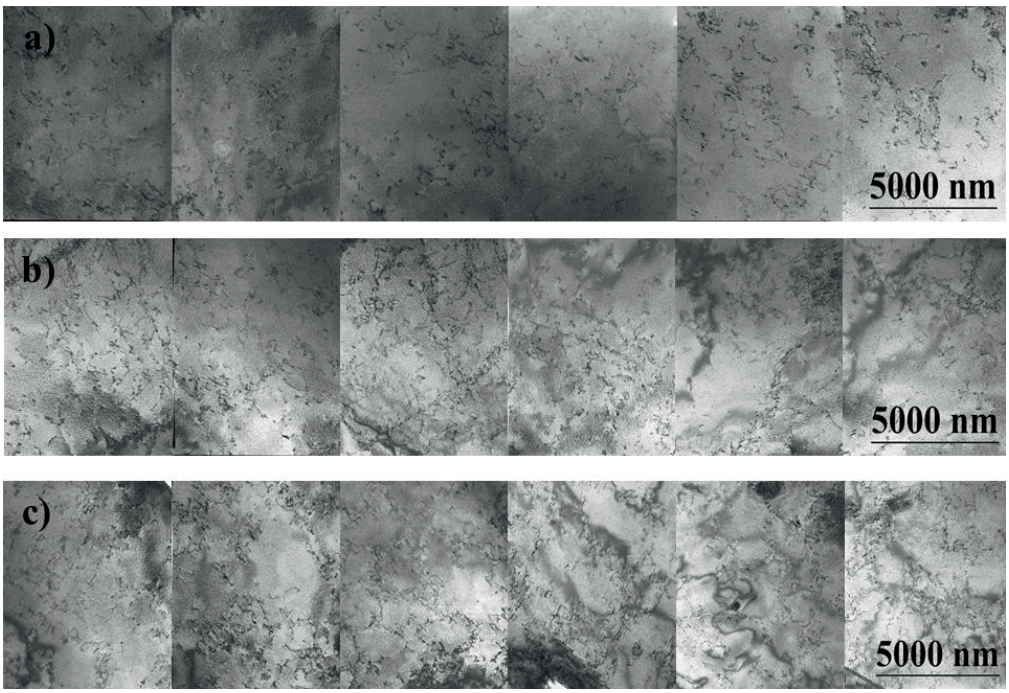

Fig. 7: TEM micrographs of dislocation densities for approximately 220 nm thick areas of the samples: (a) Heat treated according to Fig. 2 (a). (b) Heat treatment according to Fig. 5 (a). (c) Heat treatment according to Fig. 2 (e).

In some areas annihilation of dislocations within cell walls seems to have started. Fig. 8 is a higher magnification from one of many small areas relatively free from, but surrounded by dislocations, illustrating what could be the start of a cell forming in (a) and an example of a B' precipitate cross section in (b) which has nucleated on one of the dislocation lines.

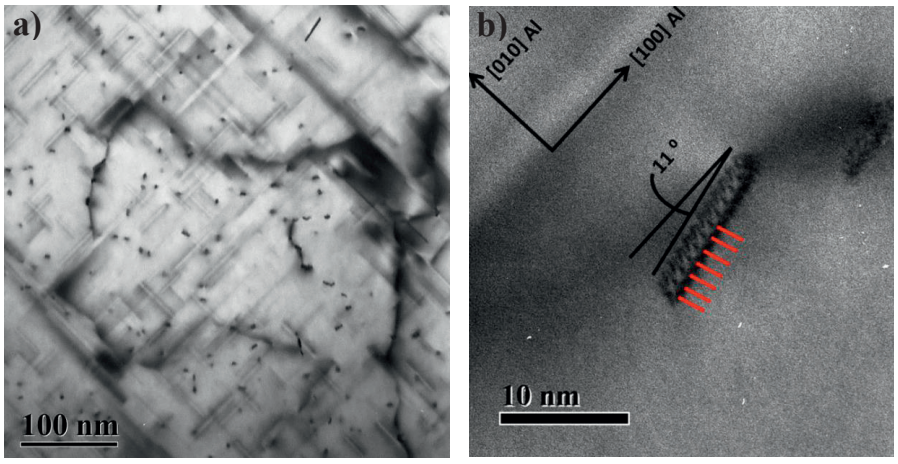

Fig. 8: TEM micrographs of (a) apparent cell formation in the material and (b) Precipitate forming on a dislocation line which is part of the cell wall in (a). The red lines indicate a periodicity of 10 Å, typical for the B' phase. The heat treatment was performed according to Fig. 2 (d).

3 Discussion

When comparing the values of 50 % yield strength measured just before elastic strain in the case of Fig. 2 (b, d, e) and Fig. 5 (a, b), several observations can be made:

- The yield strength after NA for 24 h (Fig. 5 (a)) was 25 MPa, while the lower value 18 MPa was measured just after SHT and water-quench, see Fig. 2(b). We believe this difference reflects how atomic clustering during NA increases the yield strength of the material. This effect can also explain the yield strength difference between conditions 'W + 1 % plastic deformation' (19 MPa) and 'W + 1 % plastic deformation + 24 h NA' (28 MPa), see Fig. 2 (d, e).

- A yield strength of 28 MPa was measured for the condition in Fig. 2 (e), after 1 % plastic deformation followed by 24 h NA. When comparing with the 25 MPa (Fig. 5 (a)), we assume this difference to be caused by dislocations introduced during plastic deformation in the latter case.

- 18 MPa was measured for the case of Fig. 2 (b), and 19 MPa for the case of Fig. 2 (d). As the only significant difference is 1 % plastic deformation introduced in the latter case, the 1 MPa deviation in strength may again be caused by introduced dislocations. Since this deviation is less compared to the yield strength measured after 24 h NA (~ 3 MPa), it may imply that introduced dislocations are greater assets for material strength when in an environment where atomic clusters have formed, compared to being in a random solid solution. It could be reasoned that, since dislocations provide preferable nucleation sites during AA [18, 19], they also may aid atomic cluster formation during NA.

The following observations can be drawn by comparing the precipitate parameters in Table 2 with the hardness and yield strength evolutions shown in Figs. 3, 4 and 5:

A decrease in precipitate number density coupled with an increase in average needle length, cross-section and volume fraction is observed when comparing 26 h and 11 days of AA (see Fig. 5), which is a common trend relating to microstructure coarsening due to overaging [2, 12].

When observing the yield strength of the conditions in Fig. 4 it can be seen that all strained conditions give higher strength than that of the un-strained reference. This indicates that the finest microstructure, corresponding to Fig. 2 (b), could be the result of enhanced precipitation due to the formation of favourable atomic clusters during NA. This could mean that formation of such clusters is enhanced or that the clusters are stabilized during elastic straining of the material. It can be observed that this effect becomes weaker when dislocations are introduced during 1 % plastic deformation, see Fig. 2 (b - e) and corresponding yield strength in Fig. 4.

Fig. 7 shows the dislocation distribution in a reference sample, a sample with elastic strain introduced during NA and a sample subjected to both plastic deformation and elastic strain during NA. It is evident that the energy stored in the reference sample material is insufficient for any significant recovery processes to start, as can be seen in Fig. 7 (a). This is consistent with the sample not being subjected to any strain during ageing. Knowing that recovery can also be caused by the energy stored after quenching from the high SHT temperature, in this

case it does not seem to have provided a high enough driving force for the process to start. It can be argued that the elastically strained sample shown in Fig. 7 (b) has a slightly higher dislocation density than that of 7 (a) and in some areas the driving force of recovery seems to have been high enough for the formation of tangled cell walls to form, which is the pre-stage of formation of low angle subgrain boundaries [24]. In Fig. 7 (c) a higher density of cells is present, forming a typical subgrain structure. Since this sample was plastically strained during NA it is to be expected that the driving force for recovery is higher than for the previously discussed samples in Fig. 7 (a) and 7 (b).

The observations discussed above lead to the conclusion that the main contributor to increased strength when 1 % plastic deformation is applied, when comparing to the reference sample, is not precipitation hardening, but the introduced dislocations. It is interesting to note that the highest yield strength was achieved for a combination of elastic strain and plastic deformation which, according to Table 2, cannot be attributed to precipitation hardening. Therefore, increased energy storage in samples where plastic deformation is combined with elastic strain appears to be the reason behind the increased hardness, which is associated with dislocation density and recovery.

4 Conclusions

The effects of 1 % plastic deformation, elastic strain, or a combination of the two on hardness, yield strength and precipitate formation have been investigated for an AA6060 alloy.

It was found that by applying elastic strain at the beginning of NA finer, denser precipitate microstructures formed during AA, which relates to increased yield strength in these conditions. The increased strength indicates that elastic strain in this case must promote the formation of favourable atomic clusters during NA. This strengthening effect was not found when 1 % plastic deformation was applied at the beginning of NA, or when elastic strain was applied at the end of NA or during the AA. Also, no increase in precipitate number density was found when elastic strain and 1 % plastic deformation were combined. Therefore, in all cases when plastic deformation was applied the strength increase must have been caused by the effect of introduced dislocations. Corroborating these results, an enhanced dislocation density was observed by TEM in the conditions where plastic deformation was applied. An increased density of dislocations related to a slightly lower precipitate number density after AA, as compared to an unstrained reference. It is suggested that a higher fraction of precipitates nucleated on the introduced dislocation lines, leading to faster overaging. The strength increase was highest when plastic deformation was combined with elastic strain, which could be associated to increased energy stored in the system leading to accelerated recovery and formation of dislocation cells.

Acknowledgements

Hydro Aluminium and the Research Council of Norway are gratefully acknowledged for the financial support through the BIA project no. 219371.

References

[1] C. D. Marioara, S. J. Andersen, J. Jansen and H. W. Zandbergen (2003), *The influence of temperature and storage time at RT on nucleation of β'' phase in a 6082 Al-Mg-Si Alloy*, Acta Mater., vol. 51, pp 789-796.

[2] C. D. Marioara, S. J. Andersen, H. W. Zandbergen and R. Holmestad (2005), *The Influence of alloy composition on precipitates of the Al-Mg-Si system*, Metall. Mater. Trans. A, vol. 36 A, pp 691-702.

[3] A. Serizawa, S. Hirosawa, T. Sato (2008), Metall. Mater. Trans. A 39A, pp 243–251.

[4] M. Torsæter, H. S. Hasting, W. Lefebvre, C. D. Marioara, J. C. Walmsley, S. J. Andersen and R. Holmestad (2010), *The influence of composition and natural aging on clustering during preaging in Al-Mg-Si alloys*, Journal of Applied Physics, vol. 108, issue 7, article nbr 073527.

[5] C. D. Marioara, S. J. Andersen, J. Jansen and H. W. Zandbergen (2001), *Atomic model for GP zones in a 6082 Al-Mg-Si system,* Acta Mater., vol. 49/2, pp 321-328.

[6] S.J. Andersen, H.W. Zandbergen, J. Jansen, C. Traeholt, U. Tundal,and O. Reiso (1998), Acta Mater., vol. 46 (9), pp 3283-98.

[7] H. K. Hasting, W. Lefebvre, C. Marioara, J. C. Walmsley, S. J. Andersen, R. Holmestad and F. Danoix (2007), *Comparative study of the β''-phase in a 6xxx Al-alloy by 3DAP and HRTEM*, Surf. Interface Anal., vol. 39, pp 189-194.

[8] R. Vissers, M. A. van Huis, J. Jansen, H. W. Zandbergen, C. D. Marioara and S. J. Andersen (2007), *The crystal structure of the β' phase in Al-Mg-Si alloys*, Acta Mater., vol. 55, pp 3815-3823.

[9] S. J. Andersen, C. D. Marioara, R. Vissers, A. Frøseth and H. W. Zandbergen (2007), *The structural relation between precipitates in Al-Mg-Si alloys and diamond silicon, with emphasis on the trigonal phase U1-$MgAl_2Si_2$*, Mater. Sci. Eng. A, vol. 444, pp 157-169.

[10] S. J. Andersen, C. D. Marioara, A. Frøseth, R. Vissers and H. W. Zandbergen (2005), *Crystal structure of the orthorhombic U2-$Al_4Mg_4Si_4$ precipitate in the Al-Mg-Si alloy system and its relation to the β' and β'' phases*, Mater. Sci. Eng. A, vol. 390, pp 127-138.

[11] R. Vissers, C. D. Marioara, S. J. Andersen and R. Holmestad (2008), *Crystal structure determination of the B' phase in Al-Mg-Si alloys by combining quantitative electron diffraction and ab-initio calculations*, Proceedings ICAA11, 22-26, Aachen, Germany, vol. 2, pp 1263-1269.

[12] C. D. Marioara, H. Nordmark, S. J. Andersen and R. Holmestad (2006), *Post-β" phases and their influence on microstructure and hardness in 6xxx Al-Mg-Si* alloys, J. Mater. Sci., vol. 41, pp 471-478.

[13] K. Matsuda, Y. Sakaguchi, Y. Miyata, Y. Uetani, T. Sato, A. Kamio,and S. Ikeno (2000), *Precipitation sequence of various kinds of metastable phases in Al-1.0 mass % Mg_2Si-0.4mass % Si alloy,* J. Mater. Sci., vol. 35, pp 179-89.

[14] J. Røyset, T. Stene, J. A. Sæter and O. Reiso (2006), *The Effect of Intermediate Storage Temperature and Time on the Age Hardening Response of Al-Mg-Si Alloys,* Mater. Sci. Forum, vols. 519-521, p 239.

[15] S. T. Chang, I. Wieler, N. Wanderka and J. Banhart (2009), *Positive effect of natural pre-ageing on precipitation hardening in Al–0.44 at % Mg–0.38 at % Si alloy*, Ultramicroscopy vol. 109, p 585.

[16] K. Matsuda, T. Kawabata, Y. Uetani, T. Sato, A. Kamio, and S. Ikeno (2000), *HRTEM Observation of G.P. Zones and Metastable Phase in Al-Mg-Si Alloys*, Mater. Sci. Forum, vols. 331–337, pp 989-94.

[17] JaeHwang Kim, C. D. Marioara, R. Holmestad, E. Kobayashi and T. Sato (2012), *Effects of Cu and Ag additions on age-hardening behavior during multi-step aging in Al–Mg–Si alloys*, Materials Science and Engineering A, vol 560, pp. 154-162.

[18] K. Teichmann, C. D. Marioara, S. J. Andersen and K. Marthinsen (2012), *The effect of preaging deformation on the precipitation behavior of an Al-Mg-Si alloy*, Metallurgical and Materials Transactions A, vol. 43 A (11), pp 4006-4014.

[19] K. Teichmann, C. D. Marioara, K. O. Pedersen and K. Marthinsen (2013), *The effect of simultaneous deformation and annealing on the precipitation behaviour and mechanical properties of an Al-Mg-Si alloy*, Materials Science and Engineering A, vol. 565, pp 228-235.

[20] S.J. Andersen (1995), *Quantification of the Mg_2Si β" and β' phases in AlMgSi alloys by transmission electron microscopy*, Metall. Mater. Trans. A, vol. 26 A, pp 1931-38.

[21] EN ISO 6507 – 1:2006, "Metallic Materials – Vickers hardness test – Part 1: Method of test at room temperature".

[22] EN ISO 6892 – 1:2009, "Metallic Materials – Tensile Testing – Part 1: Method of test at room temperature".

[23] EN ISO 6892 – 1:2009, "Metallic Materials – Tensile Testing – Part 2; Method of test at elevated temperature".

[24] John D. Verhoeven (1975), *Fundamentals of Physical Metallurgy*, John Wiley and Sons, p 170.

Thermal Migration of Alloying Agents in Aluminium

In progress

Paper 7

Thermal migration of alloying agents in aluminium

S.P. Cooil,[1] E.A. Mørtsell,[1] F. Mazzola,[1] M. Jorge,[1] S. Wenner,[1]
M. Edmonds,[2] L. Thomsen,[3] H.W. Klemm,[4] G. Peschel,[4] A. Fuhrich,[4]
M. Prieto,[4] Th. Schmidt,[4] J.A. Miwa,[5] R. Holmestad,[1] and J.W. Wells[1]

[1]*Department of Physics, Norwegian University of Science and Technology (NTNU), N-7491 Trondheim, Norway*

[2]*School of Physics and Astronomy and Monash Centre for Atomically Thin Materials, Clayton Victoria 3800, Australia*

[3]*The Australian Synchrotron, 800 Blackburn Road, Clayton, Victoria 3168, Australia*

[4]*Fritz-Haber Institute of the Max-Planck Society, Faradayweg 4-6 14195 Berlin Germany*

[5]*Department of Physics and Astronomy, Interdisciplinary Nanoscience Center (iNANO), University of Aarhus, 8000 Aarhus C, Denmark*

(Dated: July 30, 2016)

Abstract

The *in situ* thermal migration of alloying agents in an Al-Mg-Si-Li alloy is studied using surface sensitive photo-electron and electron diffraction/imaging techniques. Starting with the preparation of an almost oxide free surface (oxide thickness = 0.1 nm), the relative abundance of alloying agents (Mg, Li and Si) at the surface are recorded at various stages of thermal annealing, from room temperature to melting (which is observed at 550°C). Prior to annealing, the surface abundances are below the detection limit $\ll 1\%$, in agreement with their bulk concentrations of 0.423% Si, 0.322% Mg and 0.101% Li (atomic %). At elevated temperatures, all three alloying agents appear at drastically increased concentrations (13.3% Si, 19.7% Mg and 45.3% Li), but decrease again with further elevation of the annealing temperature or after melting. The temperature at which the migration occurs is species dependent, with Li migration occurring at significantly higher temperatures than Si and Mg. The mechanism of migration also appears to be species dependent with Li migration occurring all over the surface but Mg migration being restricted to grain boundaries.

Aluminium is one of the lightest and most abundant solid elements on earth, and has therefore attracted much attention for weight-conscious applications. In its pure elemental form, aluminium is a soft and malleable metal which is poorly suited to applications where strength is required. However, for more than a century, the inclusion of small quantities of alloying agents (in particular, magnesium and copper) has been shown to favorably modify aluminium's strength and hardness[1,2]. Whilst the initial development of aluminium alloys was driven by the need for light but strong airframes for lighter-than-air flight[3], aluminium alloys soon attracted attention for a wide range of weight-restrictive applications, including heavier-than-air flight, high performance motor vehicles, bicycles, and space vehicles. Very early on, aluminium alloys such as duralumin were also employed in medicine, notably as surgical splints and implants[1,4], where not only their weight and strength were important, but additionally, their low atomic number did not hinder diagnosis using the emergent X-ray radiographic techniques of the time[5]. Whilst radiology has developed dramatically over the last century, aluminium alloys are still of central importance; not only is their weight-to-strength ratio important, additionally their non-magnetic nature makes them well suited to high-field environments such as magnetic resonance imaging[6].

Whilst the alloying of aluminium began over a century ago, the parameter space is enormous and time consuming to explore. The wide choice in alloying agents (i.e. Cu, Mg, Mn, Si, Sn, Zn, Fe, Cr, V, Ti, Bi, Ga, Ge, Pb, Zr, Sc, and countless combinations thereof), mechanical processing treatments (i.e. deformation and work hardening) and thermomechanical treatments (i.e. heating time and rate, quenching and thermal cycling) all play an important role in the complex mechanisms responsible for the physical properties of the alloy. For example, in wrought alloys which have small amounts of Mg and Si as the main alloying agents (also known as 6000-series, or 6xxx, alloys) the strength has been shown to increase as a result of the aggregation of nano-sized metastable precipitate needles during age hardening, where the strength of the material usually peaks when the majority of the needles are of the so-called β'' type.[7]

Recently lithium has also attracted attention as a solute addition, as it is exceptionally lightweight and has been shown to improve the age-hardening response and thermal stability of Al alloys[8]. However it is believed that during the hardening process a significant proportion of Li migrates to the surface, leaving less Li available for the precipitation of hardening phases.[9] On the other hand, migration to surfaces and grain boundaries may be

advantageous for electrochemical applications and for corrosion resistance[10]. An extreme example of surface migration causing corrosion resistance is the formation of graphene from bulk impurities on a range of reactive metal surfaces[11,12], giving rise to a single-atom-thick inert and corrosion resistant coating with a broad range of potential applications[13,14]. It is therefore interesting to understand which bulk species agents migrate towards the surface and/or grain boundaries of the material and the thermal dependency of these mechanisms.

In this study we utilise experimental techniques based on photo-electron emission to study the migration of alloying agents during *in situ* thermal annealing. Specifically, we use X-ray photo-emission spectroscopy (XPS) and photo-emission electron microscopy (PEEM), supplemented by low energy electron microscopy (LEEM). These techniques are very surface sensitive[15,16] and are well suited to the study of light elements[17] and the spatial distribution of minority species[18], thus they are ideal for revealing the dynamics of surface migration in aluminium alloys.

A 4 kg cylindrical billet of an Al-Mg-Si-Li mix was cast and homogenized for three hours at 575°C before being air cooled to room temperature. The billet was preheated to about 540°C before extruding it as a round profile with a 20 mm diameter (for further details of the heat treatment, see Ref. 19). The abundance (atomic %) of the alloying agents in the Al-Mg-Si-Li alloy was measured by inductively coupled plasma optical emission spectroscopy and found to be 0.423% Si, 0.322% Mg, 0.101% Li, 0.097% Fe and 0.015% Mn. A 1 mm thick disk was cut perpendicular to the extrusion direction and further machined to a square of 10×10 mm^2. The sample surface was polished with grade 4000 SiC paper prior to electro-polishing (using an electrolyte consisting of 70% ethanol, 10% 2-butoxyethanol, 8% perchloric acid and 12% distilled water). Samples were then introduced into an Ultra High Vacuum (UHV) chamber where XPS or PEEM/LEEM measurements were performed. Prior to measuring, samples were further cleaned *in situ* in UHV by sufficient cycles of Ar^+ bombardment to remove the surface oxide. Additional *in situ* annealing was also performed, and is detailed below. XPS measurements were performed both using a home Mg-kα/Al-kα XPS instrument, and at the Soft X-ray endstation at the Australian Synchrotron[20]. PEEM/LEEM measurements were performed at the SMART instrument at the synchrotron light source "BESSY" in Berlin.[21]

Following the in-vacuum preparation and annealing to 200°C (for 5 min.), an XPS survey of the sample was conducted. Fig. 1a) shows an overview measurement which is dominated by the Al 2p and 2s core levels peaks and their rich plasmon loss structures. Small O 1s,

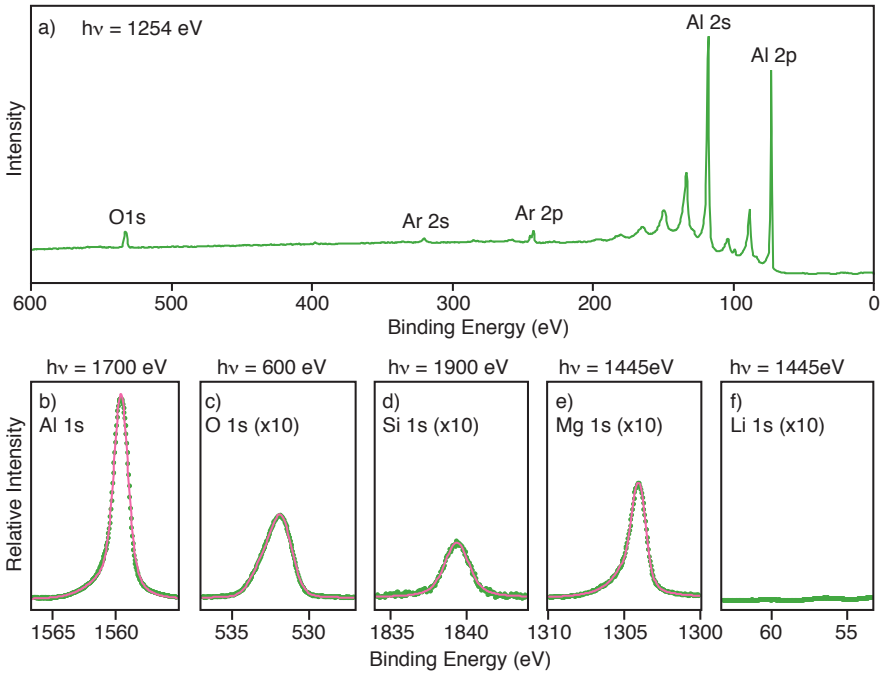

FIG. 1. (Color online) Synchrotron XPS measurements of an Ag-Mg-Si-Li alloy which has been prepared by *in situ* argon ion sputtering and annealing to 200°C. a) Photoemission survey spectra using photon energy $h\nu$=1254 eV. b-f) Detailed core level spectra for Al 1s, O 1s, Si 1s, Mg 1s and Li 1s respectively. The measured intensities (green markers) are shown following Shirley background subtraction, and fitted with Voigt functions (magenta lines), from which the peak area is extracted. The peaks are scaled by cross section and normalized to the intensity of the Al 1s photoelectron peak, thereby revealing the relative surface abundances; Al:Si:Mg:Li = 1 : 0.02 : 0.05 : 0.00. The oxygen peak is due to incomplete removal of the surface oxide; ≈0.1 nm remains. The kinetic energy of all photoelectron peaks is maintained at ≈140 eV to ensure similar escape depth of the emitted electrons.

Ar 2s and Ar 2p core levels peaks are also indicated in the spectra and are present as a result of Ar^+ sputtering and incomplete oxide removal. Using the assumption that the oxide is surface localised, this peak intensity corresponds to an oxide thickness of 0.1 nm. Detailed 1s core levels of Al, O, Si, Mg and Li were also collected using a range of photon energies (Fig. 1b-f). The photon energy was selected such that the kinetic energy of the escaping

photo-electron was ≈140 eV for each acquisition, thus maximising the surface sensitivity. 1s (singlet) core levels, lacking plasmon loss structures, were acquired to facilitate improved modeling; for each dataset, the core level peak has been modeled as Voigt contributions atop a Shirley background. As can be seen in the figure, the agreement between the model and measurement is excellent.

The measurements and peak analysis presented in Fig. 1 allow a quantitative understanding of the species present near the sample surface (i.e. within ≈1 nm). This is exemplified by the Li 1s core level, which is below the detection limit, thus indicating that a negligible amount of Li is localised at the surface. Unlike Li, the alloying agents Mg and Si are both present with detectable and significant abundances (≈ 2% and 5%, respectively). In other words, the quantity of Si and Mg located near the surface is approximately an order of magnitude larger than the bulk abundances of Al:Si:Mg:Li = $1 : 0.004 : 0.003 : 0.001$, indicating that at 200°C significant surface segregation of Si and Mg has already occurred and that surface segregation of Li has not.

In order to observe the thermal dependence of the segregation, we have performed similar measurements and analysis following annealing for 5 min. to a wide range of temperatures (from 25°C to 500°C). Fig. 2 shows the abundance of surface Mg, Li and Si (plotted relative to Al) as the annealing temperature is increased. For low temperatures (i.e. upto 120°C), the surface abundance of all three alloying agents is below the detection limit (consistent with the bulk concentrations). In the range 150°C to 450°C, Mg and Si migrate to the surface, with a maximum surface abundance of Mg 19.7% and Si 13.3% observed at 300°C. At higher temperatures, Mg completely redissolves into the bulk, with Mg $\rightarrow$ 0% at 450°C and Si partially redissolves with Si $\rightarrow$ 6.0% at 500°C.

The thermal migration of Li is somewhat different; below the relatively high temperature of 300°C, no surface Li is detected. Above this temperature, Li migrates to the surface extremely readily, resulting in a surface abundance of 45.3% (relative to Al) – an astounding amount considering that the initial bulk concentration was only 0.1%. Above 400°C, the surface abundance of Li is somewhat reduced, but still remains *very* high.

In order to understand the spatial distribution of the alloying agents at the surface, LEEM and PEEM were used. Bright-field LEEM images were collected using SV=5.5 eV, where SV is the 'start voltage', or potential of the sample relative to the incident electrons. This allows the polycrystalline nature of the material to be clearly observed; in Fig. 3a) we show such

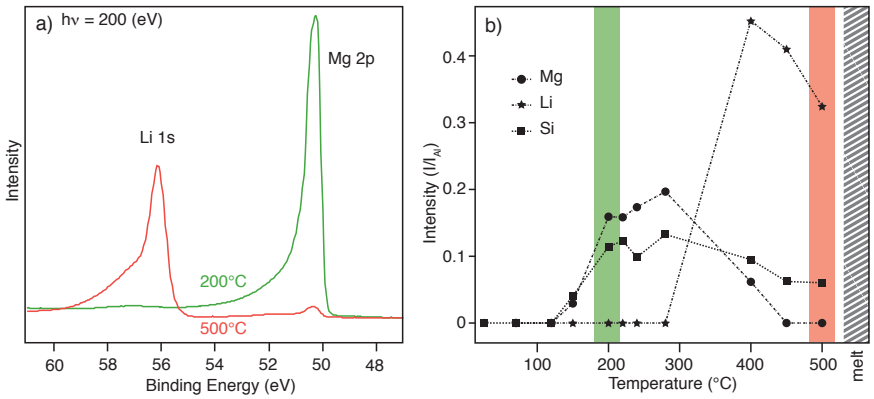

FIG. 2. (Color online) Thermal evolution of surface species. a) The Li 1s and Mg 2p core levels at two selected temperature. b) The surface concentrations of Mg, Li and Si (indicated by circles, stars and squares, respectively), extracted from XPS measurements, during annealing from room temperature to 500°C. The green and red bands indicate the temperatures at which the traces in panel a) are recorded.

an image in which a grain boundary triple-point is visible. Micro-diffraction patterns were collected from the three grains, and reveal that they are all close to {100} orientation, but individually tilted with respect to the sample surface; i.e. forming a pyramid-like geometry.

As with the XPS measurements presented above, the LEEM/PEEM allows *in situ* control of sample temperature. Measurements were made following a range of thermal annealing steps – as described for the XPS experiment. Fig. 3b shows an image formed using photo-emitted electrons; both the photon energy $h\nu$ and kinetic energy E_K of the emitted electron can be selected such that a particular binding energy E_B is probed ($E_B = h\nu - E_K$). Since E_B is element specific, this allows chemical-sensitive mapping and spectroscopy to be performed. In Fig. 3 we focus on the 400°C annealing step; according to the XPS study, this corresponds to a temperature at which Li, Mg and Si are abundant at the surface (Fig. 2). A large series of PEEM images were formed using constant photon energy ($h\nu$=150 eV) whilst SV is incrementally increased (equivalent to sweeping E_K), thus each image is sensitive to an incrementally different E_B (in the range E_B =40 to 65 eV). From such a dataset, it is straightforward to extract either a spatial image of a particular E_B (i.e. Fig. 3b, upper panel), or to extract spectral information (i.e. intensity of emitted electrons *vs.* E_B)

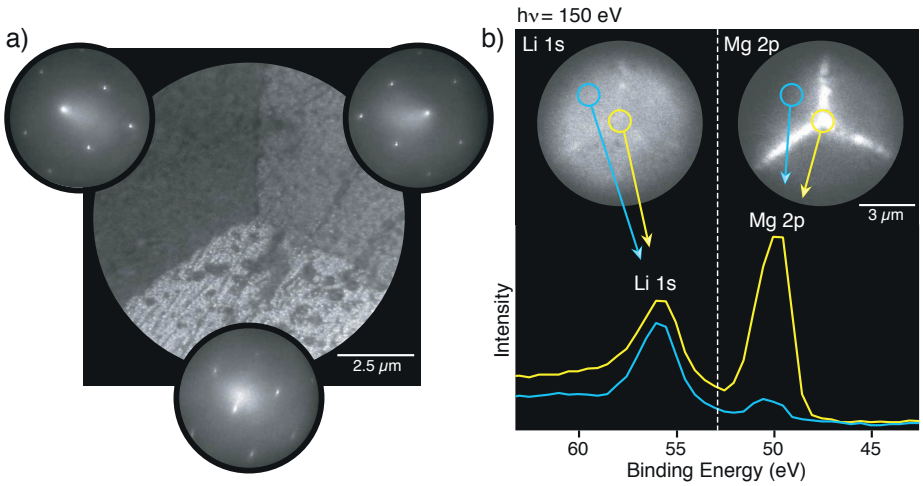

FIG. 3. (Color online) LEEM, LEED and PEEM study of a grain boundary following an *in situ* anneal of the sample to 400°C. a) Bright field LEEM image of the grain boundary (SV=5.5 eV). Contrast in each grain boundary is visible due to the different projections of the 0,0 diffraction spot in the micro-LEED patterns (shown as inserts for each grain). b) Images and spectra extracted from a series of PEEM images (ΔSV=0.5 eV) covering the kinetic energy range of the Li 1s and Mg 2p core levels. Upper panel; images formed using the peak intensity from the Li 1s and Mg 2p peak signals (left and right, respectively. Lower panel; Spectra extracted from within the grain boundary (yellow) and the grain surface (cyan).

for a specific position within the image (i.e. Fig. 3b lower panel). The two images we present in Fig. 3b correspond to the Li and Mg core-levels. Whereas the the image formed using the Li 1s peak has high intensity relatively uniformly distributed across the surface, indicating that Li is ubiquitous, the image formed using the Mg 2p peak shows very high intensity specifically at the grain boundaries. This observation is additionally supported by the spectroscopic measurements: the lower panel shows that large Li and Mg peaks are observed at the grain boundary intersection (yellow trace and yellow circle), whereas away from the boundaries, a similar quantity of Li is present but Mg is much reduced (cyan trace and cyan circle). We therefore infer that, whilst these alloying agents both migrate to the surface during annealing, the mechanism is somewhat different; Mg is predominantly observed at the grain boundaries, whereas Li is ubiquitous.

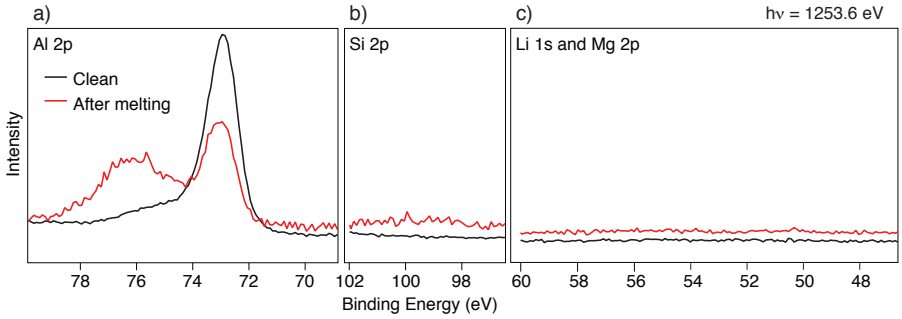

FIG. 4. (Color online) XPS measurements of the clean Al-Mg-Si-Li sample prior to annealing (black traces) and after annealing to the melting point ($T = 550$°C, red traces). a) The Al 2p region showing that the surface oxide (component at $E_B \approx 77$ eV) has increased during the melting. b) The Si 2p region and c) the Li 1s and Mg 2p region showing that these species are below the detection limit.

In order to observe the redissolving of alloying agents from the surface, we have also conducted XPS measurements at the melting temperature. In Fig. 4, XPS measurements are shown after melting (which was observed at 550°C), and are compared with measurements from the initial (not annealed) surface. Not surprisingly, the Mg is essentially absent. Already prior to melting, the Mg surface concentration was observed to return to its initial value of ≈0 (see Fig. 2b), indicating that the Mg was fully redissolved at high temperatures prior to melting. In addition to this, the surface abundance of both Li and Si also reduce after melting. In Fig. 2b, significant concentrations of both Li and Si were observed at T=500°C (i.e. just below the melting point) – however on melting, the concentrations return to their initial values of ≈0. In fact, after melting, the only core level observed in Fig. 4 is Al 2p. One can also observe that, whilst the total area of the Al 2p core level is not significantly changed, the high binding energy shoulder ($E_B \approx 77$ eV) has grown into a more distinct peak. This component corresponds to oxidised aluminium; this oxidation has occurred during the melting experiment and is simply due to a worsening of the base vacuum when melting the sample. Although the oxide component is large compared to the initial surface, it is worth restating that these measurements are especially surface sensitive. In fact, this oxide component corresponds to a surface oxide layer only 0.37 nm thick (c.f. 0.10 nm initially).

In conclusion, we have demonstrated that the combination of XPS and LEEM/PEEM is a powerful approach for studying the surface migration of alloying agents during *in situ* annealing at a wide range of temperatures from room temperature to melting at 550°C. Surface sensitive XPS, LEEM and PEEM measurements reveal both spectroscopic and spatial information of the migration processes in an Al-Mg-Si-Li alloy. Dramatic migration of Mg, Si and Li to the surface is observed – with the surface contributions increasing by more than 2 orders of magnitude above their initial (bulk) concentrations. For the case of Li, the initial concentration is ≈0.1%, but rises to 45.3% at the surface following annealing to 400°C. The surface migration is somewhat reversible; at higher temperatures, Mg is completely redissolved into the bulk whereas the surface concentrations of Si and Li reduce, but remain high compared to the initial values. On melting (at $T = 550$°C), the surface abundance of Si and Li also return to their initial values, either due to redissolving into the bulk, although loss of Li via evaporation is also a possibility. PEEM/LEEM measurement further reveal that the surface migration is not the same for all species; Mg migration is dominated by grain boundaries whereas Li is observed across the entire surface. Since the abundance of each species at the surface/grain-boundary follows its own temperature dependence, we speculate that it will be possible to control the surface termination of these alloys by careful control of the annealing temperature. More specifically, susceptibility to inter-granular corrosion is reduced when the grain boundaries are enriched by Mg[22]. Thus it should be possible to find the maximum corrosion resistance for Mg-based alloys by optimising the Mg concentration at grain boundaries using the annealing temperature. Determining when the alloying agents have diffused to the surface during annealing can alter the physical properties of the material to a large extent. The Si:Mg ratio within the grains will be influenced by surface migrations, and is very important for the formation of the nanosized precipitate phases during hardening. Low Si:Mg ratios typically suppress the formation of the phases promoting strength, and the alloy becomes softer than in regions with higher Si:Mg ratios[23]. Li depletion also leaves less solute available for the precipitation of hardening phases, rendering the material softer than in regions with more Li[8]. By documenting at which temperature Li depletion occurs, this effect can readily be avoided. We conclude that *in situ* annealing and surface sensitive photo-emission methods are able to provide a wealth of information on the migration of alloying agents in solid light metal alloys such as Al-Mg-Si-Li, which will be important for thermomechanical treatments intended for optimising the physical properties

of the alloys, and will give essential information for tailoring new alloys.

Acknowledgments: The project has been supported through the BIA RolEx project (No. 219371) by Hydro Aluminium and the Research Council of Norway. This research was partially undertaken on the soft X-ray beamline at the Australian Synchrotron (AS), Victoria, Australia and partially at the SMART beamline at 'BESSY' in the Helmholtz Zentrum, Berlin (HZB); we thank AS and HZB for the allocation of synchrotron time and for technical support.

APPENDIX: High kinetic energy 1s cross-sections for the solid light elements

It is common practice in quantitative photo-emission studies to use the calculations by Yeh and Lindolf[24] to estimate the photo-ionisation cross-sections. As well as the original paper, these calculations form the backbone of several more recent analysis tools, and are available in a widely used, convenient online resource[25]. However, in both the original paper, and the website, the calculations are only evaluated in the energy range $h\nu < 1500$ eV. As high energy XPS becomes more available, there is an increasing need for providing cross-section data for higher photon energies. For example, in this work, we have acquired core level data at photon energies up to 1980 eV.

More specifically, for this work, an estimate of the photo-ionisation cross-section is needed for Al 1s and Si 1s at $h\nu$ =1700 and $h\nu$ =1980 eV, respectively. The binding energies of these core levels are outside of the energy range considered by Yeh and Lindolf[24]. To overcome this problem, we first investigate the functional form of the 1s cross-sections for solid light elements in general.

Although the functional form of the cross-section may be more complex at low photon energy, the high energy tail can be well approximated as an exponential decay. This is evident in Fig. 5, where the 1s cross-sections are plotted for elements z =3 to 14 (Li to Si). For z =3 to 12 (Li to Mg), the cross-sections from Refs. 24 and 25 are plotted (dashed lines) for the energy range $h\nu < 1500$ eV. These plots are overlaid by simple exponential decays for the energy range $h\nu$ =1000 to 2500 eV, by thick solid traces of matching colour. In the range $h\nu$ =1000 to 1500 eV, both the calculated cross-section and the exponential decay co-exist. As can be seen in the Fig. 5, the match is extremely close and the thick trace of each exponential decay sit directly on top of the underlying dashed line.

In Fig. 5, we have chosen to plot the exponential decay in the form:

$$\chi_z = y_{0,z} + A_z \exp\left\{\frac{-(h\nu - 1000)}{\tau_z}\right\} \tag{1}$$

where z is the atomic number, χ_z is the cross-section and $y_{0,z}$, A_z and τ_z are element specific constants found by fitting the exponential function to the literature cross-sections (in the energy range $h\nu$ =1000 to 1500). The extracted values of $y_{0,z}$ and A_z and are tabulated in table I. In all cases, τ_z was found to be 330.63. The cross-section can only be estimated in this way for elements up to Mg (z=12), because Ref. 24 does not contain calculations for the

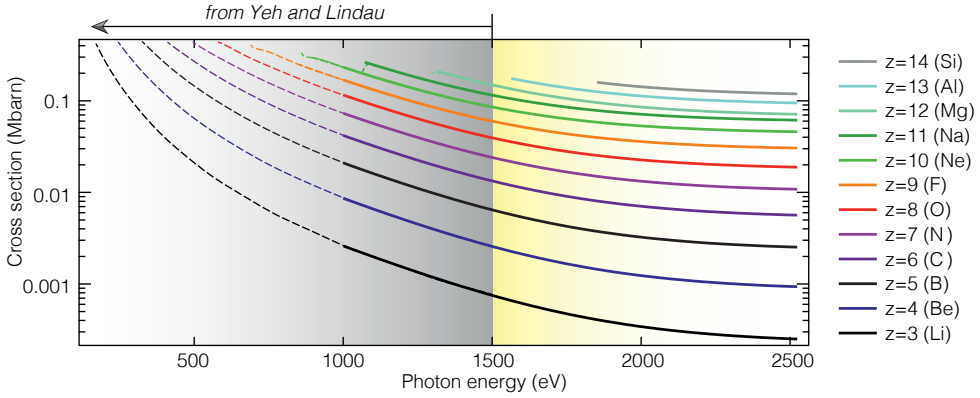

FIG. 5. (Color online) Calculated and extrapolated photo-ionisation cross-sections of the 1s orbitals of elements z =3 to 14. Dashed lines show the values calculated by Yeh and Lindau[24] (available only for $h\nu < 1500$ eV). Thick solid lines overlap with the calculated values in the range $1000 < h\nu < 1500$, and are extrapolated to higher energy.

1s orbital of heavier elements. Instead we observe that $y_{0,z}$ and A_z both follow a power-law dependence with z, i.e. $y_{0,z} \propto z^n$ and $A_z \propto z^m$. This makes it straightforward to extrapolate the coefficients in table I for z =13 and 14, and so to estimate the 1s high-photon-energy photo-ionisation cross-section for elements $z \geq 13$, which are not included in Ref. 24. This extrapolation method is consistent with the related study by Verner and Yakovlev[26].

TABLE I. Values of $y_{0,z}$ and A_z for $z = 3$ to 14. In all cases, $\tau_z = 330.63$. For $z = 3$ to 12, these values are found by fitting an exponential decay to the calculations of Yeh and Lindau[24] in the energy range $1000 < h\nu < 1500$. For $z = 13$ and 14, these (italicised) values are extrapolated from the corresponding constants for the lighter elements.

element	z	$Y_{0,z}$	A_z
Li	3	0.0002267	0.0023805
Be	4	0.00085627	0.0077799
B	5	0.0023396	0.018637
C	6	0.0052806	0.036592
N	7	0.01019	0.063029
O	8	0.017888	0.097847
F	9	0.029097	0.14007
Ne	10	0.04407	0.18863
Na	11	0.058946	0.25565
Mg	12	0.067623	0.36963
Al	*13*	*0.090078*	*0.46876*
Si	*14*	*0.11301*	*0.60572*

[1] S. Melville, "Demonstration of "duralumin."," Proceedings of the Royal Society of Medicine **6**, 161 (1913), URL http://www.ncbi.nlm.nih.gov/pmc/articles/PMC2006514/.

[2] R. Woodward, "Recent developments in light alloys," NASA Technical Reports **NACA-TM-3**, 93R10024 (1920).

[3] D. Robinson, *Giants in the Sky: A History of the Rigid Airship* (University of Washington Press;, 1973), 1st ed.

[4] E. M. Little, "A lecture on a new material (duralumin) for surgical appliances: Delivered at the medical graduates' college and polyclinic," British Medical Journal **1**, 236 (1912), URL http://www.ncbi.nlm.nih.gov/pmc/articles/PMC2344469/.

[5] T. H. Bryce, "Certain points in the anatomy and mechanism of the wrist-joint reviewed in the light of a series of Røntgen ray photographs of the living hand," Journal of Anatomy and Physiology **31**, 59 (1896), URL http://www.ncbi.nlm.nih.gov/pmc/articles/PMC1327812/.

[6] H. Elhawary, A. Zivanovic, B. Davies, and M. Lampérth, "A review of magnetic resonance imaging compatible manipulators in surgery," Proceedings of the Institution of Mechanical Engineers, Part H: Journal of Engineering in Medicine **220**, 413 (2006), http://pih.sagepub.com/content/220/3/413.full.pdf+html, URL http://pih.sagepub.com/content/220/3/413.abstract.

[7] C. D. Marioara, H. Nordmark, S. J. Andersen, and R. Holmestad, "Post-β'' phases and their influence on microstructure and hardness in 6xxx Al-Mg-Si alloys," Journal of Materials Science **41**, 471 (2006), ISSN 1573-4803, URL http://dx.doi.org/10.1007/s10853-005-2470-1.

[8] Y. Koshino, M. Kozuka, S. Hirosawa, and Y. Aruga, "Comparative and complementary characterization of precipitate microstructures in Al–Mg–Si(–Li) alloys by transmission electron microscopy, energy dispersive x-ray spectroscopy and atom probe tomography," Journal of Alloys and Compounds **622**, 765 (2015), ISSN 0925-8388, URL http://www.sciencedirect.com/science/article/pii/S0925838814026371.

[9] H. J. Leighly and P. G. Coleman, "Vacancy clustering in quenched Al-Li solid solution alloys studied by doppler broadening spectroscopy," Journal of Physics: Condensed Matter **10**, 10423 (1998), ISSN 0953-8984, URL http://stacks.iop.org/0953-8984/10/i=46/a=010.

[10] M. Hurlen Larsen, J. C. Walmsley, O. Lunder, and K. Nisancioglu, "Effect of heat treatment

on grain boundary nanostructure and corrosion of low copper AlMgSi alloy," ECS Transactions **3**, 167 (2007), URL http://ecst.ecsdl.org/content/3/31/167.

[11] J. W. May, "Platinum surface LEED rings," Surface Science **17**, 267 (1969), URL http://www.sciencedirect.com/science/article/pii/0039602869902271.

[12] J. Wintterlin and M.-L. Bocquet, "Graphene on metal surfaces," Surface Science **603**, 1841 (2009), ISSN 0039-6028, special Issue of Surface Science dedicated to Prof. Dr. Dr. h.c. mult. Gerhard Ertl, Nobel-Laureate in Chemistry 2007, URL http://www.sciencedirect.com/science/article/B6TVX-4VCH6T7-3/2/6586fbab9f367324b38146b06f401fd8.

[13] L. Nilsson, M. Andersen, R. Balog, E. Lægsgaard, P. Hofmann, F. Besenbacher, B. Hammer, I. Stensgaard, and L. Hornekær, "Graphene coatings: Probing the limits of the one atom thick protection layer," ACS Nano **6**, 10258 (2012).

[14] F. Mazzola, T. Trinh, S. Cooil, E. R. Østli, K. Høydalsvik, E. T. B. Skjønsfjell, S. Kjelstrup, A. Preobrajenski, A. A. Cafolla, D. A. Evans, et al., "Graphene coatings for chemotherapy: avoiding silver-mediated degradation," 2D Materials **2**, 025004 (2015), URL http://stacks.iop.org/2053-1583/2/i=2/a=025004.

[15] M. P. Seah and W. A. Dench, "Quantitative electron spectroscopy of surfaces: A standard data base for electron inelastic mean free paths in solids," Surface and Interface analysis **1**, 2 (1979).

[16] J. A. Miwa, P. Hofmann, M. Y. Simmons, and J. W. Wells, "Direct measurement of the band structure of a buried two-dimensional electron gas," Phys. Rev. Lett. **110**, 136801 (2013).

[17] S. P. Cooil, J. W. Wells, D. Hu, Y. R. Niu, A. A. Zakharov, M. Bianchi, and D. A. Evans, "Controlling the growth of epitaxial graphene on metalized diamond (111) surface," Applied Physics Letters **107**, 181603 (2015), URL http://scitation.aip.org/content/aip/journal/apl/107/18/10.1063/1.4935073.

[18] S. P. Cooil, F. Mazzola, H. W. Klemm, G. Peschel, Y. R. Niu, A. Zhakarov, A. Evans, T. Schmidt, M. Y. Simmons, J. A. Miwa, et al., "In-situ patterning of ultra sharp dopant profiles in silicon," *in preparation* (2016).

[19] E. Mørtsell, C. Marioara, S. Andersen, J. Røyset, O. Reiso, and R. Holmestad, "Effects of germanium, copper, and silver substitutions on hardness and microstructure in lean Al-Mg-Si alloys," Met. Trans. A, (2015).

[20] B. C. C. Cowie, A. Tadich, and L. Thomsen, "The current performance of the wide range (90–2500 ev) Soft X-ray Beamline at the Australian Synchrotron," AIP Conference Proceed-

ings **1234**, 307 (2010), URL http://scitation.aip.org/content/aip/proceeding/aipcp/10.1063/1.3463197.

[21] T. Schmidt, U. Groh, R. Fink, E. Umbach, O. Schaff, W. Engel, B. Richter, H. Kuhlenbeck, R. Schlögl, H.-J. Freund, et al., "XPEEM with energy-filtering: advantages and first results from the SMART project," Surface Review and Letters **9**, 223 (2002).

[22] J. Holmestad, "(scanning) transmission electron microscopy studies of grain boundary segregation relevant to intergranular corrosion in Al-Mg-Si-Cu alloys," Doctoral thesis, http://hdl.handle.net/11250/283573 (2015).

[23] M. Torsæter, H. S. Hasting, W. Lefebvre, C. D. Marioara, J. C. Walmsley, S. J. Andersen, and R. Holmestad, "The influence of composition and natural aging on clustering during preaging in al–mg–si alloys," Journal of Applied Physics **108**, 073527 (2010), URL http://scitation.aip.org/content/aip/journal/jap/108/7/10.1063/1.3481090.

[24] J. J. Yeh and I. Lindau, "Atomic subshell photoinoization cross sections and asymmetry parameters: $1 \leq Z \leq 103$," Atomic Data and Nuclear Data Tables **32**, 1 (1985).

[25] URL https://vuo.elettra.eu/services/elements/WebElements.html.

[26] D. A. Verner and D. G. Yakovlev, "Analytic fits for partial photoionization cross sections," Astrophysical Applications of Powerful New Databases, ASP Conference series **78**, 57 (1995).

Part III

Concluding Remarks

Chapter 5

Conclusions and Outlook

This thesis has resulted in seven journal papers, which present the main findings of this work. The focus has been on understanding extrudability and strength of Al 6xxx alloys with emphasis on understanding precipitate phases down to the atomic scale. The early stages of precipitation and growth have been given particular attention in many of the papers. In this chapter a summary and the final conclusions based on the most important results will be given. Further work and "what comes next" will be given in the 'Outlook' section of this chapter.

5.1 Conclusions

6xxx alloys with alloying agents Li, Cu, Ge and Ag, alone or combined, have been investigated. The total solute contents were reduced or unchanged by removing a fraction of Mg and Si while adding back a smaller or equal quantity of solute. All elements have a significant effect on the main hardening precipitate phase *β''*. The most effective solute addition "per at %" proved to be Ge, leading to a refined precipitate microstructure. Ge promotes disordered precipitate phases and new stacking variation of the *β''*-eyes. Cu and Ag both enter the precipitate needle structures, and change the precipitation sequence of Al-Mg-Si alloys. Li additions did not alter the precipitation sequence noticeably, but seemed to enter the *β''* phase structure.

HAADF-STEM investigations revealed how Ge occupies Si sites in the *β''*-eyes while Li occupy Mg sites, particularly the Mg3 sites. These findings were further supported by DFT calculations of volume misfits, bonding energies and simulations of different stacking variations of the *β''*-eyes. Both DFT calculations and HAADF-STEM intensities suggest it is most favourable for Mg to occupy the Mg1 sites in the *β''*-eyes, while Al goes to Si3 sites

[74] [77]. From DFT, it appears that Ge has the highest affinity to vacancies out of the different solute additions in this work. This strongly suggests that Ge creates more nucleation sites for precipitation, causing the number density of precipitate needles to increase and refining the microstructure [24] [34].

A version of the Q'/C-plate local configurations were discovered, containing Ag at the previously discovered Cu sites [78]. DFT simulations of this phase with Ag at Cu positions suggested it to be energetically favourable. Ag typically enriches the Al matrix at the precipitate/matrix interface. Ag has a low volume misfit in the Al matrix and a relatively high affinity to vacancies in Al. These mechanisms cause Ag to behave similar to both Al and Cu in this case [24].

Atomic resolution EELS has been performed on a precipitate cross section in a multicomponent, Al-Mg-Si-Cu-Ge-Ag alloy. The challenging aspects of determining elemental distribution inside such precipitates have been demonstrated. Combining EELS, HAADF-STEM and correlative analysis gave a reasonable model of the elemental distribution inside the cross section [61]. With EELS alone, it was possible to resolve the fcc Al lattice along the [100] al zone axis. The hexagonal Si-network was unmistakable across large areas of the cross section [32]. By combining these techniques, it was possible to determine a mix of elements residing in specific atomic columns.

It has been shown how elastic strain and small plastic deformations can enhance peak hardness and tensile strength of a common Al-Mg-Si alloy [79]. The strengthening effect of elastic strain only occurs if elastic strain is applied during the nucleation stage of the precipitation, directly after SHT and at the beginning of NA. 1 % plastic deformation also enhances the material strength compared to an undeformed reference alloy, because of the introduction of dislocations to the material [11].

The combination of XPS and XPEEM has grand potential for *in-situ* investigations on the migration of solute additions to alloy surfaces [67]. An Al-Mg-Si-Li alloy was studied by these methods, revealing dramatic migration of Li, Mg and Si to the alloy surface during annealing of the alloy. While Li and Si can be found all over the surface at elevated temperature, Mg mainly migrates to grain boundaries [80]. Intriguingly, the starting concentration of Li at the material surface was below the detection limit (< 0.1 at %) while during the following annealing to 400 °C, the surface concentration of Li had risen to more than 40 at % [81] [82].

5.2 Outlook

One of the major points when it comes to further work related to this thesis is the extrusion of all alloys at an industrially relevant scale. Improving the ease at which aluminium alloys can be extruded is after all the industrial motivation. The extrudability of the most promising alloy types needs to be checked. Interestingly, some of the tensile properties do not

correspond directly with the HV measurements, these mechanisms need to be better explained.

There are many possibilities to extend the work presented in this thesis further. In appendix A full sets of tensile curves are presented, which were performed at three AA temperatures for four of the most promising alloys. For full understanding of the nine alloys, tensile testing of all should be performed and compared to each other.

The results from the Ge and Li added alloys are intriguing, especially with respect to the location of Ge and Li columns inside the β'' phase [77]. Considering how Ge occupies Si sites in the β''-eyes, while Li occupies the Mg sites, it would be interesting to make an alloy with both Ge and Li additions. Predictions based on previous alloy types suggest that such an alloy has great strength potential, and we might expect the β'' phase as the main hardening phase. Further, it would also be interesting to do DFT calculations of β'' unit cells consisting of Ge and Li, to check the formation enthalpy. Part of this work is already in progress.

Some of the atomic scale results clearly show that atomic columns in the precipitate cross sections can consist of a mix of elements in many cases. Atom probe would be a great option to obtain a 3D view of the microstructure. By using this technique it would be possible to expand the knowledge of elemental occupancy in atomic columns. Additional quantitative STEM would reveal the connection between intensity variations and elemental occupation in atomic columns. This work has been initiated and there are already interesting results that are intended for publication.

After revealing that elastic strain only has an effect on precipitation if applied at the beginning of NA, it would be interesting to do a more complete investigation of different heat treatments employing this knowledge [79]. Full HV curves and tensile tests for this condition would be helpful to see if the effect is unchanged with time and different heat treatments.

A great challenge is to understand in detail what are happening during the nucleation and early growth stages of precipitate needles in Al alloys. In-situ experiments using a heating holder combined with a probe corrected TEM would possibly enable us to see the complete process. In-situ experiments with a heating holder have already been conducted successfully at the NORTEM facilities for nanowires [83], and it should be feasible to similar investigations while annealing Al alloy samples.

It would be interesting to further extend the XPS and XPEEM experiments to determine how other alloying elements than Li, Mg and Si migrate towards the material surface during annealing. Further investigations could also extend into finding the diffusion constant of alloying agents in Al alloys with specific solute concentrations.

Appendix A

Unpublished Results

In connection to the results published in paper 1 [84] there have been performed tensile tests using a laser extensometer for four of the most promising alloys at three different AA temperatures. The tensile tests have been performed according to the ISO standard for tensile testing at RT [85]. The alloys RXG2, RXGC1 and RXGC2 were chosen in addition to the dense reference alloy RX0, because of their interesting hardening responses and thermal stabilities. The heat treatment of the material used for tensile specimens was identical to that presented in [86]. It should be noted that the duration of AA was 2 hours for tensile specimens, as opposed to the 4 h ageing time of TEM samples. The heat treatment is shown for convenience in Fig. 5.1 below.

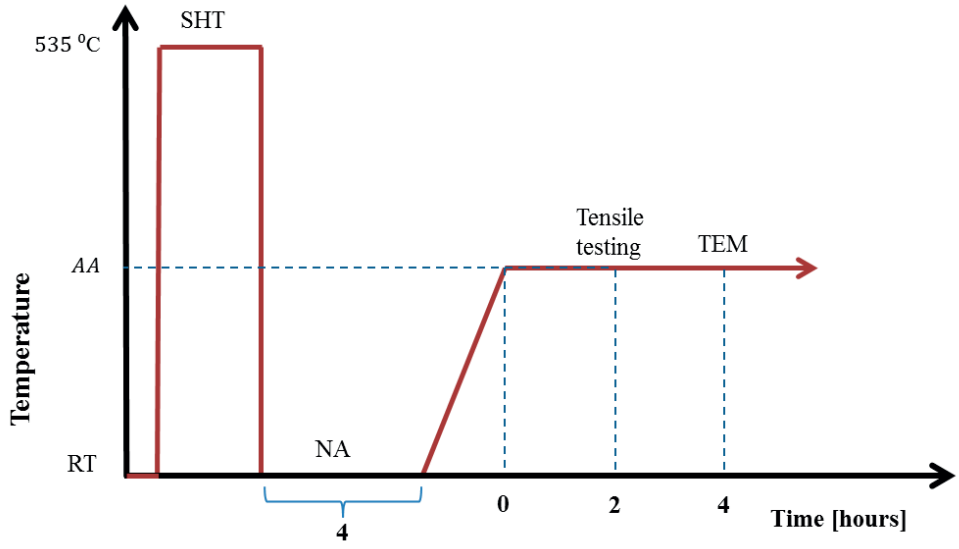

Figure 5.1 Heat treatment of the material used for tensile testing. The heat treatment was done for AA temperatures of 195 °C, 220 °C or 240 °C.

A selection of the most important quantitative results from the tensile tests is given in Table 5.2 at the end of this section. Results corresponding to 0 hours AA are also given in Table 5.2 for comparison.

A.1 Tensile Tests for AA at 195 °C

Full tensile curves after AA of the four alloys at 195 °C for 2 hours are given in Fig. 5.2. Two parallel tensile tests have been done for each alloy. The yield strength region is shown in Fig. 5.3. RXG2, RXGC1 and RXGC2 had relatively high peak hardness even though the solute additions were reduced in at % as compared to the dense reference RX0.

The most interesting values from Figs. 5.2 and 5.3 are highlighted in Table 5.1. Interestingly, the yield strength and UTS does not follow the same behaviour as the HV curves. Even though RXG2 has the peak hardness closest to RX0, it is clear that it does not have the same strain hardening potential at lower strain values. The reference alloy has the highest yield strength of the four. However, RX0 is surpassed by the other alloys at UTS. The reference RX0 does indeed seem to be the least ductile out of the four alloys presented here. The lower ductility is not surprising; given it is the alloy with the highest solute content. As RXG2 and RXGC2 have the same total at % of solute, more Ge gives higher yield strength but lower ductility. There is a higher number density of precipitate needles present in RXG2, impeding dislocation movement, which is probably on of the major reasons why this alloys is less ductile.

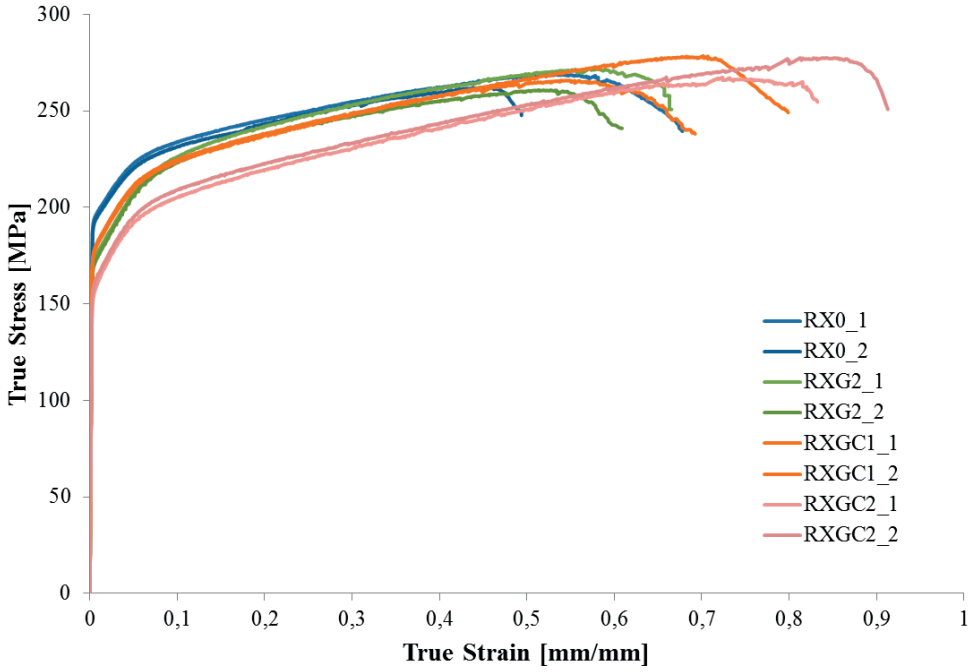

Figure 5.2 Stress-strain curves for the four alloys RX0, RXG2, RXGC1 and RXGC2. Two parallels have been measured for each condition, indicated by the numbers 1 and 2 in the curve-labels. The tensile tests were performed after 2 hours AA at 195 °C.

Table 5.1 The four alloys subjected to tensile testing with their corresponding yield strength, ultimate tensile strength (UTS) and hardness values. Tensile testing was performed after AA at 195 °C for 2 hours. See Table 5.2 for more details.

Alloy	Yield Strength [Mpa]	UTS [MPa]	HV
RX0	192,0	265,5	76,4
RXG2	170,5	266,5	76,7
RXGC1	176,5	272,5	71,9
RXGC2	156,5	272,0	65,5

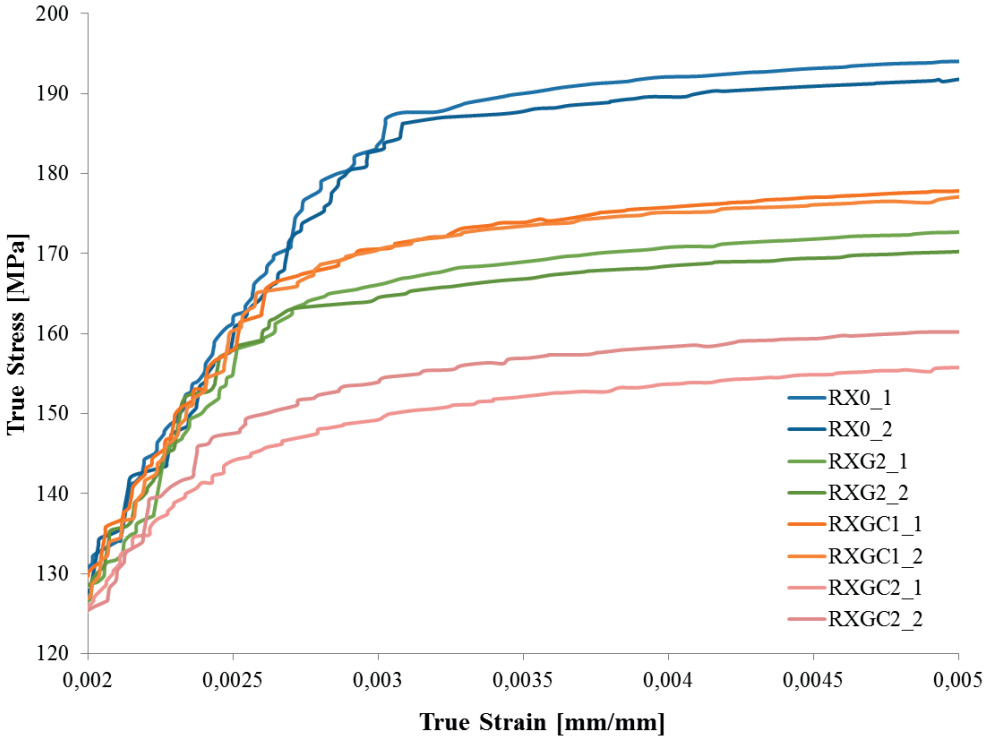

Figure 5.3 Enlarged overview of the yield strength region of the tensile tests in Fig. 5.2. Two parallel tests have been performed for each condition.

A.2 Tensile Tests for AA at 220 °C

Full tensile curves were acquired for the four alloys after AA at 220 °C for 2 hours, the results are shown in Fig. 5.4. Also in this case, it is the reference alloy RX0 which has the highest yield strength, see enlarged view in Fig. 5.5. RXGC1 has the second highest yield strength, but the highest UTS. RXG2 has lower yield strength and UTS and is also less ductile than the other alloys in this case. See Table 5.2 for more details about the tensile test results.

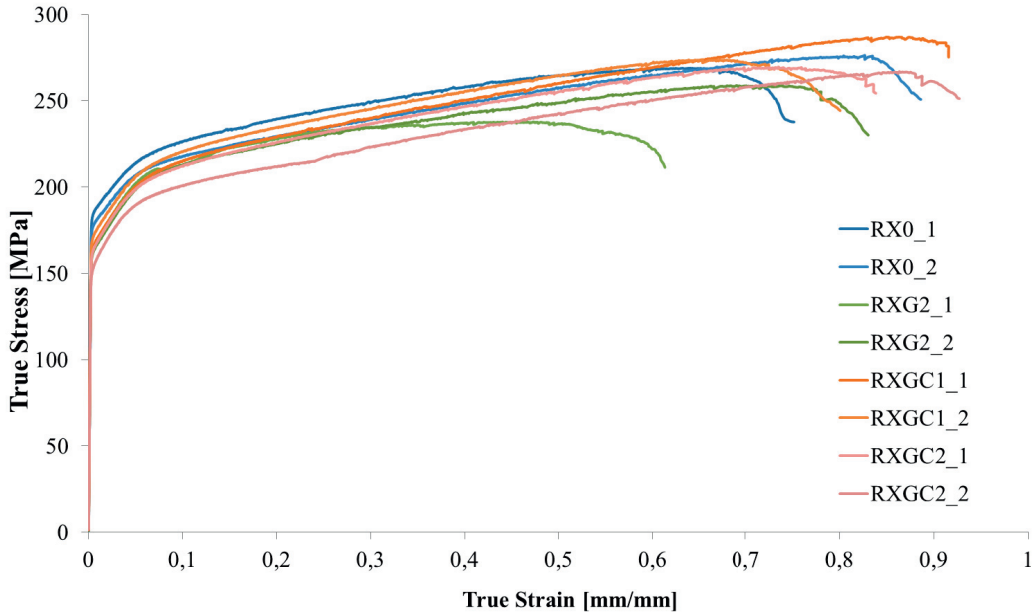

Figure 5.4 Stress-strain curves for the four alloys RX0, RXG2, RXGC1 and RXGC2. Two parallels have been measured for each condition. The tensile tests were performed after 2 hours AA at 220 °C.

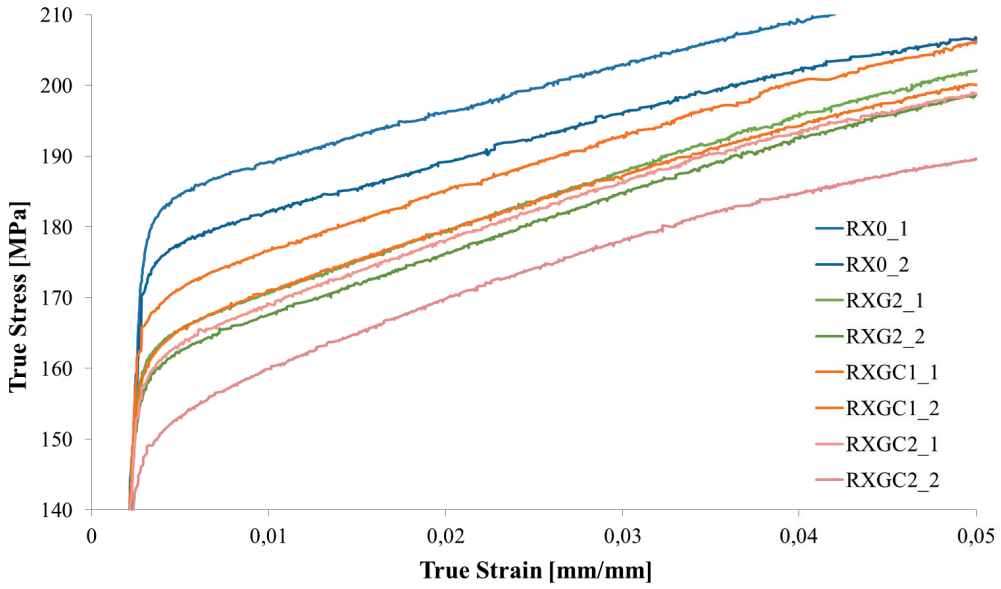

Figure 5.5 Enlarged view of the tensile curves from Fig. 5.4. Two parallel tests have been performed for each condition.

A.3 Tensile Tests for AA at 240 °C

Full tensile curves for the four alloys after AA at 240 °C for 2 hours are given in Fig. 5.6. Here, RXG2 has the lowest yield strength of the four alloys, while the reference RX0 has the highest. See Fig. 7 for an enlarged view of the yield strength region. RXGC1 is again the most promising alloy with regard to UTS and potential elongation. More details about the tensile tests are given in Table 5.2.

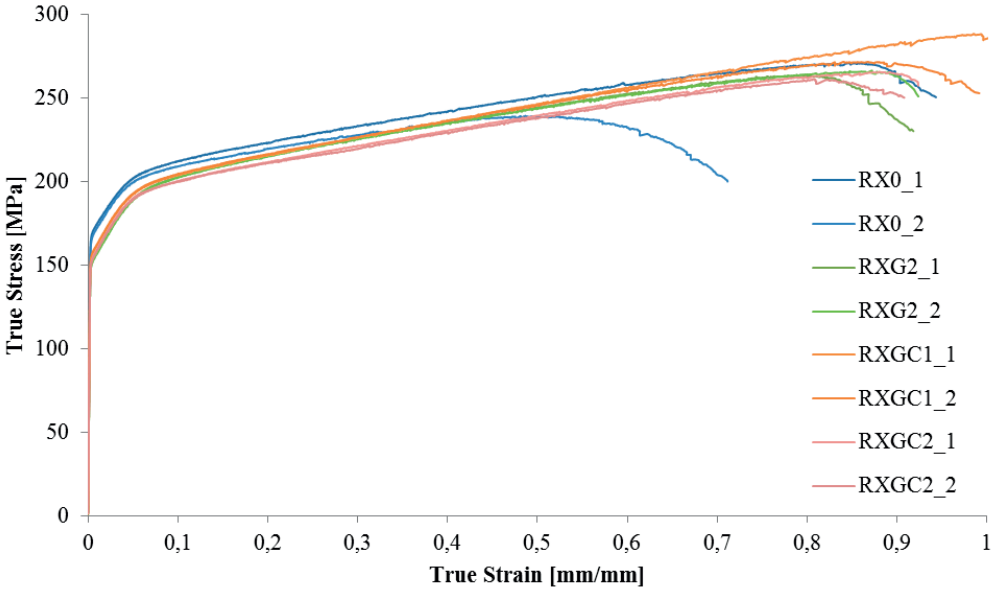

Figure 5.6 Stress-strain curves for the four alloys RX0, RXG2, RXGC1 and RXGC2. Two parallels have been measured for each condition. The tensile tests were performed after 2 hours AA at 240 °C.

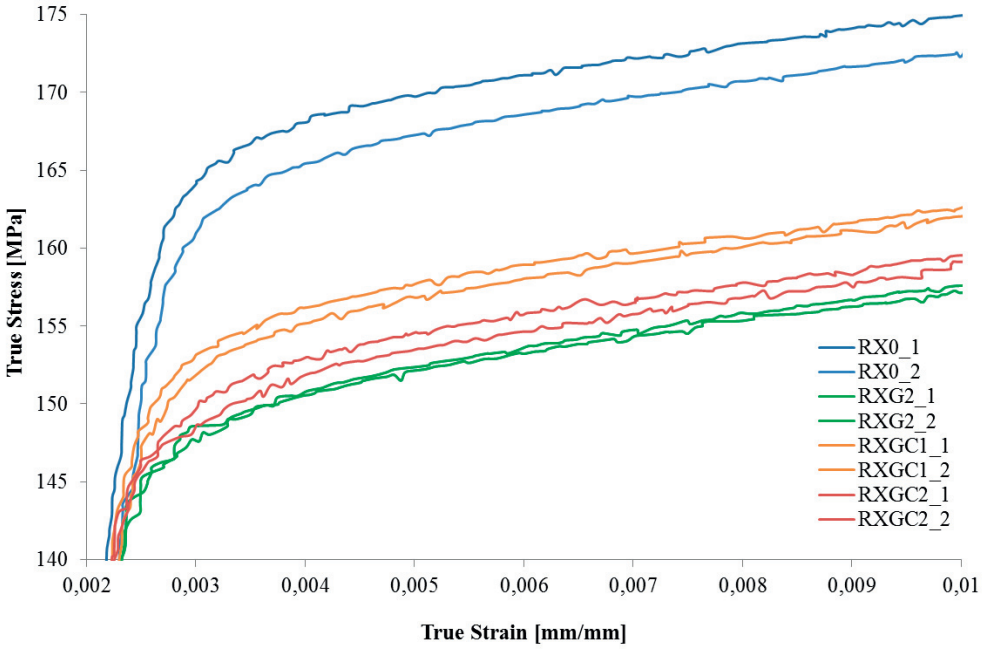

Figure 5.7 Enlarged view of the tensile curves from Fig. 5.6. Two parallels have been performed for each condition.

Table 5.2 Important results from the tensile tests of RX0, RXG2, RXGC1 and RXGC2.

Test specimen id.	Ageing Temperature Time	Yield strength RP0.2 [MPa]	Tensile strength Rm [MPa]	Strain at max. load Agt [mm/mm]	Uniaxial peak true stress [MPa]	Bridgeman peak true stress [MPa]	True strain at fracture [mm/mm]
Rx0_1	195°C/2h	193	213	0,071	269	219	0,67
Rx0_2	195°C/2h	191	211	0,072	262	210	0,49
RxG2_1	195°C/2h	172	205	0,106	272	221	0,66
RxG2_2	195°C/2h	169	202	0,099	261	211	0,61
RxGC1_1	195°C/2h	177	204	0,085	266	216	0,69
RxGC1_2	195°C/2h	176	203	0,085	279	229	0,80
RxGC2_1	195°C/2h	154	186	0,090	267	220	0,83
RxGC2_2	195°C/2h	159	190	0,091	277	230	0,91
Rx0_1	220°C/0h	184	206	0,080	269	220	0,75
Rx0_2	220°C/0h	177	198	0,074	276	228	0,88
RxG2_1	220°C/0h	164	196	0,073	238	192	0,61
RxG2_2	220°C/0h	161	193	0,087	259	213	0,83
RxGC1_1	220°C/0h	164	195	0,094	287	238	0,91
RxGC1_2	220°C/0h	170	200	0,091	274	225	0,80
RxGC2_1	220°C/0h	162	193	0,088	270	222	0,83
RxGC2_2	220°C/0h	151	183	0,080	267	221	0,92
Rx0_1	240°C/0h	169	194	0,069	271	225	0,94
Rx0_2	240°C/0h	166	191	0,068	239	195	0,71
RxG2_1	240°C/0h	151	184	0,086	264	219	0,91
RxG2_2	240°C/0h	151	184	0,088	267	221	0,92
RxGC1_1	240°C/0h	155	186	0,078	289	242	1,06
RxGC1_2	240°C/0h	156	186	0,079	272	227	0,99
RxGC2_1	240°C/0h	153	182	0,070	266	220	0,92
RxGC2_2	240°C/0h	152	182	0,077	261	217	0,90

Bibliography

[1] H. Aluminium, “hydro.com,” Hydro aluminium, [Online]. Available: http://www.hydro.com/en/About-aluminium/Why-aluminium/Physical-properties/. [Accessed 18 July 2016].

[2] I. Polmear, Light Alloys, From Traditional Alloys to Nanocrystals, Oxford UK1: Elsevier, 2006.

[3] G. E. Totten and D. S. MacKenzie, Handbook of Aluminum, Marcel Dekker Inc., 2003.

[4] J. R. Davis, Aluminum and Aluminum Alloys, ASM International, 1993.

[5] M. J. Buehler, A. Hartmaier, M. A. Duchaineau, F. R. Abraham and H. J. Gao, *Acta Mechanica Sinica,* vol. 21, p. 103, 2005.

[6] J. D. Verhoeven, Fundamentals of Physical Metallurgy, London: John Wiley & Sons, 1975.

[7] O. R. Myhr, Ø. Grong and S. J. Andersen, “Modeling of the age hardening behaviour of Al-Mg-Si alloys,” *Acta Mater.,* vol. 49, pp. 65 - 75, 2001.

[8] S. Wenner, Transmission Electron Microscopy and Muon Spin Relaxation Studies of Precipiation in Al-Mg-Si Alloys, Trondheim: Norwegian University of Science and Technology, 2014.

[9] L. Jones, H. Yang, T. J. Pennycook, M. S. J. Marshall, S. V. Aert, N. D. Browning, M. R. Castell and P. D. Nellist, “Smart Align - a new tool for robust non-rigid registration of scanning microscope data,” *Advanced Structural and Chemical Imaging,* vol. 1, 2015.

[10] T. Saito, S. Muraishi, C. D. Marioara, S. J. Andersen, J. Røyset and R. Holmestad, *Met. Mater. Trans. A,* vol. 44, pp. 4124 - 4135, 2013.

[11] K. Teichmann, C. D. Marioara, S. J. Andersen and K. Marthinsen, *Met. Mater. Trans. A,* vol. 43, pp. 4006 - 4014, 2012.

[12] C. D. Marioara, H. Nordmark, S. J. Andersen and R. Holmestad, *J. Mater. Sci.,* vol. 41, pp. 471 - 478, 2006.

[13] G. A. Edwards, K. Stiller, G. L. Dunlop and M. J. Couper, *Acta Mater.,* vol. 46, pp. 3893 - 3904, 1998.

[14] C. D. Marioara, S. J. Andersen, J. Jansen and H. W. Zandbergen, *Acta Mater.,* vol. 49, pp. 321 - 328, 2001.

[15] J. H. Chen, E. Costan, M. A. v. Huis, Q. Xu and H. W. Zandbergen, "Atomic Pillar-Based Nanoprecipitates Strengthen AlMgSi Alloys," *Science,* vol. 312, p. 416, 2006.

[16] S. J. Andersen, H. W. Zandbergen, J. Jansen, C. Træholt, U. Tundal and O. Reiso, *Acta Mater.,* vol. 46, pp. 3283 - 3298, 1998.

[17] H. S. Hasting, A. G. Frøseth, S. J. Andersen, R. Vissers, J. C. Walmsley, C. D. Marioara, F. Danoix, W. Lefebvre and R. Holmestad, *J. Appl. Phys.,* vol. 106, 2009.

[18] R. Vissers, M. A. v. Huis, J. Jansen, H. W. Zandbergen, C. D. Marioara and S. J. Andersen, *Acta Mater.,* vol. 55, pp. 3815 - 3823, 2007.

[19] S. J. Andersen, C. D. Marioara, R. Vissers, A. Frøseth and H. W. Zandbergen, *Mater. Sci. Eng. A,* vol. 444, pp. 157 - 169, 2007.

[20] S. J. Andersen, C. D. Marioara, A. Frøseth, R. Vissers and H. W. Zandbergen, *Mater. Sci. Eng. A,* vol. 390, pp. 127 - 138, 2005.

[21] R. Vissers, C. D. Marioara, S. J. Andersen and R. Holmestad, *Aluminium Alloys,* vol. 2, pp. 1263 - 1269, 2008.

[22] D. A. Porter and K. E. Easterling, Phase Transformations in Metals and Alloys, 2nd ed., Chapman & Hall, 1992.

[23] C. Wolverton, *Acta Mater. ,* vol. 55, pp. 5867 - 5872, 2007.

[24] E. A. Mørtsell, S. J. Andersen, J. Friis, C. D. Marioara and R. Holmestad, "Atomistic details of precipitates in lean Al-Mg-Si alloys with trace additions of Ag and Ge studied by HAADF-STEM and DFT," *In progress,* 2016.

[25] P. B. Hirsch, J. Silcox, R. E. Smallman and K. H. Westmacott, *Phil. Mag. ,* vol. 3, pp. 897 - 908, 1958.

[26] S. Yoshida, Y. Shimomura and M. Kiritani, *Journal of the Physical Society of Japan,* vol. 17, p. 1196, 1962.

[27] V. Gavini, K. Bhattacharya and M. Ortiz, "Vacancy clustering and prismatic dislocation loop formation in aluminium," *Phys. Rev. B,* vol. 76, p. 180101, 2007.

[28] L. A. Westfall, “An investigation of nano-voids in quenched aluminium by small-angle x-ray scattering,” Queen's University, Kingston, Ontario, Canada, 2008.

[29] M. Kubota, J. F. Nie and B. C. Muddle, “Characterization of Precipitation hardening responce and as-Quenched Microstructures in Al-Mg(-Ag) alloys,” *Mater. Trans.,* vol. 45, pp. 3256 - 3263, 2012.

[30] C. D. Marioara, S. J. Andersen, H. W. Zandbergen and R. Holmestad, *Metall. Mat. Trans. A,* vol. 36, pp. 691 - 702, 2005.

[31] M. Torsæter, H. S. Hasting, W. Lefebvre, C. D. Marioara, J. C. Walmsley, S. J. Andersen and R. Holmestad, “the influence of composition and natural ageing on clustering during preaging in Al-Mg-Si alloys,” *J. Appl. Phys.,* vol. 108, p. 073527, 2010.

[32] S. J. Andersen, C. D. Marioara, R. Vissers, A. L. Frøseth and P. Derlet, in *Proc. 13th Eur. Mocr. Congress (EMC) 2*, 2004.

[33] F. J. H. Ehlers, S. Wenner, S. J. Andersen, C. D. Marioara, W. Lefebvre, C. B. Boothroyd and R. Holmestad, “Phase stabilization principle and precipitate-host lattice influences for Al-Mg-Si-Cu alloy precipitates,” *J Mater Sci,* vol. 49, pp. 6413 - 6426, 2014.

[34] C. Wolverton, “Solute vacancy binding in aluminium,” *Acta Mater.,* vol. 55, pp. 5867 - 5872, 2007.

[35] H. L. Jr and P. Coleman, “Vacancy clustering in quenched Al-Li solid solution alloys studied by Doppler broadening spectroscopy,” *J. Phys.: Condensed Matter,* vol. 10, pp. 10423 - 10428, 1998.

[36] Y. Koshino, M. Kozuka, S. Hirosawa and Y. Aruga, “Comparative and complementary characterization of precipitate microstructures in Al-Mg-Si(-Li) alloys by transmission electron microscopy, energy dispersive X-ray spectroscopy and atom probe tomography,” *Journal of Alloys and Compounds,* vol. 622, pp. 765 - 770, 2015.

[37] G. Svenningsen, M. H. Larsen, J. C. Walmsley, J. H. Nordlien and K. Nisancioglu, *Corros. Sci. ,* pp. 1528 - 1543, 2006.

[38] G. Svenningsen, J. Lein, A. Bjørgum, J. H. Nordlien, Y. Yu and K. Nisancioglu, *Corros. Sci.,* vol. 48, pp. 226 - 242, 2006.

[39] H. Zahn, J. M. C. Mol, F. Hannour, L. Zhuang, H. Terryn and J. H. W. d. Wit, *Materials and Corrosion,* vol. 59, pp. 670 - 675, 2008.

[40] C. D. Marioara, S. J. Andersen, T. N. Stene, H. Hasting, J. Walmsley, A. T. J. V.

Helvoort and R. Holmestad, *Philosophical Magazine,* vol. 87, p. 3385, 2007.

[41] D. J. Chakrabarti and D. E. Laughlin, *Prog. Mater. Sci.,* vol. 49, p. 389, 2004.

[42] C. Cayron, L. Sagalowicz, O. Beffort and P. A. Buffat, *Philos. Mag. A,* vol. 79, p. 2833, 1999.

[43] K. Matsuda, Y. Uetani, T. Sato and S. Ikeno, *Metall. Mater. Trans. A,* vol. 32, p. 1293, 2001.

[44] L. Arnberg and B. Aurivillius, *Acta Chem Scand A,* vol. 34, p. 1, 1980.

[45] T. Saito, C. D. Marioara, S. J. Andersen, W. Lefebvre and R. Holmestad, *J. Phys. Conf. Ser. 522,* p. 012030, 2104.

[46] J. M. Silcock and T. J. Heal, *Acta Cryst.,* vol. 9, p. 680, 1956.

[47] C. D. Marioara, S. J. Andersen, J. Røyset, O. Reiso, S. Gulbrandsen-Dahl, T. E. Nicolaisen, I. E. Opheim, J. F. Helgaker and R. Holmestad, *Metall. Mater. Trans. A,* vol. 45, pp. 2938 - 2949, 2014.

[48] J. M. Rosalie, D. Dwyer and L. Bourgeois, *Acta. Mater.,* vol. 69, pp. 224 - 235, 2014.

[49] C. D. Marioara, J. Nakamura, K. Matsuda, S. J. Andersen, R. Holmestad, T. Sato, T. Kawabata and S. Ikeno, *Phil. Mag.,* vol. 92, pp. 1149 - 1158, 2012.

[50] J. Rosalie, L. Bourgeois and B. C. Muddle, *Phil. Mag. ,* vol. 89, pp. 2195 - 2211, 2009.

[51] J. Kim, C. D. Marioara, R. Holmestad, E. Kobayashi and T. Sato, *Mater. Sci. Eng. A,* vol. 560, pp. 154 - 162, 2013.

[52] K. Matsuda, J. Nakamura, T. Kawabata, S. Ikeno, T. Sato, C. D. Marioara, S. J. Andersen and R. Holmestad, *Mater. Sci. Forum,* Vols. 706 - 709, pp. 357 - 360, 2012.

[53] K. Matsuda, S. Ikeno and T. Munekata, "HRTEM Study of Precipitates in Al-Mg-Si and Al-Mg-Ge Alloys," *Mater. Sci. Forum,* Vols. 519 - 521, p. 221, 2006.

[54] R. Bjørge, C. D. Marioara, S. J. Andersen and R. Holmestad, *Metal. Mater. Trans. A,* vol. 41, p. 1907, 2010.

[55] R. Bjørge, S. J. Andersen, C. D. Marioara, J. Etheridge and R. Holmestad, *Phil. Mag. ,* vol. 92, pp. 3983 - 3993, 2012.

[56] D. B. Williams and C. B. Carter, Transmission Electron Microscopy, Part 1: Basics, New York: Springer, 2009.

[57] S. Pennycook and D. Jesson, “High-resolution Z-contrast imaging of crystals,” *Ultramicroscopy,* vol. 37, pp. 14-38, 1991.

[58] P. D. Nellist and S. J. Pennycook, “Accurate structure determination from image reconstruction in ADF STEM,” *Journal of Microscopy,* vol. 190, pp. 159-170, 1998.

[59] V. T. Fauske, Electron Microscopy Based Characterization of Semiconductor Nanowires, Trondheim: NTNU, 2016.

[60] R. F. Egerton, P. Li and M. Malac, “Radiation damage in the TEM and SEM,” *Micron,* vol. 35, pp. 399 - 409, 2004.

[61] E. A. Mørtsell, S. Wenner, P. Longo, S. J. Andersen, C. D. Marioara and R. Holmestad, “Elemental electron energy loss mapping of a precipitate in a multi-component aluminium alloy,” *Micron,* April 2016.

[62] I. Gatan, “Gatan, Inc.,” Gatan, [Online]. Available: http://www.gatan.com/products/tem-imaging-spectroscopy/stempack-spectrum-imaging . [Accessed 05 June 2016].

[63] D. B. Williams and C. B. Carter, Transmission Electron Microscopy, Part 4: Spectroscopy, New York: Springer, 2009.

[64] T. Malis, S. C. Cheng and R. F. Egerton, “EELS log-ratio technique for specimen-thickness measurement in TEM,” *Journal of Electron Microscopy Techniques,* vol. 8, pp. 193-200, 1988.

[65] C. C. Ahn, O. L. Krivanek, R. P. Burgner, M. M. Disko and P. R. Swann, EELS Atlas - A reference guide of electron energy loss spectra covering all stable elements, Arizona: ASU HREM facility and GATAN, 1983.

[66] S. P. Cooil, Controlling the Epitaxial Growth of Graphene On Diamond Surfaces, Aberystwyth, 2014.

[67] T. Schmidt, S. Heun, J. Slezak, J. Diaz and K. C. Prince, “SPELEEM: Combining LEEM and Spectroscopic Imaging,” *Surface Review and Letters,* vol. 5, no. 6, pp. 1287 - 1296, 1998.

[68] H. Chandler, Hardness Testing 2nd Edition, ASM International, 1999.

[69] U. Tundal, O.Reiso, E. Hoff, R. Dickson and C. Devadas, in *Proc. 10th International Aluminum Extrusion Technology Seminar*, Miami, 2012.

[70] P. Hohenberg and W. Kohn, “Inhomogeneous Electron Gas,” *Phys. Rev.,* vol. 136, pp. B864 - B871, 1964.

[71] W. Kohn and L. J. Sham, “Self-consistent equations including exchange and correlation effects,” *Phys. Rev. B,* vol. 140, pp. 1133 - 1138, 1965.

[72] G. Kresse and J. Hafner, “Ab initio molecular dynamics for liquid metals,” *Phys. Rev. B,* vol. 32, pp. R558 - R561, 1993.

[73] G. Kresse and J. Furthmüller, “Efficiency of ab initio total energy calculations for metals and semiconductors using a plane wave basis set.,” *Comput. Mater. Sci.,* vol. 6, pp. 15 - 50, 1996.

[74] P. H. Ninive, A. Strandlie, S. Gulbrandsen-Dahl, W. Lefebvre, C. D. Marioara, S. J. Andersen, J. Friis, R. Holmestad and O. M. Løvvik, “Detailed atomistic insight itno the beta" phase in Al-Mg-Si alloys,” *Acta Materialia,* vol. 69, pp. 126 - 134, 2014.

[75] S. Vannarat, M. H. F. Sluiter and Y. Kawazoe, *Phys. Rev. B,* vol. 64, pp. 1 - 8, 2001.

[76] G. P. M. Leyson, L. G. Hector and W. A. Curtin, “Solute strengthening from first principles and application to aluminum alloys,” *Acta Mat.,* vol. 60, pp. 3873 - 3884, 2012.

[77] E. A. Mørtsell, C. D. Marioara, S. J. Andersen, I. G. Ringdalen, J. Friis, S. Wenner, J. Røyset, O. Reiso and R. Holmestad, “The effect of Li-additions in lean Al-Mg-Si alloys,” *Work in progress,* 2016.

[78] T. Saito, C. D. Marioara, S. J. Andersen, W. Lefebvre and R. Holmestad, “Aberration-corrected HAADF-STEM investigations of precipitate structures in Al-Mg-Si alloys with low Cu additions,” *Philosophical Magazine,* vol. 94, no. 5, pp. 520 - 531, 2015.

[79] E. A. Mørtsell, I. Westermann, C. D. Marioara, K. O. Pedersen, S. J. Andersen, J. Røyset and R. Holmestad, “The Effect of 1 % Plastic Deformation and Elastic Strain on a 6060 Aluminium Alloy during Natural and Artificial Ageing,” *Work in progress,* 2016.

[80] J. Holmestad, (Scanning) Transmission Electron Microscopy Studies of Grain Boundary Segregation relevant to Intergranular Corrosion in Al-Mg-Si-Cu Alloys, Trondheim: NTNU, 2015.

[81] A. Sagara and K. Kamada, “Measurements of evaporation rate of Lithium from Al-Li alloy by depth profiling with an ion beam,” *Nuclear Instruments and Methods in Physics Research B,* vol. 44, pp. 373 - 376, 1990.

[82] S. P. Cooil, E. A. Mørtsell, F. Mazzola, M. Jorge, S. Wenner, M. Edmonds, L. Thomsen, H. G. Klemm, G. Peschel, J. A. Miwa, R. Holmestad and J. W. Wells, “Thermal preicpitation of alloying agents in aluminium,” *Work in progress,* 2016.

[83] V. T. Fauske, J. Huh, G. Divitini, D. L. Dheeraj, A. M. Munshi, C. Ducati, H. Weman,

B. O. Fimland and A. T. J. v. Helvoort, “In Situ Heat-Induced Replacement of GaAs Nanowires by Au,” *Nano Letters,* vol. 16, no. 5, pp. 3051 - 3057, 2016.

[84] E. A. Mørtsell, C. D. Marioara, S. J. Andersen, J. Røyset, O. Reiso and R. Holmestad, *Metallurgical and Materials Transactions A,* vol. 46, no. 9, pp. 4369 - 4379, 2015.

[85] E. I. 6892, *Metallic Materials - Tensile testing - Part 1: Method of test at room temperature,* 2009.

[86] E. A. Mørtsell, C. D. Marioara, S. J. Andersen, J. Røyset, O. Reiso and R. Holmestad, “Effects of Germanium, Copper, and Silver Substitutions on Hardness and Microstructure in Lean Al-Mg-Si Alloys,” *Metallurgical and Materials Transactions A,* vol. 46, no. 9, pp. 4369 - 4379, 2015.